Alma Mater Studiorum · Università di Bologna

SCUOLA DI SCIENZE
Dipartimento di Fisica e Astronomia
Corso di Laurea Magistrale in Astrofisica e Cosmologia

Upper limits on the 21 cm power spectrum from the Epoch of Reionization

Tesi di Laurea Magistrale

Candidato:
Emilio Ceccotti

Relatore:
Chiar.mo
Prof. Lauro Moscardini

Correlatore:
Dott. Gianni Bernardi

Sessione IV
Anno Accademico 2018-2019

This Thesis work was done as part of the research activity of the

Istituto di Radioastronomia - Istituto Nazionale di Astrofisica
(Bologna)

Contents

Abstract

The 21 cm line is one of the most promising probes of the intergalactic medium (IGM), especially of its thermal and ionization history, from the Cosmic Dawn ($z \approx 30$) until the end of the Epoch of Reionization (EoR, $z \approx 6$). The biggest challenge to 21 cm observations is the presence of Galactic and extragalactic foreground emission that is a few orders of magnitude brighter than the cosmological signal everywhere in the sky. Foreground and 21 cm emission can, however, be separated spectrally, as foreground emission is spectrally smooth on scales of tens of MHz, whereas the 21 cm emission significantly evolves on MHz scales.

In this Thesis work, we analyse observations taken with the Precision Array to Probe the Epoch of Reionization (PAPER; Parsons et al. 2010) in the 120−180 MHz range (i.e., $6 < z < 10$). In particular, we focus on the power spectrum estimate of the EoR signal at four different redshift intervals ($z = 7.48$, 8.13, 8.85, 9.93) from a subset of ~ 8 hours of data. The analysis of PAPER data is rather unconventional: the array is constituted by 128 dipoles arranged in a highly redundant configuration in order to maximize the power spectrum sensitivity on a limited number of k-modes. For this very reason, PAPER observations are not ideal to image and model foreground emission: we instead adopted a strategy that relies on avoidance, i.e. isolating the power spectrum region where the foreground emission is expected to be fainter than the cosmological signal. Given the high redundancy, we estimated the power spectrum from PAPER observations using only 30 m baselines, the most numerous one, that also enable comparison with previous works (e.g., Kolopanis et al. 2019).

After an initial data selection, we developed a pipeline to estimate the power spectrum of the 21 cm signal. The pipeline averages calibrated data over the duration of the observation, Fourier (“delay”) transforms them along the frequency axis and then calculate cross-products between different baselines of the same length. The resulting cross-spectra are averaged to obtain a final estimate for each redshift interval. The delay transform separates the foregrounds, that are confined to the $k < 0.2\,h\,\mathrm{Mpc}^{-1}$ region. Higher k-modes are consistent with the noise power spectrum that we derived from the data themselves. We therefore estimated upper limits on the 21 cm power spectrum at $0.2 < k < 0.5\,h\,\mathrm{Mpc}^{-1}$ to be $(35\,000\,\mathrm{mK})^2$, $(11\,000\,\mathrm{mK})^2$, $(51\,000\,\mathrm{mK})^2$ and $(3200\,\mathrm{mK})^2$ at $z = 9.93$, 8.84, 8.13 and 7.48, respectively. Using a simple, analytic model of the 21 cm signal (Parsons et al. 2014) and assuming an average neutral fraction $\overline{x}_{\mathrm{HI}} = 0.3$ (Greig and Mesinger 2017), we calculated a 70 mK lower limit on the IGM temperature at $z = 7.48$, in agreement with existing models.

Sommario

La riga a 21 cm è una delle più promettenti sonde del mezzo intergalattico (IGM), specialmente per quanto riguarda la sua storia termica e di ionizzazione, dalla Cosmic Dawn ($z \approx 30$) fino alla fine dell'Epoca della Reionizzazione (EoR, $z \approx 6$). La più grande sfida per le osservazioni della 21 cm è la presenza dell'emissione Galattica ed extragalattica di foreground, la quale è qualche ordine di grandezza più brillante del segnale cosmologico ovunque nel cielo. Il foreground e l'emissione della 21 cm possono comunque essere separati spettralmente, dato che l'emissione di foreground è spettralmente piatta su scale di decine di MHz, mentre l'emissione della 21 cm evolve significativamente su scale dell'ordine del MHz.

In questo lavoro di Tesi, abbiamo analizzato osservazioni prese con il Precision Array to Probe the Epoch of Reionization (PAPER; Parsons et al. 2010) nel range $120 - 180\,\mathrm{MHz}$ (cioè $6 < z < 10$). In particolare, ci concentriamo sulla stima dello spettro di potenza del segnale dalla EoR in quattro diversi intervalli di redshift ($z = 7.48$, 8.13, 8.85, 9.93) da un sottoinsieme di ~ 8 ore di dati. L'analisi dei dati di PAPER è piuttosto non convenzionale: l'array è costituito da 128 dipoli disposti in una configurazione altamente ridondante, in modo da massimizzare la sensibilità dello spettro di potenza su un numero limitato di modi k. Per questo motivo, le osservazioni di PAPER non sono ideali per fare immagini e modelli dell'emissione di foregroud: adottiamo invece una strategia basata sull'avoidance, cioè l'isolare la regione dello spettro di potenza in cui l'emissione di foreground dovrebbe essere più debole del segnale cosmologico. Data l'elevata ridondanza, stimiamo lo spettro di potenza dalle osservazioni di PAPER usando solo le baseline di 30 m, le più numerose, che ci permettono anche di fare un confronto con i precedenti lavori (e.g., Kolopanis et al. 2019).

Dopo un'iniziale selezione dei dati, abbiamo sviluppato una pipeline per stimare lo spettro di potenza del segnale della 21 cm. La pipeline media i dati calibrati sulla durata dell'osservazione, ne fa la trasformata di Fourier ("delay" transform) lungo le frequenze e poi calcola il cross-prodotto tra le diverse baseline della stessa lunghezza. I risultanti cross-spettri vengono mediati in modo da ottenere una stima finale per ogni intervallo di redshift. La delay transform separa i foreground, i quali sono confinati nella regione con $k < 0.2\,h\,\mathrm{Mpc}^{-1}$. I modi k più alti sono consistenti con lo spettro di potenza del rumore che abbiamo derivato dai dati stessi. Abbiamo inoltre stimato che i limiti superiori dello spettro di potenza della 21 cm per $0.2 < k < 0.5\,h\,\mathrm{Mpc}^{-1}$ sono $(35\,000\,\mathrm{mK})^2$, $(11\,000\,\mathrm{mK})^2$, $(51\,000\,\mathrm{mK})^2$ e $(3200\,\mathrm{mK})^2$, rispettivamente a $z = 9.93$, 8.84, 8.13 e 7.48. Usando un semplice modello analitico del segnale della 21 cm (Parsons et al. 2014) e assumendo una frazione neutra media $\overline{x}_{\mathrm{HI}} = 0.3$ (Greig e Mesinger 2017), abbiamo calcolato un limite inferiore di $70\,\mathrm{mK}$ per la temperature dell'IGM a $z = 7.48$, in accordo con gli attuali modelli.

Introduction

Our understanding of cosmology has had a remarkable development in the last few decades, in which a concordance model has been reached, i.e., the ΛCDM model. According to this, our Universe is made up of cold dark matter (CDM), baryonic matter, radiation, and dark energy (well represented by the cosmological constant Λ). The model is supported by many independent observational probes, such as the primordial nucleosynthesis (Beringer et al. 2012), the cosmic microwave background (CMB; Planck Collaboration et al. 2018a) and the power spectrum of large scale structure (Tegmark et al. 2006). Despite this progress, we know very little, observationally speaking, about the first billion years of the Universe, a fundamental period for the formation of first stars and galaxies.

After the cosmological recombination, all the gas in the Universe is in a neutral state. First luminous sources begin to form within dense clouds and start heating and ionizing the surrounding intergalactic medium (IGM) (e.g., Barkana and Loeb 2001). This is the beginning of the Epoch of Reionization (EoR) which is observationally constrained in the redshift range $12 < z < 6$. Thanks to the presence of neutral hydrogen, the 21 cm line emitted from hydrogen hyperfine transition is a powerful probe of the cosmic evolution during this epoch (Furlanetto et al. 2006). That line is emitted at 1420 MHz, but it is observed from Earth redshifted into the ~ 100 MHz radio band. Each frequency maps a certain redshift, so that is possible to reconstruct 3D pictures of the evolution of IGM and, hence, of cosmic structures. Such maps require high angular resolutions and sensitivities to be achieved, thus current experiments are focusing on statistical measurements of the cosmological signal, through the power spectrum estimator.

There are two complementary approaches to measure the 21 cm signal: global experiments measuring the sky-averaged brightness temperature of the line relative to the CMB background (e.g., EDGES; Bowman et al. 2008; Bowman et al. 2018, SARAS; Patra et al. 2013, LEDA; Bernardi et al. 2015), and interferometers targeting spatial fluctuations caused by heating, collapse and ionization (e.g., LOFAR; van Haarlem et al. 2013, MWA; Tingay et al. 2013, PAPER; (Parsons et al. 2010)).

The biggest challenge to all 21 cm observations is the contamination from Galactic and extragalactic foregrounds, whose emission is few orders of magnitudes brighter than the cosmological signal everywhere in the sky. However, foregrounds and 21 cm emissions can be separated because of the different spectral behaviours: the former are generally spectrally smooth, whereas the latter fluctuate significantly with frequencies. We can mitigate foreground contamination by subtracting the emission with some form of fitting or avoiding it with a delay transform of visibilities, i.e., a Fourier transform along the frequency axis (Parsons et al. 2012a). PAPER was the first instrument to apply the avoidance method in order to estimate the power spectrum. With the delay transform approach, data from each interferometric baseline can be analysed separately, without requiring foreground imaging and modelling. Thus, PAPER baselines were deployed in a highly redundant configuration, i.e., on a regular grid where same baseline length and orientation are repeated several times. This boosts the power spectrum sensitivity on a given k-mode corresponding to the baseline length (Parsons et al. 2012b).

In view of the ongoing and next-generation large interferometric arrays, such as HERA (DeBoer et al. 2017) and SKA (Mellema et al. 2013), that will explore the Epoch of Reionization in great details, it is crucial to accurately define a strong analysis method to obtain a power spectrum estimator foreground free.

This Thesis work is organized as follows.

- In Chapter 1 we introduce the current cosmological scenario, focusing on the ΛCDM model, the cosmic microwave background and the structure formation theory.
- In Chapter 2 we briefly review the theory of the 21 cm line and its cosmological applications, discussing both the global signal and the spatially fluctuating one.
- In Chapter 3 we describe the fundamentals of interferometry, in order to define the delay transform. We then provide information about main Galactic and extragalactic foregrounds, and current methods to mitigate their contamination. We place great emphasis on the avoidance technique.
- In Chapter 4 we present PAPER and the data set used in our analysis, evaluating their noise level. Then, we describe the method used to estimate the 21 cm power spectrum and validate it with sky simulations.
- In Chapter 5 we show the results of this Thesis work. Upper limits to EoR power spectrum are estimated and compared to previous works. We then use these values to calculate lower limits to the IGM temperature during the EoR.
- In Chapter 5.2 we summarize the results of this Thesis work and discuss future perspectives.

Chapter 1

The cosmological context

In this chapter, our aim is to provide a summary of the current cosmological scenario on which this dissertation is based. More details on the modern cosmology can be found, for instance, in Coles and Lucchin (2002) and Mukhanov (2005).

1.1 Fundamentals of Cosmology

Cosmology is the study of origin and evolution of our Universe. The fundamental assumption at the base of all cosmological models is the *cosmological principle*, introduced by Einstein (1917) in order to find exact solutions of the equations of his General Theory of Relativity (Einstein 1916). According to the principle, the Universe is spatially homogeneous (it is the same at any position) and isotropic (it looks the same in any direction) on large scales. A principle cannot be proved, but there are observational evidences both in the local universe, where the distribution of galaxies is homogeneous and isotropic on scales larger than about 100 Mpc, and at very high-redshift, where the distribution of the cosmic microwave background (CMB) anisotropies has a high degree of isotropy (Planck Collaboration et al. 2019).

1.1.1 Kinematics of the Universe

as the Universe is expanding and is a homogeneous and isotropic fluid of matter and energy (see §1.1.3), we can define the unique *cosmic time* t as the time at which the density of that fluid has a particular value. The expansion is described by the dimensionless function $a(t)$, known as *scale factor*, which is normalized such that $a(t_0) = 1$ at the present cosmic time t_0 ($0 < a(t) \leq 1$ in case of expansion). In the cosmological context there are two sets of coordinates: the *comoving coordinates*, that follow the expansion of the Universe, and the *proper coordinates*, that are the physical ones. Thus, the proper distance between two comoving observers at the time t is $r(t) = r(t_0)a(t)$, where $r(t_0)$ is the distance at the time t_0. Instead, the comoving distance between these observers is $x = r(t)/a(t)$ and hence is constant during the expansion (see §1.1.2). It follows that the comoving observer sees the Universe homogeneous and isotropic, because his motion is not influenced by the local matter distribution.

The relative speed of two comoving observers separated by $r(t)$ is

$$v(t) = \dot{r}(t) = x\dot{a}(t) = r(t)\frac{\dot{a}(t)}{a(t)} = r(t)H(t), \tag{1.1}$$

where $H(t)$ is the *Hubble parameter*. At the present time, $H(t_0) \equiv H_0$ is the *Hubble constant* and Eq. (1.1) becomes $v = H_0 r$, that is known as the *Hubble-Lemaître law* (Lemaître 1927; Hubble 1929). The value of H_0 is found to be positive, so, on large scales, the galaxies move away from each other with a speed proportional to their relative distance. This motion is due to the expansion of the Universe, that sets $\dot{a} > 0$, and is known as *Hubble flow*. The value of H_0 is not known with great accuracy and a tension between different methods occurs today: Riess et al. (2019) estimated a value of $H_0 = 74.24 \pm 1.82\,\mathrm{km\,s^{-1}\,Mpc^{-1}}$ from long-period Cepheids in the Large Magellanic Cloud, whereas Planck Collaboration et al. (2018b) measured $H_0 = 67.4 \pm 0.5\,\mathrm{km\,s^{-1}\,Mpc^{-1}}$ observing the CMB with the *Planck*[1] space mission. For this reason, a value of $H_0 \approx 70\,\mathrm{km\,s^{-1}\,Mpc^{-1}}$ is generally taken into account.

As a consequence of the Hubble flow, at the *Hubble time* $t_\mathrm{H} = H_0^{-1}$ the distance between galaxies was zero, then t_H provides an approximate estimate of the age of the Universe. In particular, we find $t_\mathrm{H} \approx 13.7\,\mathrm{Gyr}$. The precise value of the age of the Universe is obtained considering the evolution of $H(t)$ and hence is model-dependent (see §1.1.3). Furthermore, on small scales the Universe is not homogeneous and isotropic, and the gravitational attraction between galaxies can lead to a decrease in their relative speeds. Indeed, in these cases the Hubble flow is negligible, because the dynamics between galaxies dominates the effect of expansion and adds a peculiar velocity term to Eq. (1.1). Thus, two galaxies can approach each other rather than recede.

The relative motion between a source and an observer changes the radiation wavelength according to the Doppler effect. The consequently *redshift* is defined as

$$z \equiv \frac{\lambda_\mathrm{obs} - \lambda_\mathrm{em}}{\lambda_\mathrm{em}}, \tag{1.2}$$

where λ_em is the wavelength of a photon emitted by the source at time t_em and λ_obs is the wavelength of the same photon received by the distant comoving observer at time $t_\mathrm{obs} > t_\mathrm{em}$. In the cosmological context, there is no Doppler effect due to the motion of the source, but the photon wavelength changes because the Universe has expanded between t_em and t_obs by a factor $a(t_\mathrm{obs})/a(t_\mathrm{em})$:

$$\lambda_\mathrm{obs} = \frac{a(t_\mathrm{obs})}{a(t_\mathrm{em})}\,\lambda_\mathrm{em}. \tag{1.3}$$

If we consider the case in which $t_\mathrm{obs} = t_0$, we have $a(t_\mathrm{obs}) = 1$ and Eq. (1.2) can be written as

$$z = \frac{1}{a(t)} - 1, \tag{1.4}$$

where t_em has become a generic cosmic time t. As the Universe is expanding, $a(t) \leq 1$ and hence $z \geq 0$, with $z = 0$ at the present time, that is why today quantities are indicated with a subscript zero. The name "redshift" is due to the fact that in this case the observed wavelength is higher than the emitted one and hence shifted toward the red. Eq. (1.4) connects an observable quantity, i.e., z, to the expansion of the Universe, which can then be directly measured. Furthermore, the scale factor can be expressed as $a \equiv (1+z)^{-1}$: the redshift can be used to describe the cosmic time similar to the scale factor, taking into account that z increases when a decreases.

1.1.2 Cosmological distances

In order to calculate the distance between two points in the Universe, we have to define a metric. In particular, a good example of metric that takes into account the cosmological principle is the *Friedmann-Lemaître-Robertson-Walker metric*, in which the interval in the spacetime between two events at (t, x_1, x_2, x_3) and $(t + \mathrm{d}t, x_1 + \mathrm{d}x_1, x_2 + \mathrm{d}x_2, x_3 + \mathrm{d}x_3)$ is defined as

$$\mathrm{d}s^2 = c^2\mathrm{d}t^2 - \mathrm{d}r^2 = c^2\mathrm{d}t^2 - a^2(t)\left[\frac{\mathrm{d}x^2}{1 - Kx^2} + x^2\left(\mathrm{d}\theta^2 + \sin^2\theta\,\mathrm{d}\varphi^2\right)\right], \tag{1.5}$$

---

[1] http://www.esa.int/Planck

where we have used the comoving spherical coordinates x, θ and φ instead of the generic x_1, x_2 and x_3, K is the curvature parameter, that could be only $+1$, 0 or -1, and c is the light speed. Thus, the term in square brackets describes the geometry of the spacetime:

- when $K = +1$ the spacetime is a sphere, which represents a *closed Universe*;
- when $K = 0$ the spacetime is an Euclidean space, which represents a *flat Universe*;
- when $K = -1$ the spacetime is a 3D hyperboloid, which represents an *open Universe*.

Instead, the value of $\mathrm{d}s^2$ tells us if the interval is light-like ($\mathrm{d}s^2 = 0$), time-like ($\mathrm{d}s^2 > 0$) or space-like ($\mathrm{d}s^2 < 0$). In the cosmological context we are interested in the light-like intervals, which are the photon paths in a given geometry.

We define the *proper distance* as the physical distance measured between two points by an observer at the time t. For simplicity, we suppose that the observer is on the origin of the polar coordinate system, which is oriented so that θ and φ are constant along the path. Thus, from Eq. (1.5), the observer measures a proper distance between the origin and x given by:

$$r(t) = \int_0^x \frac{a(t)\,\mathrm{d}x'}{(1 - Kx'^2)^{1/2}} = a(t) f(x), \tag{1.6}$$

where values of $f(x)$ depend on the spacetime geometry:

$$f(x) = \begin{cases} \sin^{-1} x, & \text{for } K = +1 \\ x, & \text{for } K = 0 \\ \sinh^{-1} x, & \text{for } K = -1 \end{cases} .$$

The proper distance is an increasing function of time, as $a(t)$ increases as the expansion proceeds.

The *comoving distance* is instead the proper distance measured by the observer at a time t_{obs} with the comoving coordinates, which follow the Hubble flow and hence do not change while the Universe is expanding:

$$x = a(t_{\mathrm{obs}}) f(x) = \frac{a(t_{\mathrm{obs}})}{a(t)}\, r(t). \tag{1.7}$$

This distance does not change with time, as both $r(t)$ and $a(t)$ increase with time. Furthermore, if $t_{\mathrm{obs}} = t_0$, the comoving distance is $x = r(t)/a(t)$, expression that we already seen in the previous section.

Consider a photon emitted by a comoving source at the time t, placed in the origin of the coordinate system, and observed by a comoving observer at time t_{obs}, placed at a distance x. As photons travel along a path given by light-like intervals ($\mathrm{d}s^2 = 0$), from Eq. (1.6) we can write

$$f(x) = \int_0^x \frac{\mathrm{d}x'}{(1 - Kx'^2)^{1/2}} = \int_t^{t_{\mathrm{obs}}} \frac{c\,\mathrm{d}t'}{a(t')}. \tag{1.8}$$

In a flat Universe, the comoving distance between the source and the observer is then given by

$$x = \int_t^{t_{\mathrm{obs}}} \frac{c\,\mathrm{d}t'}{a(t')}. \tag{1.9}$$

From this expression, it can be shown that the comoving distance in terms of redshift is

$$x(z) = c \int_{z_{\mathrm{obs}}}^{z} \frac{\mathrm{d}z'}{H(z')}, \tag{1.10}$$

which is of practical usefulness, as we will see in §3.1.2.

Finally, we define the *horizon distance* as the (proper) distance that describes a region in causal connection with an observer at a given time t:

$$R_{\mathrm{H}}(t) = a(t)\int_0^t \frac{c\,\mathrm{d}t'}{a(t')}, \tag{1.11}$$

where two observers are in casual connection when they can exchange photons. So, the horizon distance defines the size of the observable Universe, that at the present time is $R_{\mathrm{H}}(t_0) \approx 14\,\mathrm{Gpc}$.

1.1.3 Dynamics of the Universe

The cosmology is based on the General Theory of Relativity, in which the Universe is described as a *perfect fluid*, homogeneous and isotropic in order to find solutions for the Einstein's equations. These solutions are known as *Friedmann equations* (Friedmann 1922) and describe the expansion of the Universe in terms of the scale factor $a = a(t)$:

$$\dot{a}^2 = \frac{8\pi G\rho}{3}\,a^2 - Kc^2 \tag{1.12a}$$

$$\ddot{a} = -\frac{4\pi G}{3}\left(\rho + \frac{3p}{c^2}\right)a, \tag{1.12b}$$

where G is the gravitational constant, ρ and p are, respectively, the energy density and pressure of the fluid, and K is the curvature parameter. As the Universe is a closed system, it is expanding without energy loss. So, the Friedmann equations above are linked by the adiabatic condition

$$\mathrm{d}\big(\rho c^2 a^3\big) = p\,\mathrm{d}a^3. \tag{1.13}$$

If we introduce the *critical density* of the Universe, defined as

$$\rho_{\mathrm{cr}}(t) \equiv \frac{3H^2(t)}{8\pi G}, \tag{1.14}$$

and the *density parameter*, defined as

$$\Omega(t) \equiv \frac{\rho(t)}{\rho_{\mathrm{cr}}(t)}, \tag{1.15}$$

the Friedmann equation (1.12a) can be written as

$$H^2(1-\Omega)a^2 = -Kc^2. \tag{1.16}$$

as the right-hand side is a constant, we can calculate the left-hand side at t_0, so that $H_0^2(1-\Omega_0) = -Kc^2$, where $\Omega_0 = \Omega(t_0)$. Thus, the value of Ω_0, and hence the value of $\rho_0 = \rho(t_0)$, determines the geometry of the Universe at all times:

- if $\Omega_0 = 1$, i.e., $\rho_0 = \rho_{0,\mathrm{cr}}$, we have $K = 0$, that means a flat Universe;
- if $\Omega_0 > 1$, i.e., $\rho_0 > \rho_{0,\mathrm{cr}}$, we have $K = 1$, that means a closed Universe;
- if $\Omega_0 < 1$, i.e., $\rho_0 < \rho_{0,\mathrm{cr}}$, we have $K = -1$, that means an open Universe.

The critical density is then the density that the Universe must have to be geometrically flat. At the present time, it has value given by

$$\rho_{0,\mathrm{cr}} = \rho_{\mathrm{cr}}(t_0) = \frac{3H_0^2}{8\pi G} \approx 1.9\cdot 10^{-29}h^2\,\mathrm{g\,cm^{-3}}, \tag{1.17}$$

where h is the *dimensionless Hubble constant* that parameterises the Hubble constant as $H_0 = 100h\,\mathrm{km\,s^{-1}\,Mpc^{-1}}$. Assuming $H_0 \approx 70\,\mathrm{km\,s^{-1}\,Mpc^{-1}}$, we have $h \approx 0.7$ and hence $\rho_{0,\mathrm{cr}} \approx 10^{-29}\,\mathrm{g\,cm^{-3}}$.

In ordinary condition, in which ρ and p are both non-negative, Eq. (1.12b) tells us that the Universe is decelerating, because $\ddot{a} < 0$. Furthermore, we know that the Universe is expanding, i.e., $\dot{a} > 0$, so $a(t)$ is an increasing monotone and concave down function. As a consequence, there is a time at which $a(t) = 0$ and it must be $t = 0$. This point sets the origin of the Universe and is known as the *Big Bang*. This name is a misnomer, because the Big Bang is not an explosion: the higher the pressure, the greater the deceleration, as opposed to an explosion. The expansion is due only to the initial conditions describing a homogeneous and isotropic Universe. All models based on the Friedmann equations (and hence on the cosmological principle and the perfect fluid) intrinsically include the Big Bang.

The perfect fluid within the Friedmann equations is a mixture of different components, having each one its particular mass density and pressure. In cosmology a general *equation of state* is used to describe such fluid:

$$p = w\rho c^2, \tag{1.18}$$

where w is a dimensionless parameter that assumes different values for different components. In general w is a function of redshift z, but for simplicity we assume it as a constant. If we substitute the the equation of state (Eq. 1.18) in the adiabatic condition (Eq. 1.13), we obtain

$$\rho_w = \rho_0\, a^{-3(1+w)} = \rho_0(1+z)^{3(1+w)}, \tag{1.19}$$

which describes the density evolution of each component through the cosmic history. In particular, the perfect fluid is made up of three main components:

- **Matter** It is a non-relativistic fluid with $p \ll \rho c^2$, made of baryonic matter and non-baryonic dark matter (DM; see §1.3). Assuming $p \approx 0$, the equation of state of this component has $w = 0$, so its density evolves as

  $$\rho_\mathrm{m} = \rho_{0,\mathrm{m}}\, a^{-3} = \rho_{0,\mathrm{m}}(1+z)^3. \tag{1.20}$$

- **Radiation** It is a relativistic fluid made of non-degenerate particles, such as photons or neutrinos, with a pressure given by

  $$p_\gamma = \frac{1}{3}\rho_\gamma c^2, \tag{1.21}$$

  where $w = 1/3$. Thus, the density of the radiation component evolves as

  $$\rho_\gamma = \rho_{0,\gamma}\, a^{-4} = \rho_{0,\gamma}(1+z)^4. \tag{1.22}$$

- **Dark Energy** It is an exotic fluid associated with the *cosmological constant* Λ (i.e., the vacuum energy), which has a pressure given by

  $$p_\Lambda = -\rho_\Lambda c^2, \tag{1.23}$$

  where $w = -1$. This means that its pressure is negative and could produce an accelerated expansion of the Universe, as we have $\ddot{a} > 0$ from Eq. (1.12b). The density of the dark energy component is constant with time:

  $$\rho_\Lambda = \rho_{0,\Lambda} = \mathrm{const.} \tag{1.24}$$

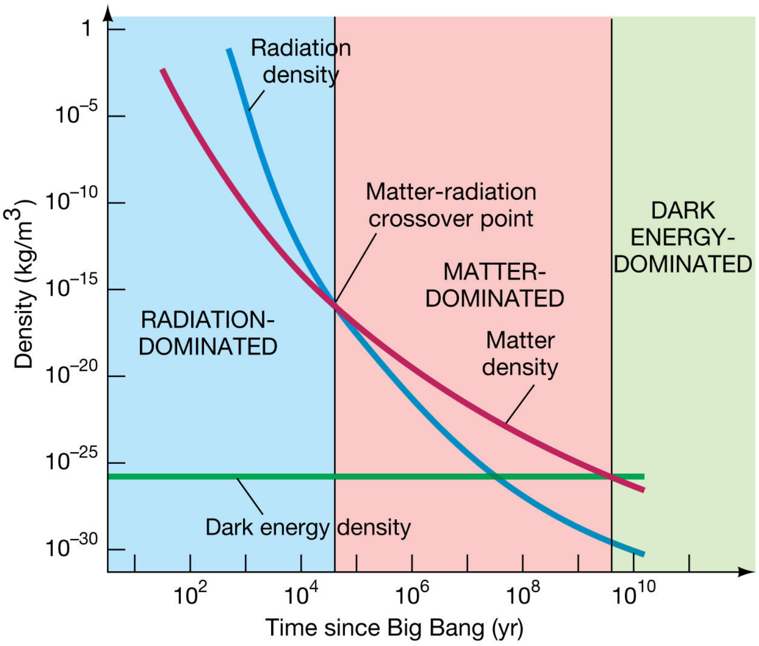

Figure 1.1 The density of the perfect fluid as a function of time. The three different colored lines show the evolution of the density for radiation (blue), matter (red) and dark energy (green). In the early Universe the radiation is the dominant component, until the time of matter-radiation equivalence after which matter becomes the dominant one. The equivalence time between matter and dark energy is at a time close to t_0, after which the latter becomes the dominant component until today. From `https://pages.uoregon.edu/jimbrau/BrauImNew/Chap27`, credits to 2011 Pearson Education.

The evolution of these densities as a function of the cosmic time is shown in Figure 1.1. The density parameters of matter, radiation and dark energy are respectively defined as $\Omega_{\rm m} \equiv \rho_{\rm m}/\rho_{\rm cr}$, $\Omega_\gamma \equiv \rho_\gamma/\rho_{\rm cr}$ and $\Omega_\Lambda \equiv \rho_\Lambda/\rho_{\rm cr}$, then $\Omega_0 = \Omega_{0,\Lambda} + \Omega_{0,{\rm m}} + \Omega_{0,\gamma}$.

Using the definition of critical density (Eq. 1.14) and Eq. (1.19), we can write Eq. (1.16) as

$$H^2 = H_0^2\,E^2(z) = H_0^2\left[\Omega_{0,\Lambda} + \Omega_{0,K}(1+z)^2 + \Omega_{0,{\rm m}}(1+z)^3 + \Omega_{0,\gamma}(1+z)^4\right], \qquad (1.25)$$

where $\Omega_{0,K} = 1 - \Omega_0$ is a sort of density parameter that describes the contribution of the space curvature of the Universe, similarly to K. Thus, the evolution of the Hubble parameter is model-dependent.

1.2 The ΛCDM model

From the Friedmann model, we know how the components of the Universe evolve through the cosmic history, but there is no information about the value of the density parameters. So, in order to put constraints on the different cosmological models (flat, open, closed), we need observations. In particular, the most accurate estimates come from the analysis and modelling of the CMB (see §1.2.3) and from its weak gravitational lensing, both probed by the *Planck* satellite (Planck Collaboration et al. 2018b; 2019). The main values of these parameters, measured at the present time, are reported in Table 1.1, where we introduced the baryon and the cold dark matter (CDM) density parameters, respectively $\Omega_{0,{\rm b}}$ and $\Omega_{0,{\rm c}}$. The cold DM is necessary to explain the hierarchical structure formation (see §1.3.1), that in the presence of a dominant hot DM component can not take place. As $\Omega_{0,K} \approx 0$, we can safely say that the Universe is flat. A cosmological model in which the Universe is geometrically flat, follows the Friedmann equations, has a dark energy component associated to Λ and in which the DM is cold, is known as *ΛCDM model.* This is the currently accepted and most used cosmological

$\Omega_{0,\Lambda}$	$\Omega_{0,\mathrm{m}}$	$\Omega_{0,\gamma} \cdot 10^5$	$\Omega_{0,\mathrm{c}} h^2$	$\Omega_{0,\mathrm{b}} h^2$	$\Omega_{0,K}$
0.685 ± 0.007	0.315 ± 0.007	9.3 ± 0.2	0.120 ± 0.001	0.0224 ± 0.0002	-0.009 ± 0.006

Table 1.1 Density parameters from Planck Collaboration et al. (2018a) for the ΛCDM model. All values are given at a confidence level of 68%, except the last one which is at 95%. The radiation density parameter $\Omega_{0,\gamma}$ is calculated from Eq. (1.30) using $z_{\mathrm{eq}} = 3402 \pm 26$.

model – the concordance model – as it is supported by many independent observational probes, such as the primordial nucleosynthesis (Beringer et al. 2012), the power spectrum of large scale structure (Tegmark et al. 2006) and, as we already said, the CMB.

1.2.1 Radiation, matter and dark energy eras

Knowing the values of the today matter, radiation and dark energy density parameters and the relative slopes of the curves described by Eq. (1.19), it is possible to follow the evolution of these three components through the cosmic history.

We have seen that the Friedmann equations predict a decelerating and expanding Universe. However, there are observational evidence, such as those from Type Ia Supernovae (SNIa) (Perlmutter et al. 1999), that the expansion rate is currently accelerating due to the presence of the dark energy. In order to quantify the time variation of the expansion of the Universe, we introduce the *deceleration parameter*:

$$q(t) \equiv -\frac{\ddot{a}a}{\dot{a}^2}, \tag{1.26}$$

which is positive when the Universe decelerates ($\ddot{a} < 0$) and negative when accelerates ($\ddot{a} < 0$). In a model in which matter and dark energy dominate, this parameter can be written as

$$q = \frac{\Omega_{\mathrm{m}}}{2} - \Omega_{\Lambda}, \tag{1.27}$$

which is $q_0 \approx -0.55$ in the ΛCDM model. Thus, there must have been a time in the history of the Universe after which the repulsive effect of the dark energy, whose density is a fixed constant, begins to dominate over the attractive effect of matter and radiation, whose densities, on the other hand, decrease as the expansion proceeds. At that time, that we indicate as z_{flex}, the function $a(t)$ has a flex and $q = 0$, so from Eq (1.27) we have $\Omega_{\mathrm{m}}(z_{\mathrm{flex}}) = 2\Omega_{\Lambda}(z_{\mathrm{flex}})$. Using Eq. (1.24) for $\Omega_{\Lambda}(z_{\mathrm{flex}})$ and Eq. (1.20) for $\Omega_{\mathrm{m}}(z_{\mathrm{flex}})$, we obtain

$$\Omega_{0,\mathrm{m}}(1 + z_{\mathrm{flex}})^3 = 2\Omega_{0,\Lambda}, \tag{1.28}$$

from which $z_{\mathrm{flex}} \approx 0.6$. Thus, for $z > z_{\mathrm{flex}}$ the expansion of the Universe is decelerating, while for $z < z_{\mathrm{flex}}$ it is accelerating.

The flex is not, however, the time at which the dark energy density becomes dominant over the matter density. This time, indicated with $z_{\mathrm{eq},\Lambda}$, is known as *Λ-matter equivalence* and occurs when $\rho_{\Lambda} = \rho_{\mathrm{m}}$. Using Eq. (1.24) for $\Omega_{\Lambda}(z_{\mathrm{eq},\Lambda})$ and Eq. (1.20) for $\Omega_{\mathrm{m}}(z_{\mathrm{eq},\Lambda})$, we obtain

$$\Omega_{0,\Lambda} = \Omega_{0,\mathrm{m}}(1 + z_{\mathrm{eq},\Lambda})^3, \tag{1.29}$$

from which $z_{\mathrm{eq},\Lambda} \approx 0.3$. For $z > z_{\mathrm{eq},\Lambda}$ the matter is the dominating component. However, its density evolves with redshift slower than the radiation density, so there is a point where $\rho_{\mathrm{m}} = \rho_{\gamma}$. This occurs at the time of *matter-radiation equivalence*, often referred as time of *equivalence*, as it is more important than $t_{\mathrm{eq},\Lambda}$ as we will see in §1.4.3, and indicated with z_{eq}. Using Eq. (1.20) for $\Omega_{\mathrm{m}}(z_{\mathrm{eq}})$ and Eq. (1.22) for $\Omega_{\gamma}(z_{\mathrm{eq}})$, we obtain

$$\Omega_{0,\mathrm{m}} = \Omega_{0,\gamma}(1 + z_{\mathrm{eq}}), \tag{1.30}$$

Generic EdS (w)	Matter EdS ($w = 0$)	Radiation EdS ($w = 1/3$)
$a = (t/t_0)^{\frac{2}{3(1+w)}}$	$a \propto t^{2/3}$	$a \propto t^{1/3}$
$t = t_0(1+z)^{-3(1+w)/2}$	$t \propto (1+z)^{-3/2}$	$t \propto (1+z)^{-2}$
$H = H_0(1+z)^{3(1+w)/2}$	$H = H_0(1+z)^{3/2}$	$H = H_0(1+z)^{2}$
$\rho_w = \frac{1}{6\pi G(1+w)^2 t^2}$	$\rho_{\mathrm{m}} = \frac{1}{6\pi G t^2}$	$\rho_\gamma = \frac{3}{32\pi G t^2}$

Table 1.2 Main cosmological quantities for the EdS models.

from which $z_{\mathrm{eq}} \approx 3400$. An accurate value of $z_{\mathrm{eq}} = 3402 \pm 26$ was estimated by Planck Collaboration et al. (2018a). Thus, we can identify three major epochs in the ΛCDM Universe, also shown in Figure 1.1: between the Big Bang and z_{eq} there has been a *radiation-dominated era*, after which there has been a *matter-dominated era* until $z_{\mathrm{eq},\Lambda}$, which marks the beginning of the *dark energy-dominated era*.

The present time is quite near the Λ-matter equivalence, so the dark energy dominates over the matter component but the latter is not negligible, as it is about 30% of the total density of the Universe. However, far enough from the time of equivalence we can approximate the Universe as a one-component model, i.e., a radiation-only Universe in the radiation era and a matter-only Universe in the matter era. A flat Universe with $\Omega_w = 1$ and only one component with densityρ_w is known as *Einstein-de Sitter (EdS) model* (Einstein and de Sitter 1932). In Table 1.2 are summarized the main relations for a generic EdS Universe with equation of state parameter w, for a matter-only Universe with $w = 0$, and for a radiation-only Universe with $w = 1/3$.

1.2.2 Thermal history of the early Universe

In the early Universe the dominant component is the radiation, whose temperature can be used as a cosmic clock, as well as time and redshift, since it decreases as the Universe expands:

$$T_\gamma(z) = T_{0,\gamma}(1+z), \tag{1.31}$$

where $T_{0,\gamma} \approx 2.73\,\mathrm{K}$ is the today temperature (see §1.2.3). Furthermore, Thomson scattering between photons and electrons in the hot primordial plasma keeps coupled the matter to the radiation fluid, and hence $T_\gamma = T_{\mathrm{m}}$. Thus, we can describe the *thermal history* of the Universe following the evolution of the radiation temperature until the matter-radiation decoupling, that occurred during the recombination.

The Big Bang is the point at which the Universe has been originated, but we can not investigate the times before $t_{\mathrm{P}} \approx 10^{-43}\,\mathrm{s}$, known as *Planck time*, as we can not apply the General Relativity to describe the Universe in that epoch. Indeed, the quantum effects are not negligible, but actually we do not have a solid quantum-gravity theory that can help us to include them. However, near t_{P} the General Relativity and hence the Friedmann equations are valid and the Universe has a temperature of about $10^{32}\,\mathrm{K}$. At that energy, all four interactions (gravitational, electromagnetic, weak and strong) are combined as one "super force" (Bennett et al. 2009). When the temperature drops below $10^{32}\,\mathrm{K}$, gravity separates from the other three forces, which remain united according to the Grand Unified Theory (GUT; Buras et al. 1978) until the temperature is about $10^{29}\,\mathrm{K}$. That temperature is reached $10^{-38}\,\mathrm{s}$ after the Big Bang. The separation of the electroweak from the strong nuclear interaction releases an enormous amount of energy in only $10^{-36}\,\mathrm{s}$, causing a sudden acceleration, known as *inflation*, in the expansion of the Universe, which grows by a factor 10^{60} (Linde 2008). According to Sakharov (1967), this is also the only time during which conservation of baryons number can be violated and baryogenesis may occur, that is the generation of an asymmetry between particles and antiparticles. In the Standard Model of particle physics, however, according to Shaposhnikov (1987), the baryogenesis takes place during the electroweak era. This period lasts until the temperature drops to $10^{15}\,\mathrm{K}$, approximately $10^{-10}\,\mathrm{s}$ after the Big Bang, when the electromagnetic force separates from the weak nuclear interaction and elementary particles, such as photons, gluons and quarks, are formed.

At the age of $10^{-5}\,\mathrm{s}$, the Universe has a temperature of $10^{12}\,\mathrm{K}$, which is low enough to allow the formation of hadrons. Protons and neutrons start to fuse, forming heavier nuclei and initiating the *primordial nucleosynthesis* (Fuller et al. 1988). When the fusion ceases, approximately 300 s after the Big Bang and at a temperature of $10^{9}\,\mathrm{K}$, the Universe is still made up of 75% protons, while the other 25% was helium nuclei with trace of lithium and deuterium. This hot plasma is also formed by electrons, which constantly scatter photons. The coupling between baryons and radiation prevents the formation of neutral atoms until the temperature is about 3000 K and the Universe is 380 000 years old, corresponding to $z_{\mathrm{rec}} \approx 1100$ (Kamionkowski 2007; Bennett et al. 2009). At that moment the *recombination* begins and electrons bind to protons in order to form neutral hydrogen atoms (Peebles 1968; Zeldovich et al. 1968). As a consequence, the *decoupling* between matter and radiation occurs at $z_{\mathrm{dec}} \approx 200$ and the photons are finally able to propagate, making the Universe transparent. We can see that relic radiation today as the cosmic microwave background. The gas constituted by the newly formed neutral atoms starts to cool faster than the radiation fluid, so that its kinetic temperature evolves as

$$T_{\mathrm{k}}(z) \approx T_{\mathrm{m}}(z) \propto (1+z)^2. \tag{1.32}$$

1.2.3 The Cosmic Microwave Background

The existence of a cosmic microwave background radiation (CMB) was predicted at the end of 1940s (Gamow 1946; Alpher and Herman 1949) and it was effectively observed in 1965 (Penzias and Wilson 1965; Dicke et al. 1965). The CMB spectrum is the best black-body known in nature (Fixsen 2009), with a today temperature $T_{0,\gamma} \approx 2.73\,\mathrm{K}$, and it is almost isotropic, according to the cosmological principle. Thus, the CMB has a cosmological origin, as its photons are the components of the radiation fluid that, due to the expansion of the Universe, has cooled from $10^{32}\,\mathrm{K}$ at the Planck time to 2.73 K at $z = 0$.

When we observe the CMB, we have to take into account that we are not comoving observers, as the Solar System has a motion with respect to the Hubble flow. Thus, there is a dipole anisotropy along the direction of the motion (i.e., on an angular scales of 180°) with a temperature fluctuation $\Delta T_\gamma / T_\gamma \approx 1.3 \cdot 10^{-3}$. Subtracting this anisotropy, we find other small temperature fluctuations over the sky with values $\Delta T_\gamma / T_\gamma \approx 10^{-5}$ due to three main processes:

- **Gravity.** As we will see in §1.3, at the time of decoupling the Universe is not homogeneous and isotropic on small scales, but there are density fluctuations in the DM component. Indeed, the DM particles are collisionless, so they decouple from photons before baryons and have the time to grow, forming potential wells and peaks. Thus, a CMB photon is subject to redshift (i.e., it loses energy) if at the decoupling time it is in a potential well, while, on the other hand, it is subject to blueshift (i.e., it gains energy) if it is in a potential peak.

- **Density.** Assuming adiabatic fluctuations, if photons are in a overdense region at the decoupling time, they can be more energetic than those photons coming from less dense region. This process is in competition with the gravity.

- **Velocity.** The (peculiar) velocity field generates a Doppler effect on photons: if they are receding from us, they are redshifted, while if they are approaching us, they are blueshifted.

Thus, the *CMB temperature anisotropies* are due to the fact that photons do not move in an empty space. Studying these fluctuations, we can get valuable information about the matter distribution in the primordial Universe and hence improve our understanding on galaxy formation.

Figure 1.2 shows the observed map of the CMB fluctuations $\Delta T_\gamma(\theta,\varphi)/T_\gamma$, where θ and φ are the spherical angular coordinates on the sky, as we assume that the CMB is distributed on a spherical surface. Thus, the temperature fluctuations can be decomposed in spherical harmonics using the Fourier-Legendre series:

$$\frac{\Delta T_\gamma}{T_\gamma}(\theta,\varphi) = \sum_{\ell=0}^{\infty}\sum_{m=-\ell}^{\ell} a_{\ell m} Y_{\ell m}(\theta,\varphi), \tag{1.33}$$

where $\ell \propto 1/\theta$ is the multipole index, m is associated to the direction of observation φ (for a given ℓ, there are $2\ell+1$ possible directions), and $Y_{\ell m}$ are the spherical harmonics that include the Lagrange polynomials $P_\ell^m(\cos\theta)$. The term $a_{\ell m}$ is generally complex and is defined such as $\langle a_{\ell m}\, a^*_{\ell' m'}\rangle = C_\ell\, \delta_{\ell\ell'}\delta_{mm'}$, where the average is done over an ensemble of realisations, $\delta_{\ell\ell'}$ and $\delta_{mm'}$ are the Kronecker delta, and C_ℓ is the *CMB angular power spectrum*:

$$C_\ell = \langle |a_{\ell m}|^2\rangle = \frac{1}{2\ell+1}\sum_{m=-\ell}^{\ell} a^2_{\ell m}. \tag{1.34}$$

For $\ell = 0$ we have the monopole term, which is zero because it describes the temperature variation on scales $\theta = 360^\circ$, i.e., the mean value. The dipole term $\ell = 1$, instead, correspond to $\theta = 180^\circ$, the quadrupole term $\ell = 2$ to $\theta = 90^\circ$, and so on.

Figure 1.3 shows the CMB power spectrum observed by Planck Collaboration et al. (2018a), where there are several peaks, due to the harmonic oscillations of baryons. Indeed, before the decoupling, baryons can not collapse within the DM potential well because of the radiation pressure of photons. These oscillations occurred at the sound speed, so they are known as *baryon acoustic oscillations* (BAO). The physical interpretation of the first two peaks is the following:

- The first peak corresponds to $\ell_\mathrm{H} \approx 220$, i.e., to a scale $\theta_\mathrm{H} \approx 1^\circ$, and it is due to the first maximum compression of acoustic oscillations, that occurs when baryons are at the bottom of the DM potential well and on the horizon scale at the decoupling time. The position of this peak is a measure of the geometry of the Universe, i.e., of Ω_0, as the angular scale under which we observe the horizon changes as the curvature changes ($\ell_\mathrm{H} < 220$ if the Universe is closed, $\ell_\mathrm{H} > 220$ if the Universe is open).

- The second peak corresponds to $\ell \approx 500$, i.e., to a scale $\theta \approx 0.4^\circ$, and it is due to the first maximum rarefaction of acoustic oscillations. The baryons are near the edge of the DM potential well and the higher the baryons density ρ_b, the greater the difference between first and second peak. Thus, we can measure that difference in order to constrain the baryon density parameter $\Omega_\mathrm{b} \equiv \rho_\mathrm{b}/\rho_\mathrm{cr}$.

All the odd peaks are due to compression, while all the even peaks are due to rarefaction. At the smaller angular scale, i.e., largest ℓ, dissipation effects become important and the acoustic peaks are dampened.

1.3 Cosmological structure formation

The currently accepted model of structure formation is based on the collapse of baryonic matter within dark matter halos, which are generated from the growth of small perturbations

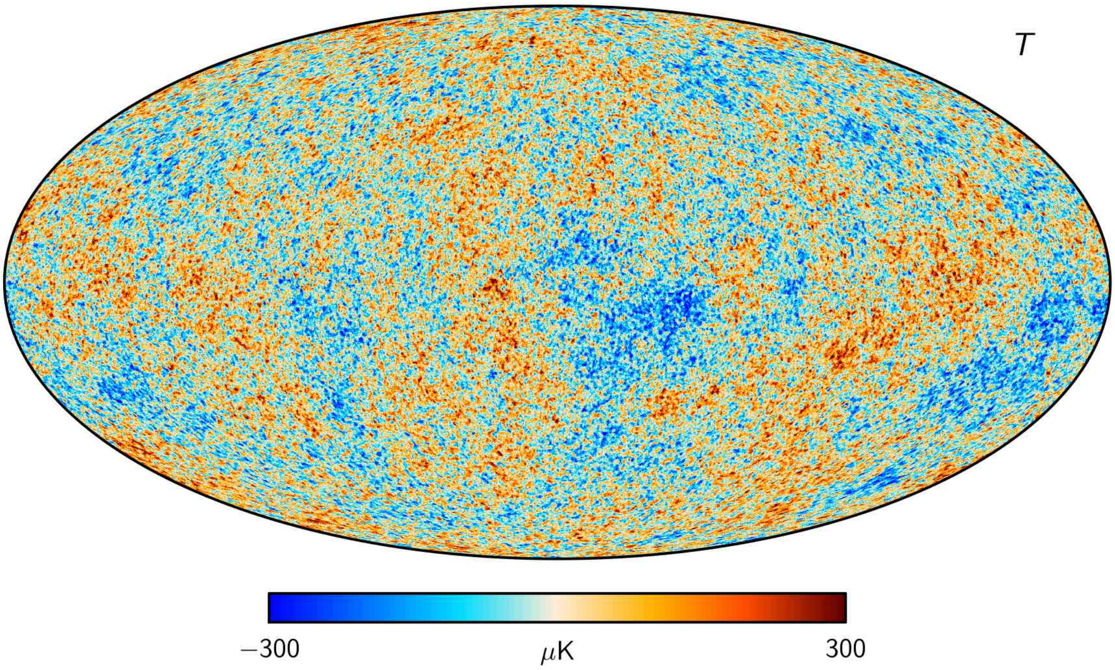

Figure 1.2 CMB temperature map obtained from Planck Collaboration et al. (2018a) after removal of the dipole component and average over frequencies. From `http://pla.esac.esa.int/pla/#maps`.

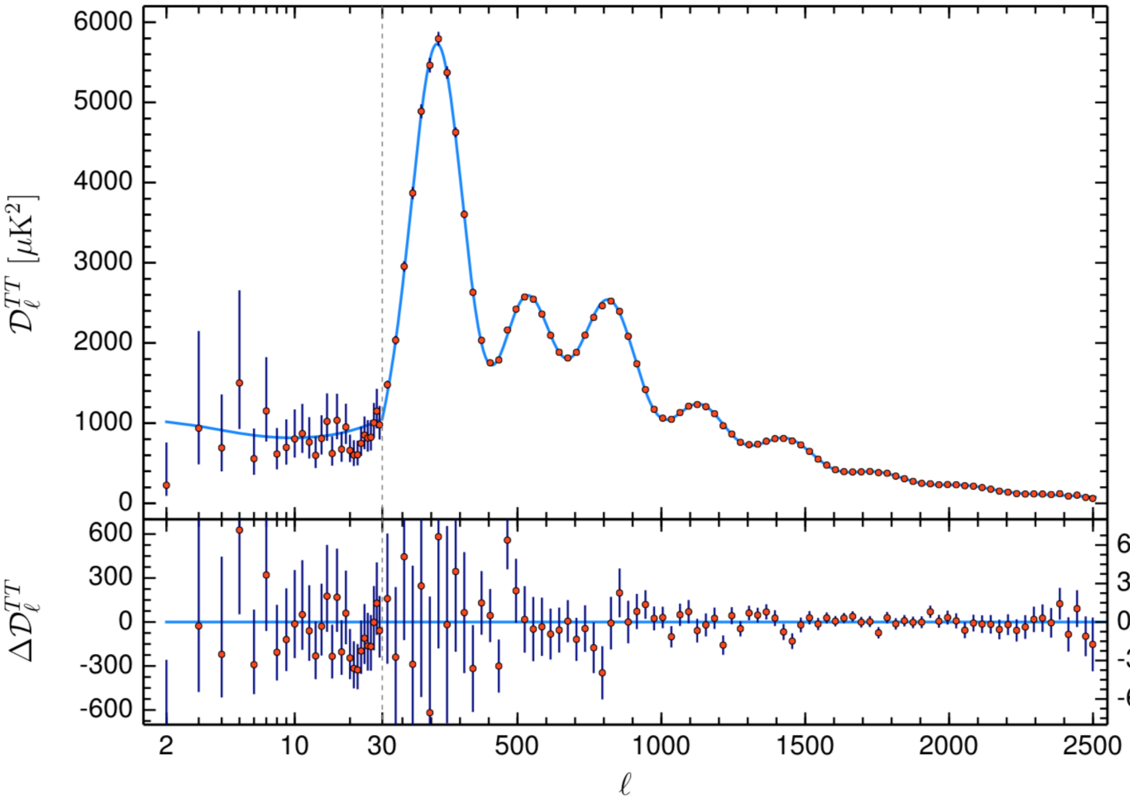

Figure 1.3 In the top panel the observed angular power spectrum of CMB temperature anisotropies is shown with red points, whereas the ΛCDM theoretical best fit is plotted as light blue curve. In the lower panel residual between the model and the data are shown. The error bars are given at a confidence level of 68%. Note that $\mathcal{D}_\ell^{TT} = \ell(\ell+1)C_\ell/(2\pi)$, where C_ℓ is given by Eq. (1.34). From Planck Collaboration et al. (2018b).

in the primordial matter density distribution of the Universe (see §1.3.1). The dark matter is so called because its particles do not interact electromagnetically, neither with other DM particles nor with the baryonic ones. Thus, we can probe its existence only through gravitational effects. The first evidence of DM was inferred by Zwicky (1933) through dynamical studies on the Coma galaxy cluster.[2] After that, the evidence of the DM presence was found studying the velocity dispersion in elliptical galaxies (Loewenstein and White 1998) and the rotation curves of spiral galaxies (Fuchs 2001), in the gravitational lensing (Li et al. 2016), and in the X-ray emitting gas (Buote and Canizares 1994).

The real difficulty concerning the DM is about its nature. The currently accepted model distinguishes between *hot dark matter* (HDM) and *cold dark matter* (CDM) depending on the thermal speed of particles at the decoupling time, which is much before the baryon-photon decoupling $z_{\rm dec}$. Indeed, in the early Universe all particles are coupled to the radiation fluid and hence are relativistic. The time at which a particle with mass $m_{\rm X}$ becomes non-relativistic is given by the equilibrium between thermal and rest energies:

$$k_{\rm B}T_\gamma = m_{\rm X}c^2, \tag{1.35}$$

where $k_{\rm B}$ is the Boltzmann constant. Thus, more massive particles become non-relativistic before less massive ones, because $T_\gamma \propto z$. This is the case of CDM, whose particles are more massive than HDM and hence become non-relativistic well before the DM-radiation decoupling. On the other hand, the HDM is made up of low-mass particles, such as neutrinos, that are still relativistic at the decoupling. Note that any decoupling is determined by the collisional timescale between a given particle and radiation. In the case of DM, the interaction with photons is really small, so the collisional timescale is much higher than the Hubble time and the DM-radiation decoupling occurs well before the matter-radiation equivalence.

1.3.1 Evolution of density perturbations

In order to form cosmic structures, the Universe can not be homogeneous, but there must be small perturbations that grow and then collapse into galaxies. These primordial perturbations are generated when the inflation ends (see §1.2.2) and we describe them with a dimensionless quantity known as *density contrast*:

$$\delta \equiv \frac{\delta\rho}{\rho} = \frac{\rho - \overline{\rho}}{\overline{\rho}}, \tag{1.36}$$

where $\overline{\rho} = \overline{\rho}(t)$ is the mean density of the Universe at the time t. As $\rho \geq 0$, the density contrast interval is $-1 \leq \delta \leq +\infty$, so there are both overdense and underdense regions in the Universe, but only the overdense ones can grow and form cosmic structures. Originally the perturbations are small, such that $|\delta| \ll 1$, and they evolve in a *linear regime*. Let us consider an overdense region, i.e., with $\delta > 0$, that expands in a EdS Universe, for simplicity. Because of its self-gravity, the perturbation expands slower than the Universe and the density contrast increases as the time passes. When the perturbation reaches $\delta \approx 1$, it enters the *non-linear regime*, in which the evolution of δ can not more be described analytically, and starts to recollapse as a consequence of its gravity. Finally, the perturbation becomes a virialised system, i.e., a bound structure known as *dark matter halo*. These halos start forming before the baryon-radiation decoupling and so, at $z_{\rm dec}$, the baryon density perturbations catch up the DM ones and after a certain time they grow with the same rate.

However, it is not enough to have an overdense region to form structures, but its mass must be also higher than the *Jeans mass*, which is defined as

$$M_{\rm J} = \frac{4\pi}{3}\rho_{\rm m}\lambda_{\rm J}^3, \tag{1.37}$$

---

[2] Zwicky was the first to refer to this non-baryonic component as dark matter.

where λ_J is the Jeans length, defined as $\lambda_\mathrm{J} \propto v/\sqrt{G\rho}$, where v is the thermal velocity of particles constituting the dominant component of the matter distribution with density ρ. As CDM and HDM have different velocities, i.e., $v_\mathrm{CDM} \ll v_\mathrm{HDM}$, we expect $\lambda_\mathrm{J,HDM} \gg \lambda_\mathrm{J,CDM}$ and hence $M_\mathrm{J,HDM} \gg M_\mathrm{J,CDM}$. Thus, there are two possible formation scenarios depending on which component dominates:

- **Bottom-up scenario.** The CDM component dominates on the HDM. The Jeans mass is $M_\mathrm{J} \approx 10^5\,\mathrm{M}_\odot$, similar to today globular cluster mass, which means that low-mass structures form first and then they aggregate into more massive ones. This scenario is also known as hierarchical structure formation.

- **Top-down scenario.** The HDM component dominates on the CDM. The Jeans mass is $M_\mathrm{J} \approx 10^{16}\,\mathrm{M}_\odot$, which is larger then today galaxy clusters mass. This means that very high-mass structures, like large pancakes, form first and then generate less massive ones through fragmentation.

The top-down scenario is not supported by observations, as the most distant galaxy cluster is observed at $z \approx 2$ (Wang et al. 2016). Thus, the CDM scenario is the preferred one to explain the structure formation, as there are observed galaxies up to $z \approx 11$ (Oesch et al. 2016).

1.4 Statistical properties of cosmological perturbations

The density perturbation δ is a *stochastic field* generated by random processes at the end of inflation. Thus, we can study the statistical properties of this field. However, in cosmology there is the problem that the Universe is only one and hence we can not repeat measures several times. For this purpose, we take into account the *ergodic principle*: the average over several realisations of a universe is equivalent to the average over separate volumes of a single Universe. This principle is also known as *fair sample*. The volumes must be enough large, that means $V \gg l_\mathrm{str}^3$, where l_str is the maximum scale at which we can find a structure due to perturbation growth. Thus, the volume dimension is a function of time and non-linearity level. For example, today $V^{1/3} \gg 500\,\mathrm{Mpc}$. We can apply the ergodic principle because of the cosmological principle, i.e., the stochastic processes that affect a region of the Universe are on average similar to those affecting a different region, but they are a different random realisation of the same process.

Inside a volume V the density perturbation $\delta(\mathbf{x})$, defined in comoving coordinates $\mathbf{x}$, can be decomposed as

$$\delta(\mathbf{x}) = \frac{1}{(2\pi)^3} \int \tilde{\delta}(\mathbf{k})\, e^{i\mathbf{k}\cdot\mathbf{x}}\, \mathrm{d}^3k, \tag{1.38}$$

where $\mathbf{k}$ is the Fourier conjugate of $\mathbf{x}$ and $\tilde{\delta}(\mathbf{k})$ is the perturbation density expressed in the Fourier space, such that

$$\tilde{\delta}(\mathbf{k}) = \int \delta(\mathbf{x})\, e^{-i\mathbf{k}\cdot\mathbf{x}}\, \mathrm{d}^3x. \tag{1.39}$$

Note that, as $\delta(\mathbf{x})$ is a real number, we have $\tilde{\delta}^*(\mathbf{k}) = \tilde{\delta}(-\mathbf{k})$. Perturbations are generated by random processes, so $\tilde{\delta}(\mathbf{k})$ has random imaginary part. This means that there is no correlation between phases of different $\tilde{\delta}(\mathbf{k})$. Thus, the distribution of these complex values is *Gaussian*:

$$\mathcal{P}(\delta) = \frac{1}{2\pi\sigma^2} \exp\left[-\frac{(\bar{\delta}-\delta)^2}{2\sigma^2}\right], \tag{1.40}$$

where $\bar{\delta} = 0$ as it is the fluctuation mean. Thus, the only quantity defining the density field is the variance σ^2. If we consider several realisations, we expect the values of $\tilde{\delta}(\mathbf{k})$ to be distributed around a quantity known as power spectrum.

1.4.1 Correlation function and power spectrum

The statistical properties of the perturbation field $\delta(\mathbf{x})$ can be described by the *correlation function*:

$$\xi(x) = \langle \delta(\mathbf{x}') \, \delta(\mathbf{x}' + \mathbf{x}) \rangle, \tag{1.41}$$

where $x = |\mathbf{x}|$ and the average is done over $\mathbf{x}'$. The correlation function describes the (auto)correlation of the field δ with itself in positions that are distant $\mathbf{x}$ from a given $\mathbf{x}'$. As the average is done over all directions, ξ is only function of the magnitude of $\mathbf{x}$.

Eq. (1.41) can be written as Fourier transform:

$$\xi(x) = \frac{1}{(2\pi)^6} \int \mathrm{d}^3 k \int \langle \tilde{\delta}(\mathbf{k}) \, \tilde{\delta}(\mathbf{k}') \rangle \, e^{i\mathbf{k}\cdot(\mathbf{x}'+\mathbf{x}) + i\mathbf{k}'\cdot\mathbf{x}'} \, \mathrm{d}^3 \mathbf{k}', \tag{1.42}$$

where

$$\langle \tilde{\delta}(\mathbf{k}) \, \tilde{\delta}(\mathbf{k}') \rangle = (2\pi)^3 \, P(k) \, \delta_{\mathrm{D}}(\mathbf{k} + \mathbf{k}'), \tag{1.43}$$

in which the average is done over different realisations of the perturbation field, δ_{D} is the Dirac delta function and $P(k)$ is the *power spectrum* of density fluctuations at the wavenumber $k = |\mathbf{k}|$. As $\delta_{\mathrm{D}}(\mathbf{k} + \mathbf{k}') \neq 0$ if and only if $\mathbf{k} = -\mathbf{k}$, Eq. (1.42) can be rewritten as

$$\xi(x) = \frac{1}{(2\pi)^3} \int P(k) \, e^{i\mathbf{k}\cdot\mathbf{x}} \, \mathrm{d}^3 k \tag{1.44}$$

and, as a consequence, we have

$$P(k) = \int \xi(x) \, e^{-i\mathbf{k}\cdot\mathbf{x}} \, \mathrm{d}^3 x. \tag{1.45}$$

Thus, $P(k)$ and $\xi(x)$ are a Fourier transform pair. From Eq. (1.43), the power spectrum can be defined as

$$P(k) = V \, \langle |\tilde{\delta}(\mathbf{k})|^2 \rangle \tag{1.46}$$

and then it measures the amount of perturbations on scale $R = 2\pi/k$. The power spectrum is a fundamental quantity because its volume integral is the variance of the perturbation field:

$$\sigma^2 = \frac{1}{2\pi^2} \int_0^\infty P(k) k^2 \, \mathrm{d}k \tag{1.47}$$

which is only function of time, as the amplitude of the perturbation evolves as the Universe expands.

1.4.2 The mass variance

The density field $\delta(\mathbf{x})$ is a continuous quantity and measuring it is difficult, because we can only get discrete information from luminous sources which form in the overdense regions. Thus, we have no direct information about voids and dark matter regions. To study the density field, we have to count the number of galaxies (or galaxy clusters) within a given volume V, which plays the role of a filter. The density contrast of galaxies is defined as

$$\delta_{\mathrm{gal}} = \frac{N_{\mathrm{gal}}(V) - \overline{N}_{\mathrm{gal}}(V)}{\overline{N}_{\mathrm{gal}}(V)}. \tag{1.48}$$

Similarly, we can define the density contrast of matter as

$$\delta_M = \frac{M(V) - \overline{M}(V)}{\overline{M}(V)}. \tag{1.49}$$

As we know very little about galaxy formation processes, we parametrize this ignorance with a *bias* b, such that $\delta_{\text{gal}} \equiv \delta_M$. Assuming $b = \text{const}$ – i.e., a linear relation between the galaxies number and the total mass within a volume – we can obtain $\delta(\mathbf{x})$ from δ_M through a convolution with a window function $W(R)$ within a radius $R \propto V^{1/3}$:

$$\delta_M(\mathbf{x}) = \delta(\mathbf{x}) * W(R). \tag{1.50}$$

Filtering $\delta(\mathbf{x})$ with $W(R)$ means smoothing it on scales smaller than R, because an averaging is done. The *mass variance* of δ_M is then defined as

$$\sigma_M^2 = \frac{1}{2\pi^2} \int_0^\infty P(k) \widetilde{W}^2(k, R) k^2 \, \mathrm{d}k, \tag{1.51}$$

where $\widetilde{W}(k, R)$ is the Fourier transform of $W(R)$. Note that $\sigma_M^2 \leq \sigma^2$:

- if $R \to 0$, we have $\delta_M(\mathbf{x}) = \delta(\mathbf{x})$, that means $\sigma_M^2 \to \sigma^2$;
- if $R \to \infty$, we have $\delta_M(\mathbf{x}) \to 0$, that means $\sigma_M^2 \to 0$.

The variance is expected to decrease for increasing R, as the filter averages down small scales fluctuations.

1.4.3 Evolution of power spectrum

The primordial power spectrum can be described as a power-law:

$$P_{\text{prim}}(k) = A_{\text{s}} k^{n_{\text{s}}}, \tag{1.52}$$

where A_{s} is the scalar amplitude and n_{s} is the scalar spectral index. If perturbations are originated by inflation, it is expected $n_{\text{s}} \approx 1$ (Harrison 1970; Zeldovich 1972), which as been confirmed by the *Planck* satellite observing $n_{\text{s}} = 0.965 \pm 0.004$ (Planck Collaboration et al. 2018c). This is a consequence of the fact that at the time of inflation there are no privileged scales for the fluctuations. The value of the amplitude, however, is not predicted by theory but can only be constrained by observations. From the CMB a primordial amplitude $A_{\text{s}} = (2.10 \pm 0.03) \cdot 10^{-9}$ is estimated at $k = 0.05\,\text{Mpc}^{-1}$ (Planck Collaboration et al. 2018b).

The growth of perturbations is strictly related to the horizon scale (Eq. 1.11) at a given time: outside the horizon the fluctuations always grow, as the only force at work is gravity, while inside the horizon the growth is influenced by micro-physics effects, such as radiation pressure before the decoupling. In particular, the CDM perturbations that enter the horizon before the equivalence z_{eq} undergo a *stagnation effect* (Meszaros 1974) and do not grow until $z < z_{\text{eq}}$. This is due to the fact that the expansion timescale of the Universe, given by $\tau_{\text{exp}} \propto \rho_{\text{tot}}^{-1/2}$ with $\rho_{\text{tot}} = \rho_\gamma$ in the radiation era, is much smaller than the CDM free-fall (or collapse) timescale, given by $\tau_{\text{ff}} \propto \rho_{\text{c}}^{-1/2}$ where ρ_{c} is the CDM density (see Table 1.1). After the equivalence, $\rho_{\text{tot}} \approx \rho_{\text{m}}$ and the CDM perturbations can grow again. Thus, it is possible to describe the power spectrum at the equivalence as

$$P(k, z_{\text{eq}}) = \begin{cases} P_{\text{prim}}(k)\, k^{-4}, & \text{for } k \gg k_{\text{eq}} \\ P_{\text{prim}}(k), & \text{for } k \ll k_{\text{eq}} \end{cases} \tag{1.53}$$

where $k_{\text{eq}} = 0.0105 \pm 0.0001\,\text{Mpc}^{-1}$ (Planck Collaboration et al. 2018a) in the ΛCDM model. After the time of equivalence, the micro-physics effects are negligible and the power spectrum grows in a self-similar way in the linear regime.

Substituting Eq. (1.52) into Eq. (1.51), it can be shown that the smaller the scale, the higher the variance:

$$\sigma_M^2 \propto \int k^{n_{\text{s}}+2} \, \mathrm{d}k \propto k^{n_{\text{s}}+3} \propto R^{-(n_{\text{s}}+3)} \tag{1.54}$$

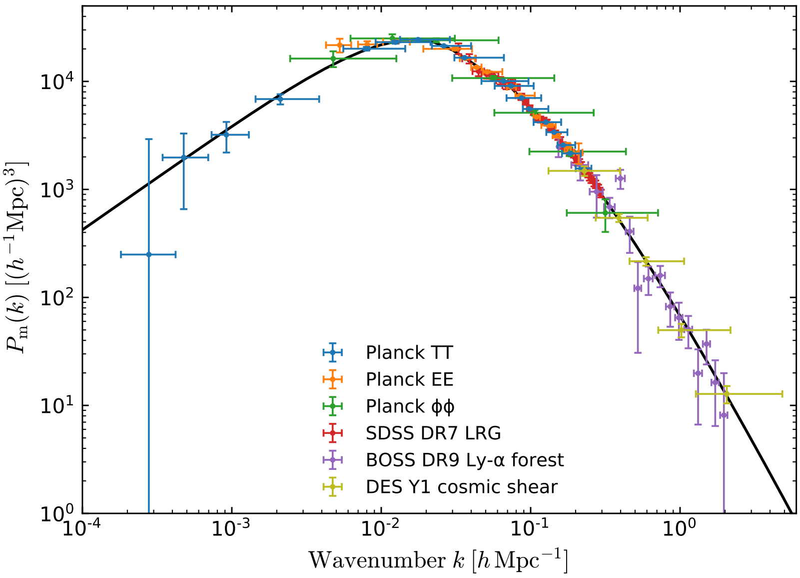

Figure 1.4 The linear theory matter power spectrum at $z = 0$, indicated as $P_{\rm m}$, obtained from different cosmological probes. The black line is the model from the ΛCDM model, that fits very well with such different data. From Planck Collaboration et al. (2018a).

This means that small scales enter the non-linear regime earlier than large ones and begin to grow faster respect to the linear regime.[3]

Figure 1.4 shows the linear theory power spectrum at present day. At $k \approx 0.01\,h\,{\rm Mpc}^{-1}$ we note the peak corresponding to the horizon scale at the time of equivalence. Thus, the peak position is a function of $\Omega_{0,{\rm m}}$, which can be directly measured from the observed matter power spectrum. Finally, note that in Figure 1.4 the error bars increase in magnitude toward large scales. This is due to the *cosmic variance*: at small k-modes correspond large volumes, so the considered realisations are few (the maximum volume is the Universe one) and the average over these can not reduces the error. On the other hand, at smaller scales we can sample the Universe with several small volumes, and the average over these reduces the final error.

---

[3] The perturbations at the time of equivalence are still linear, because at the baryon-radiation decoupling the CMB fluctuations are $\delta_\gamma \approx 10^{-5}$ (see §1.2.3) and $z_{\rm eq} > z_{\rm dec}$.

Chapter 2

Cosmology with the 21 cm line

In this chapter, we will review the theory of the 21 cm line in a cosmological context, in particular during the epoch of reionization (EoR). A detailed discussion can be find in Furlanetto et al. (2006).

2.1 From the Dark Ages to the Epoch of Reionization

The evolution of the Universe after recombination can be marked with three distinct phases.

The first is called *Dark Ages*, which begins right after recombination and ends at $z \approx 30$. As shown in §1.3, DM halos begin to accrete baryons at $z \approx z_{\rm dec}$ and density perturbations grow, becoming non-linear at $z \approx 30$. By then, baryon overdensities are expected to collapse into the first luminous objects (e.g., Barkana and Loeb 2001; O'Leary and McQuinn 2012). In this respect, the physics of the Dark Ages is fairly simple as it is driven by gravity and expansion of the Universe only.

The formation of the first stars at $z = 20 - 30$ marks the beginning of the *Cosmic Dawn*. We will see in the next sections that the formation of the first structures leaves a footprint on the intergalactic medium (IGM): initially galaxies heat the IGM and, as their star formation progresses, they will ionize the IGM, beginning the *Epoch of Reionization* (EoR). Before describing the potential of the 21 cm line as cosmic probe, we will review the observational evidences of cosmic reionization in the next section.

2.1.1 Observational probes of the Epoch of Reionization

Cosmic reionization is supported by several observational evidences.

- **Gunn-Peterson (GP) effect.** It is related to the absorption against high-redshift quasars. Gunn and Peterson (1965) first pointed out that, given the large Lyman-alpha (Lyα) cross section, even a small HI fraction $x_{\rm HI}$ (i.e., $x_{\rm HI} > 10^{-4}$) in the IGM would completely absorb the UV radiation of a background source. This can be seen defining the GP optical depth (e.g., Becker et al. 2001):

$$\tau_{\rm GP} = 1.8 \cdot 10^5 \, x_{\rm HI} \, h^{-1} \Omega_{0,\rm m}^{-1/2} \left(\frac{\Omega_{0,\rm b} h^2}{0.02} \right) \left(\frac{1+z}{7} \right)^{3/2}, \tag{2.1}$$

  where $\Omega_{0,\rm m}$ and $\Omega_{0,\rm b}$ are the matter and baryon density parameters (see Table 1.1). The GP effect was first observed by Schmidt (1965) on quasars at $z \approx 2$. As observations become capable to reach higher redshifts, Becker et al. (2001) observed the absorption against three quasars at $z = 5.82$, 5.99 and 6.28. They found no detection of emission immediately blueward of the Lyα line (rest-frame wavelength $\lambda_\alpha = 1215.67\,\text{Å}$), a two orders of magnitude drop compared with the observation of $z = 5.3$ quasars, implying an optical depth of the GP effect $\tau_{\rm GP} > 20$. This was interpreted as a clear detection of a complete GP trough and the fact the Universe is approaching reionization at $z \approx 6$. Evidence of $z \approx 6$ reionization was further confirmed by the analysis of a sample of $5.7 < z < 6.5$ quasars by Fan et al. (2006). Finding increasingly higher redshift quasars is, however, challenging and fewer are known at $z > 6$. The current record holder is ULAS J1120+0641 at $z = 7.08$ (Mortlock 2016). Thus, the actual scenario is that the reionization ends at $z \approx 6$, where $\tau_{\rm GP} > 0.038$ (Venemans et al. 2013). The problem of observations based on the GP effect is that they can probe only the tail of the reionization, as if the HI fraction of the IGM is higher than $\sim 10\%$ there is no transmission. Thus, it is insensitive to the reionization history. To do that, other techniques are needed, such as dark gaps (Croft 1998; Songaila and Cowie 2002) or dark pixels (McGreer et al. 2011; McGreer et al. 2015) methods.

- **CMB optical depth.** In the presence of free electrons, CMB photons are Thomson scattered, with an optical depth $\tau_{\rm th}$ defined as

  $$\tau_{\rm th} = \int n_e \sigma_{\rm th} \,{\rm d}l, \tag{2.2}$$

  where n_e is the electron density, such that $x_i = n_e/n_{\rm HI}$ is the ionization fraction, $\sigma_{\rm th}$ is the Thomson scattering cross-section and the integral is over the line of sight. We therefore expect that, after recombination, CMB photons are further scattered during reionization. In particular, Thomson scattering produces an additional peak in the CMB polarization power spectrum on very large scales, known as *reionization bump* (e.g., Rees 1968). The magnitude and position of that bump depend upon the optical depth and the redshift of reionization respectively. The latest measurements from the Planck experiment constrained the optical depth to be $\tau_{\rm th} = 0.058 \pm 0.012$ (Planck Collaboration et al. 2016b; 2016c). Measurements of the evolution of the HI neutral fraction can be derived from the CMB optical depth by assuming a model for the evolution of the ionization fraction (Kogut et al. 2003; Hinshaw et al. 2013). A standard assumption is to use a tanh model (Lewis 2008):

  $$x_i(z) = \frac{f}{2}\left[1 + \tanh\left(\frac{y - y_{\rm re}}{\Delta y}\right)\right], \tag{2.3}$$

  where $f = 1 + n_{\rm He}/n_{\rm HI}$, with $n_{\rm He}$ the number density of helium atoms, $y = (1+z)^{3/2}$, $\Delta y = 3(1+z)^{1/2}\Delta z/2$ and $z_{\rm re}$ is the mid-point redshift of the reionization, i.e. the redshift at which $x_{\rm HI} = 0.5$. Based on the Planck data alone, Planck Collaboration et al. (2016c) found $z_{\rm re} = 8.5 \pm 0.9$. Assuming that the reionization end was constrained by observations of the GP effect in high-redshift quasars to be $z = 6$, this implies that reionization began at $z \approx 11$. As the GP effect, the CMB optical depth is not sensitive to the reionization history, because it is an integrated quantity.

- **Kinetic Sunyaev-Zeldovich (kSZ) effect.** Theoretically developed by Sunyaev and Zeldovich (1980), it is due to the bulk velocity of free electrons relative to the CMB photons, which introduces a Doppler shift to the scattered photons (Reichardt 2016). The scales at work are small, comparable to the ionized bubbles around the ionizing sources, so the effect is observed at $\ell \approx 3000$. Planck Collaboration et al. (2016c) is insensitive to these high ℓ, so their estimates are obtained combining measurements from other experiments, finding $z_{\rm re} = 7.8 \pm 0.9$. Finally, they combine this result with that obtained by the CMB optical depth, in order to estimate a reionization mid-point $z_{\rm re} = 8.2 \pm 1.1$. All the errors are given by the cosmic variance at large-scales and by foregrounds and systematic effects at small-scales (Planck Collaboration et al. 2016c). These values suggest that there is probably no reionization at $z > 15$, according to the results obtained from high-redshift IGM simulations (e.g., Mesinger et al. 2011).

- **Demographics of Lyα emitters**. Lyα emitters (LAE) are star forming galaxies at high-redshift (McQuinn et al. 2007). Similar to the GP effect, the neutral IGM absorbs the Lyα emission, leading to a rapid decrease in the LAE luminosity function beyond $z \approx 6$ (Kashikawa et al. 2006; Ouchi et al. 2010; Konno et al. 2014). Indeed, the Lyα line can be observed only if the surrounding environment of an emitting galaxy is ionized and large enough to redshift the line out of resonance before being absorbed by HI. Thus, the decline in the fraction of LAE observed at high-redshift is attributed to the absorption of neutral IGM, which has a neutral fraction $x_{\mathrm{HI}} \approx 0.70$ at $z \approx 7$ (Tilvi et al. 2014; Faisst et al. 2014). This method, similarly to that related to the GP effect and to the CMB optical depth, constrains the neutral fraction but does not provide more information about the reionization history. In order to do that, in particular about the redshift evolution of the IGM temperature and the distribution of the ionized bubbles, the 21 cm line is potentially the best probe, as we will see in next sections.

2.2 The 21 cm hydrogen line

The 21 cm line is emitted from the hyperfine spin-flip transition of neutral hydrogen, which occurs when the electron and proton spins are in the parallel configuration – rather than the anti-parallel configuration in the fundamental state. The energy associated to the hyperfine transition $1\,S_{1/2}$ is $5.9 \cdot 10^{-6}$ eV, much smaller than the 13.6 eV corresponding to the fundamental level. The two hyperfine levels are $1\,{}_0S_{1/2}$ and $1\,{}_1S_{1/2}$ according to the Hund notation ${}_FL_J$, where L and J are the orbital and angular momentum of the electron, and F is the total angular momenta of the atom, which could be 1 if electron and proton spins are parallel or 0 if they are antiparallel.[1] In this section, we summarize the physics of the 21 cm line in order to better understand its high-redshift applications, following the detailed review of Furlanetto et al. (2006).

2.2.1 The 21 cm brightness temperature

The 21 cm line emitted by a hydrogen cloud at high-redshift can be described by the radiative transfer equation, assuming equilibrium along the line of sight through the cloud. The specific intensity I_ν of the 21 cm line can be written using the Rayleigh-Jeans approximation:

$$T_b(\nu) \approx \frac{c^2}{2k_{\mathrm{B}}\nu^2}\, I_\nu, \tag{2.4}$$

where $T_b(\nu)$ is the brightness temperature – i.e., the temperature that a black-body should have to emit the observed radiation –, c is the speed of light and k_{B} is the Boltzmann's constant. Eq. (2.4) describes the brightness observed from Earth at the frequency $\nu = \nu_0(1+z)^{-1}$, where ν_0 is the rest frequency, that is $\nu_0 = 1420$ MHz for the 21 cm line. Thus, the brightness measured in the cloud comoving frame at redshift z is $T'_b(\nu_0) = T_b(\nu)(1+z)$, similarly to Eq. (1.31) for the CMB.

Using the brightness temperature, the radiative transfer equation can be written as

$$T'_b(\nu) = T_{\mathrm{s}}(1 - e^{-\tau_\nu}) + T'_{\mathrm{r}}(\nu)\, e^{-\tau_\nu}, \tag{2.5}$$

where T_{s} is the cloud excitation or *spin temperature*, τ_ν is the optical depth and T'_{r} is the brightness temperature of the background radiation. In the cosmological context, the background is represented by the CMB temperature, i.e. $T'_{\mathrm{r}} = T_\gamma$. The first term on the right-hand side of Eq. (2.5) describes the radiation emitted from the cloud and absorbed by the cloud itself, whereas the second term describes the absorption of the background radiation when it passes through the cloud.

---

[1] F is the sum of the electron and the proton/nucleus spins, which take values $\pm 1/2$ such that $F = 0$ or 1.

The spin temperature describes the population ratio between the hyperfine and the fundamental energy levels in a cloud in thermodynamic equilibrium:

$$\frac{n_1}{n_0} = \frac{g_1}{g_0} \exp\left(-\frac{E_{10}}{k_\mathrm{B} T_\mathrm{s}}\right), \tag{2.6}$$

where n_1 and n_0 are the number of atoms in the hyperfine and fundamental states, respectively, g_1 and g_0 their statistical weights, and $E_{10} = 5.9 \cdot 10^{-6}\,\mathrm{eV}$ is the energy difference between the two levels that correspond to a temperature $T_\star$:

$$T_\star \equiv \frac{E_{10}}{k_\mathrm{B}} = 0.0681\,\mathrm{K}. \tag{2.7}$$

As the lower state of the hyperfine structure is a singlet and the upper is a triplet, the statistical weights are $g_0 = 1$ and $g_1 = 3$ respectively, and Eq. (2.6) becomes

$$\frac{n_1}{n_0} = 3\,e^{-T_\star/T_\mathrm{s}}. \tag{2.8}$$

In essentially all the cosmological cases $T_\mathrm{s} \gg T_\star$, implying that only $1/4$ of the total number of atoms is in the hyperfine ground state, while the remaining $3/4$ are in the excited state. The spin temperature is therefore a convenient quantity to describe the relative population of the singlet and the triplet in a population of HI atoms (Field 1958).

The observed *brightness contrast* $\delta T_b \equiv T_b - T_\gamma$ between the radiation emitted by the HI cloud and the CMB is (e.g., Ciardi and Madau 2003)

$$\delta T_b(z) = \frac{T_b'(\nu) - T_\gamma(z)}{1+z} = \frac{T_\mathrm{s} - T_\gamma(z)}{1+z}\left(1 - e^{\tau_{\nu_0}}\right) \approx \frac{T_\mathrm{s} - T_\gamma(z)}{1+z}\,\tau_{\nu_0}, \tag{2.9}$$

where we have substituted Eq. (2.5) in the second step, and the last approximation follows from the fact that the 21 cm optical depth is small. Using the expression for τ_{ν_0} derived by Madau et al. (1997), the 21 cm brightness temperature becomes (Mesinger et al. 2015)

$$\delta T_b(z) = 27 x_\mathrm{HI}(1+\delta)\left[\frac{1+z}{10}\frac{0.15}{\Omega_{0,\mathrm{m}}h^2}\right]^{1/2}\left[\frac{\Omega_{0,\mathrm{b}}h^2}{0.023}\right]\left[\frac{1-Y_\mathrm{p}}{0.75}\right]\left[1 - \frac{T_\gamma}{T_\mathrm{s}}\right]\left[\frac{H(z)/(1+z)}{\mathrm{d}v_\parallel/\mathrm{d}r_\parallel}\right]\mathrm{mK}, \tag{2.10}$$

where x_HI is the HI neutral fraction, δ is the density contrast (see §1.3.1), $H(z)$ is the Hubble parameter, Y_p is the helium mass fraction, and $\mathrm{d}v_\parallel/\mathrm{d}r_\parallel$ is the gradient of the proper velocity along the line of sight (see Kaiser 1987). The last term in brackets takes into account the redshift-space distortion effect, which is generally a second-order effect.

The evolution of the brightness temperature is essentially determined by x_HI, δ and T_s, all quantities that vary spatially. In particular, Eq. (2.10) formalizes the concept that the 21 cm emission is always observed against the CMB background: δT_b is observed in absorption (i.e., is negative) if $T_\mathrm{s} < T_\gamma$, and in emission (i.e., is positive) if $T_\mathrm{s} > T_\gamma$. We describe below which processes set the spin temperature.

2.2.2 The spin temperature

As we have seen in the previous section, the 21 cm line is observable if the spin temperature is different than the CMB temperature, in other words if the spin temperature is driven towards (i.e., coupled to) the only other physical temperature at play, the gas temperature T_k. There three such competing mechanisms:

- absorption of CMB photons sets the spin temperature to the CMB temperature ($T_\mathrm{s} \to T_\gamma$);

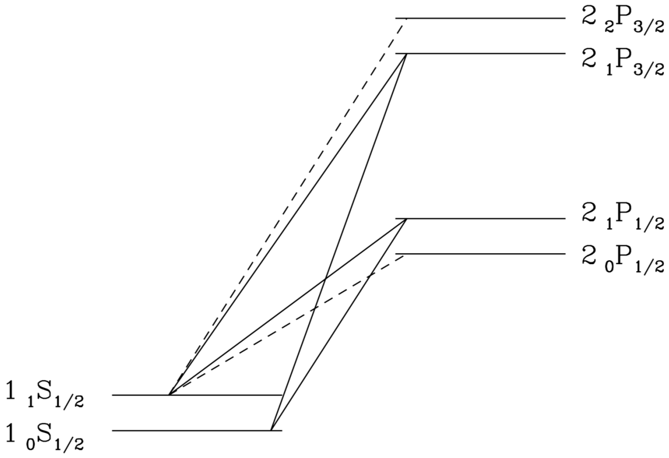

Figure 2.1 Hyperfine splitting of the $1\,S$ and $2\,P$ levels of the neutral hydrogen atom, according to the Hund notation. The solid lines represent transitions relevant for the Wouthuysen-Field effect, since they mix the population of the ground state hyperfine levels, while the dashed lines represent transitions that do not lead to a mixing of populations. From Pritchard and Furlanetto (2006).

- collisions with other HI atoms set the spin temperature to the gas temperature ($T_\mathrm{s} \to T_\mathrm{k}$). Collisions are the main coupling mechanism at high-redshift ($z > 30$), when the gas density is high and no other astrophysical sources exist (Furlanetto 2016);

- resonant scattering of UV photons (Wouthuysen-Field effect; Wouthuysen 1952; Field 1959) sets the spin temperature to the CMB temperature ($T_\mathrm{s} \to T_\gamma$). Figure 2.1 visually shows the Wouthuysen-Field (WF) effect: when a Lyα photon is absorbed by a HI atom in the ground state $1\,S$, the electron can jump to either of the $2\,P$ states, following the quantum selection rules. At this point, the electron can decay from the $2P$ state to the fundamental triplet rather than the singlet, allowing for a 21 cm photon to be emitted. In other words, the WF effect allows the hyperfine state to be populated in the presence of a UV background radiation. In most models, the first stars form at $z \approx 30$ and emit a background of UV photons. From that moment onward, the WF effect is the main coupling mechanism. As the IGM is extremely optically thick at high-redshift, the large number of scattering produces a black-body shape in the Lyα spectrum around the resonance frequency, driving $T_\mathrm{s} \to T_\mathrm{k}$.

Mathematically, the spin temperature can be described as a weighted mean of these three processes and here we present a pedagogical derivation of this result based on the seminal Field (1958) paper.

Collisions and UV scattering are described by the excitation (de-excitation) rates per atom C_{01} (C_{10}) and P_{01} (P_{10}), respectively. Since timescales of the above processes are much shorter than the Universe expansion time, *statistical thermal equilibrium* can be used to determine the spin temperature (e.g., Furlanetto et al. 2006):

$$n_1(C_{10} + P_{10} + A_{10} + B_{10}I_\gamma) = n_0(C_{01} + P_{01} + B_{01}I_\gamma), \tag{2.11}$$

where A_{10}, B_{01} and B_{10} are the Einstein coefficients of spontaneous emission, absorption and stimulated emission of the 21 cm transition, respectively. It can be shown that B_{01} and B_{10} are functions of A_{10} (Rybicki and Lightman 1979), whose value is $\sim 2.85 \cdot 10^{-15}\,\mathrm{s}^{-1}$:

$$B_{01} = 3B_{10} = \frac{3c^2}{2h\nu^3}\,A_{10}, \tag{2.12}$$

where the first equality follows from the Einstein relation $g_0 B_{01} = g_1 B_{10}$, with $g_0 = 1$ and $g_1 = 3$. Using Eq. (2.4) and (2.7), we can write

$$B_{01} I_\gamma = \frac{3\lambda^2 I_\gamma}{2h\nu_0} A_{10} = 3A_{10}\,\frac{T_\gamma}{T_\star}. \tag{2.13}$$

Furthermore, the ratios between the transition rates due to collisions and photon scattering are respectively (Field 1958)

$$\frac{C_{01}}{C_{10}} \approx 3\left(1 - \frac{T_\star}{T_\mathrm{k}}\right) \quad ; \quad \frac{P_{01}}{P_{10}} \approx 3\left(1 - \frac{T_\star}{T_\alpha}\right), \tag{2.14}$$

where T_α is the color temperature of the UV radiation field. Thus, replacing Eq. (2.13) and Eq. (2.14) in Eq. (2.11), we have

$$\begin{aligned} \frac{n_1}{n_0} = 3\left(1 - \frac{T_\star}{T_\mathrm{s}}\right) &= \frac{C_{01} + P_{01} + B_{01} I_\gamma}{C_{10} + P_{10} + A_{10} + B_{10} I_\gamma} \\ &= 3\,\frac{\left(1 - \frac{T_\star}{T_\mathrm{k}}\right) C_{10} + \left(1 - \frac{T_\star}{T_\alpha}\right) P_{10} + \frac{T_\gamma}{T_\star} A_{10}}{C_{10} + P_{10} + \left(1 + \frac{T_\gamma}{T_\star}\right) A_{10}}. \end{aligned} \tag{2.15}$$

Isolating T_s^{-1} and dividing numerator and denominator by $A_{10} T_\gamma$, we finally obtain

$$T_\mathrm{s}^{-1} = \frac{\frac{C_{10}}{A_{10}} \frac{T_\star}{T_\gamma} T_\mathrm{k}^{-1} + \frac{P_{10}}{A_{10}} \frac{T_\star}{T_\gamma} T_\alpha^{-1} + T_\gamma^{-1}}{\frac{C_{10}}{A_{10}} \frac{T_\star}{T_\gamma} + \frac{P_{10}}{A_{10}} \frac{T_\star}{T_\gamma} + \left(1 + \frac{T_\star}{T_\gamma}\right)} = \frac{x_c T_\mathrm{k}^{-1} + x_\alpha T_\alpha^{-1} + T_\gamma^{-1}}{x_c + x_\alpha + 1}, \tag{2.16}$$

where in the last step we have assumed $T_\gamma \gg T_\star$ at any $z > 0$, and we have introduced the coupling coefficients for collisions and photon scattering, x_c and x_α respectively. Thus, $T_\mathrm{s} \to T_\gamma$ when there are only CMB photons and no other astrophysical process. When the first luminous sources are formed, x_α begins to couple T_s to T_α which is, in turn, coupled to the gas temperature due to the high optical depth of the IGM.

Figure 2.2 shows the evolution of T_s, T_k and T_γ for a fiducial model (Mesinger et al. 2011), averaged over the cosmological volume. Right after thermal decoupling, the gas temperature starts to cool faster than the CMB, and collisions couple the spin temperature to the gas temperature. Around $z \approx 35$, the Universe has expanded sufficiently that collisions are no longer efficient to couple the spin temperature to the gas temperature (i.e., $x_c \to 0$) and the spin temperature is again driven towards the CMB temperature. Around $z \approx 30$, however, the WF effect starts again to couple T_s to T_k, due to the UV radiation background emitted by the first stars. The coupling is complete in a few tens of million of years ($z \approx 25$) and, from that moment onward, T_s remains coupled to T_k.

The last transition of the thermal history of the IGM occurs later ($z \approx 20$ in the model shown here): the radiation emitted by the first sources eventually heats the IGM above the CMB, until $T_\mathrm{k} \gg T_\gamma$ at $z \approx 15$. This transition is often referred to as the *spin temperature saturation*, as the evolution of the 21 cm brightness essentially no longer depends upon T_s (see Eq. 2.10) from that moment onward.

2.3 The 21 cm Global Signal

After the thermal history of the IGM, the 21 cm signal is determined by the evolution of its ionization state. Before the formation of astrophysical sources, the IGM is fully neutral and its evolution is essentially driven by the evolution of the spin temperature. The average HI neutral fraction begins to evolve when the first galaxies emit sufficient UV radiation to begin

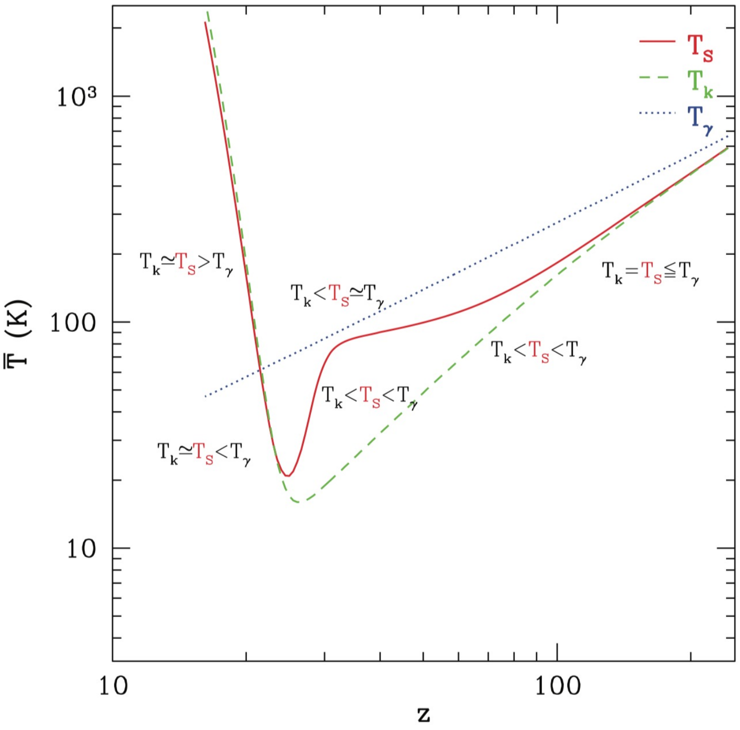

Figure 2.2 Redshift evolution of volume averaged temperatures $\overline{T}_{\rm s}$ (red solid line), $\overline{T}_{\rm k}$ (green dashed line) and $\overline{T}_\gamma$ (blue dotetd line) in a fiducial model. From Mesinger et al. (2011).

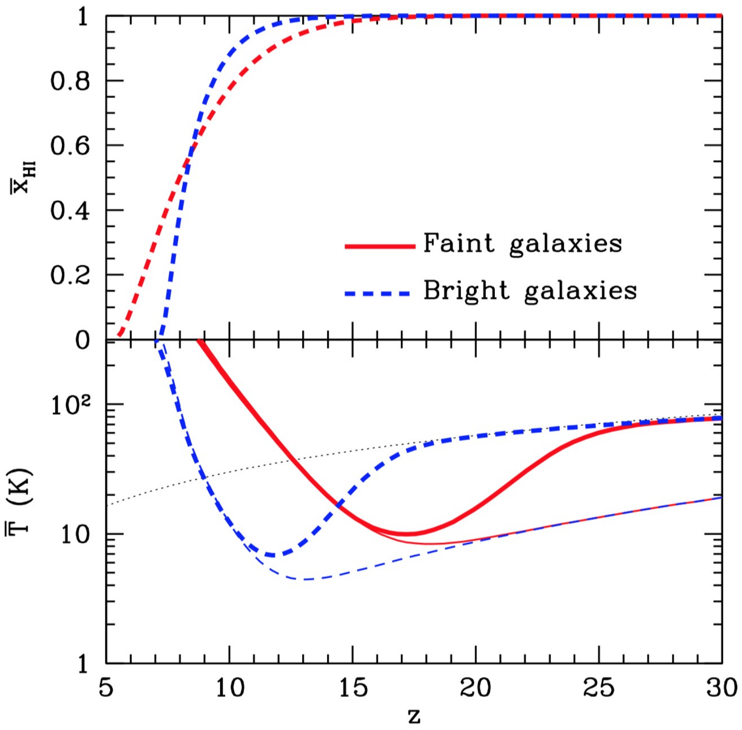

Figure 2.3 Redshift evolution of the volume averaged HI fraction $\overline{x}_{\rm HI}$ (top panel), together with the average mean temperatures (bottom panel): $\overline{T}_{\rm s}$ (thick line), $\overline{T}_{\rm k}$ (thin line) and $\overline{T}_\gamma$ (black dotted line). Faint Galaxies (red) and a Bright Galaxies scenario (blue) models are shown – see text for more details. From Mesinger et al. (2016).

to ionize the surrounding IGM. The evolution of the HI neutral fraction depends upon the formation and evolution of ionizing sources. Figure 2.3 displays the evolution of the volume averaged quantities for two models where the reionization is driven by either faint or bright galaxies (Mesinger et al. 2016). The difference between the two scenarios resides in the star formation efficiency: in §1.3 we have seen that stars and galaxies form inside DM halos, but in order to collapse into stars, the gas has to cool down to ~ 100 K. If the gas is heated or expelled from the DM halo, for instance due to supernovae (SNe) explosions, the star formation efficiency decreases (e.g., Barkana and Loeb 2001; Springel and Hernquist 2003). Suppression of star formation occurs more easily in low-mass DM halos – which are more numerous than high-mass halos. The Mesinger et al. (2016) Bright Galaxies model assumes an extremely efficient SNe feedback, which suppresses star formation in small halos, leaving only the rare ones with masses above $10^{10}\,\mathrm{M}_\odot$ to drive reionization. On the other hand, in the Faint Galaxies scenario the SNe feedback is inefficient and reionization is driven by the abundant halos with $\sim 10^9\,\mathrm{M}_\odot$ mass. As we have seen in §1.3.1, in a CDM-dominated Universe, small structures form first, thus in the Bright Galaxies scenario reionization starts later than in the Faint Galaxies one, but it is faster because the ionizing UV background is produced much more efficiently. The mid point of reionization is the same by construction in both scenarios.

In both models, the IGM temperature evolves with redshift in a similar fashion, as described in §1.2.2, although shifted at lower redshifts for the Bright Galaxies model. Specifically, in the Faint Galaxies model the onset of reionization occurs when T_s is coupled to T_k and higher than T_γ, whereas in the Bright Galaxies model it occurs when T_s is colder than T_γ. As a consequence, in the Bright Galaxy model, the gas is still colder than the CMB at the mid-point of reionization and becomes heated well above the CMB only when reionization is essentially complete.

The Bright Galaxies model is a flavour or *cold reionization* scenario, i.e. a scenario where the gas temperature is never heated above the CMB temperature before reionization is complete. Fialkov et al. (2014) suggested that if the spectrum of the X-ray emission produced in the first galaxies (for instance, form X-ray binaries) is hard, the IGM heating is less efficient and is, therefore, delayed, as hard X-ray photons have a longer mean free path compared to soft X-ray photons.

In the next section we well discuss the details of the evolution of the global signal.

2.3.1 Evolution of the Global Signal

The sky-averaged 21 cm brightness temperature is known as the *global signal*:

$$\overline{\delta T}_b(z) = \frac{\int_\Omega \delta T_b(\Omega', z)\,\mathrm{d}\Omega'}{\int \mathrm{d}\Omega'}, \tag{2.17}$$

where Ω is the sky solid angle. Similarly, we can define the globally-averaged temperature and HI fraction, indicated with overbars. A fiducial model of $\overline{\delta T}_b(z)$ is shown in Figure 2.4. As we have seen in §2.2.2, the evolution of the signal is driven by the coupling between the spin temperature and the CMB or the gas temperature through the different cosmic epochs (see also Figure 2.2). Following the thermal history outlined in §2.1, there are a few landmarks in the evolution of the global signal.

- $\mathbf{z > 200}$. Compton scattering between CMB photons and free electrons keeps the gas temperature coupled to the CMB temperature, thus we do not expect a 21 cm signal since $T_\mathrm{s} = T_\gamma$.

- $\mathbf{200 > z > 80}$. The average ionized fraction $\overline{x}_i = 1 - \overline{x}_\mathrm{HI}$ drops to $\sim 10^{-4}$ (Furlanetto et al. 2006) and Compton scattering is no longer efficient to couple T_k and T_γ. The Universe enters in the Dark Ages and the gas begins to adiabatically cool faster than

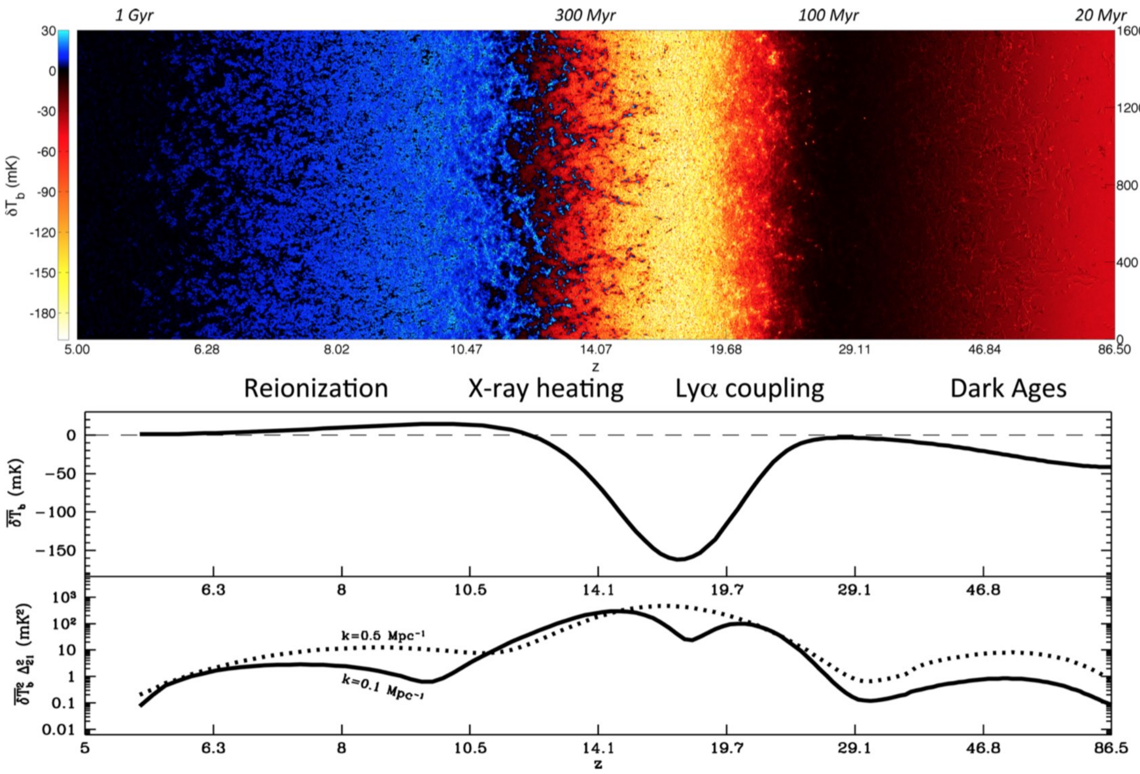

Figure 2.4 Evolution of the 21 cm signal. The top panel is a simulation slice representing the redshift evolution of the brightness temperature fluctuations δT_b. The middle panel shows the fiducial model of the sky-averaged brightness (i.e., global signal, solid line). The most relevant cosmic epochs are highlighted. The bottom panel represents the evolution of the dimensionless power spectrum amplitude (Eq. 2.22) at $k = 0.1\,\mathrm{Mpc}^{-1}$ (solid line) and $k = 0.5\,\mathrm{Mpc}^{-1}$ (dotted line). From Mesinger et al. (2016).

the CMB. In particular, from Eq. (1.32), we can normalize the gas temperature to the redshift $z_{\rm dec}$ of the baryon-radiation decoupling:

$$T_{\rm k}(z) = T_{\rm k}(z_{\rm dec})\,\frac{(1+z)^2}{(1+z_{\rm dec})^2} = T_{\gamma,0}\,\frac{(1+z)^2}{1+z_{\rm dec}}, \tag{2.18}$$

where in the last step we have used Eq. (1.31) and the fact that $T_\gamma(z_{\rm dec}) \equiv T_{\rm k}(z_{\rm dec})$. Assuming $z_{\rm dec} \approx 200$ (Furlanetto et al. 2006) and $T_{\gamma,0} \approx 2.73\,\mathrm{K}$, we can write Eq. (2.18) as

$$T_{\rm k}(z) \approx 0.014(1+z)^2\,\mathrm{K}. \tag{2.19}$$

At these redshifts, the density of the IGM is high enough that collisional coupling keeps $T_{\rm s} = T_{\rm k}$, thus, from $z_{\rm dec}$ the signal appears in absorption.

- **80 > z > 30**. Collisional coupling is no longer effective as a result of the expansion of the Universe, so $T_{\rm s} \to T_\gamma$. At $z \approx 30$ the spin temperature equals the CMB temperature and the 21 cm signal disappears.

- **30 > z > 20 (Cosmic Dawn)**. In most structure formation models, first stars form here, and begin to emit a Lyα radiation background that couples the spin temperature to the gas temperature through the WF effect. Using Eq. (2.19), we know that the gas has $T_{\rm k} \approx 6\,\mathrm{K}$ at $z \approx 20$, while the CMB has $T_\gamma \approx 60\,\mathrm{K}$, then $T_{\rm k} \ll T_\gamma$ and the absorption in the 21 cm signal can be very strong. Indeed, the Cosmic Dawn signature is the more prominent feature in $\overline{\delta T}_b$ and hence the main target of global 21 cm experiments, as we will see in §2.5.

- **$20 > z > 12$**. As star formation continues, more massive stars die as Type II supernovae (SNII), leaving black holes that can form binary systems with other stars and emit X-ray radiation through accretion (Pritchard and Furlanetto 2007). X-ray photons heat large volumes of the IGM, eventually leading the gas temperature above the CMB temperature. From this moment on, the 21 cm signal appears in emission.

- **$12 > z > 6$ (EoR)**. At $z \approx 12$ the 21 cm signal saturates, because $T_{\mathrm{s}} \gg T_{\gamma}$. In this period first galaxies form and, when enough ionizing UV radiation escapes from them, the IGM begins to be ionized (e.g., Ciardi and Ferrara 2005). At $z \approx 6$ the gas is essentially fully ionized, then $\overline{x}_{\mathrm{HI}} \approx 0$ and from Eq. (2.10) we no longer expect any signal from the 21 cm.

2.4 Spatial fluctuations of the signal

We have seen that δT_b is a direction dependent quantity (Eq. 2.10) as δ, x_{HI} and T_{s}, i.e. evolve spatially with cosmic time. Though observations of the 21 cm line we can obtain *tomographic* images that encode the three dimensional evolution of the physics of the IGM and structure formation (Furlanetto 2016). Obtaining detailed 21 cm images is extremely demanding in terms of signal-to-noise ratio (SNR) and foreground subtraction (see §3). Therefore, spatial fluctuations are more easily characterized statistically, i.e. via their power spectrum. If we define the fractional brightness temperature contrast as

$$\delta_{21}(\mathbf{x}) \equiv \frac{\delta T_b(\mathbf{x}) - \overline{\delta T}_b}{\overline{\delta T}_b} \tag{2.20}$$

and indicate with $\tilde{\delta}_{21}(\mathbf{k})$ its Fourier transform, the 21 cm power spectrum is given by (Furlanetto et al. 2006)

$$\langle \tilde{\delta}_{21}(\mathbf{k})\, \tilde{\delta}_{21}(\mathbf{k}') \rangle \equiv (2\pi)^3 \delta_{\mathrm{D}}(\mathbf{k} + \mathbf{k}') P_{21}(k), \tag{2.21}$$

that it the same definition of Eq. (1.43), replacing the matter density perturbation δ with the 21 cm intensity fluctuations δ_{21}. The 21 cm power spectrum generally has dimensions of temperature squared times volume, i.e. $\mathrm{mK}^2\,(h^{-1}\,\mathrm{Mpc})^3$. The *dimensionless* power spectrum[2] $\Delta^2_{21}(k)$ is often used in literature:

$$\Delta^2_{21}(k) \equiv \frac{k^3}{2\pi^2} P_{21}(k), \tag{2.22}$$

which quantifies the space variance of δ_{21} and depends only on the wavenumber $k = |\mathbf{k}|$, and not on its orientation.

The bottom panel of Figure 2.4 shows the redshift evolution of two power spectrum modes from the Faint Galaxies scenario (see §2.3, Mesinger et al. 2016) at $k = 0.1\,\mathrm{Mpc}^{-1}$ and $k = 0.5\,\mathrm{Mpc}^{-1}$, corresponding to $\sim 60\,\mathrm{Mpc}$ and $\sim 10\,\mathrm{Mpc}$, respectively.

Simulations of 21 cm fluctuation together with their corresponding power spectra (Mesinger et al. 2011) are shown in Figure 2.5. Following Furlanetto (2016), we summarize the main phases similarly to what we did for the global signal.

- **$z \approx 30$**. The IGM is colder than CMB and the first luminous sources just begin to couple T_{s} to T_{k} through the WF effect. Thus, the fluctuations in the 21 cm signal are driven by the fluctuations in the Lyα radiation field, i.e. by T_{s}. In the top panel of Figure 2.5 most of the IGM is transparent to the CMB, while $\delta T_b < 0$ in small regions around the first sources.

---

[2] In the 21 cm cosmology it is a misnomer, since it has dimensions of temperature squared.

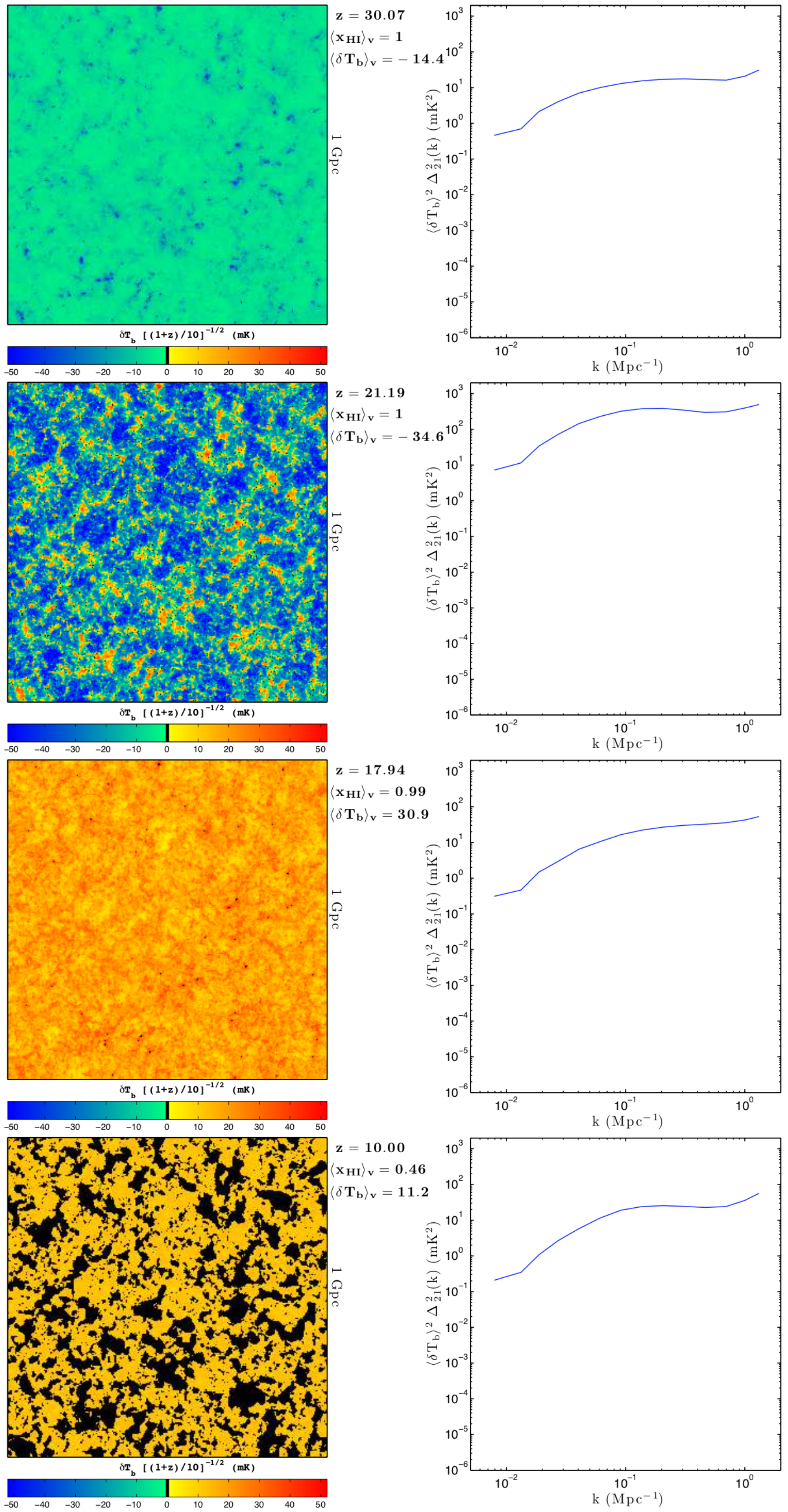

Figure 2.5 Left panels show slices from a semi-numerical simulation of the 21 cm signal (Mesinger et al. 2011) at $z = 30.1$, 21.2, 17.9 and 10.0 (top to bottom). Boxes are 1 Gpc wide and 3.3 Mpc deep. Black regions correspond to ionized regions, where $\delta_b = 0$ due to $x_{\mathrm{HI}} = 0$ (bottom left panel). Right panels illustrate the corresponding power spectra. The reported redshifts are the landmarks of the IGM evolution: from top to bottom we have the onset of the coupling between T_{s} and T_{k} by Lyα scattering, the beginning of X-ray heating, the 21 cm signal saturation due to $T_{\mathrm{s}} \gg T_{\gamma}$, and the mid-point of reionization. From Mesinger et al. (2011).

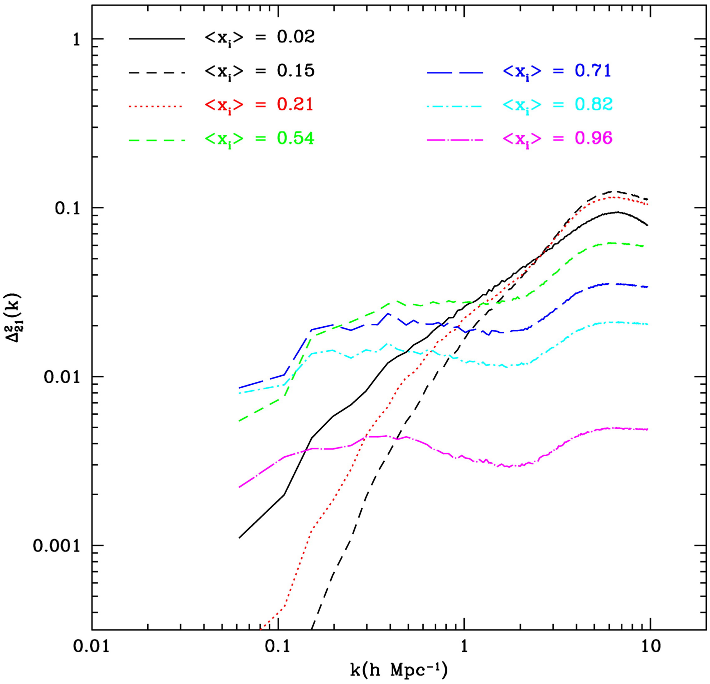

Figure 2.6 Redshift evolution of the dimensionless power spectrum as a function of wavenumber k and average ionization fraction $\langle x_i \rangle = \overline{x}_i$. In particular, the ionization fraction acts as a time coordinate, as $\overline{x}_i = 0.02, 0.15, 0.21, 0.54, 0.71, 0.82, 0.96$ correspond to $z = 11.46, 8.76, 8.34, 7.32, 7.03, 6.90, 6.77$. From Lidz et al. (2008).

- **z ≈ 20**. The appearance of the first X-ray sources starts to heat the surrounding gas, driving $T_{\rm k}$, and hence $T_{\rm s}$, above T_γ in discrete regions, which are seen in emission. The rest of the IGM is still cold and, therefore, appears in absorption against the CMB, as the Lyα radiation field had the time to couple $T_{\rm s}$ to $T_{\rm k}$ nearly everywhere. Fluctuations in the 21 cm signal are driven by the gas temperature, which generates a strong contrast between emitting and absorbing regions (second panel of Figure 2.5). The power spectrum amplitude is approximately one order of magnitude larger than at $z \approx 30$.

- **z ≈ 15**. The X-ray heating has saturated the 21 cm signal, with $T_{\rm s} \gg T_\gamma$ nearly everywhere in the IGM (third panel of Figure 2.5). Fluctuations are driven by the large-scale density field (Barkana and Loeb 2007), as variations in the gas temperature no longer contribute to δT_b. The amplitude of the power spectrum decreases by one order of magnitude.

- **z ≈ 10**. In this model, this is the mid-point of reionization. In the bottom panel of Figure 2.5 we see a net contrast between the ionized bubbles around galaxies, where $\delta T_b = 0$, and the fully neutral IGM, where the ionized photons have not yet penetrated. The ionized bubbles are a key feature of the EoR, since their properties depend largely on the nature of the ionizing sources (Zaldarriaga et al. 2004; Lidz et al. 2007). Thus, the 21 cm fluctuations in this epoch are driven by fluctuations in the neutral fraction $x_{\rm HI}$.

Figure 2.6 summarizes the power spectrum evolution across the EoR (albeit from a different model, Lidz et al. 2008) as a function of the average ionization fraction $\overline{x}_i$, which acts as time coordinate. When the IGM is still largely neutral, i.e. $\overline{x}_i = 0.02$, the power spectrum is still driven by the density fluctuations and peaks at small scales ($k > 1\,h\,{\rm Mpc}^{-1}$), which correspond to the densest regions where ionized regions form first. As reionization continues, there is a brief phase between $\overline{x}_i = 0.15$ and 0.21 in which the dimensionless power spectrum drops and steepens in slope at large-scales. This is due to the fact that we are plotting $\Delta^2_{21} \propto k^3 P_{21}(k)$ and in this period $P_{21}(k)$ is nearly constant at all scales: the overdense (small) regions initially contain more neutral hydrogen than underdense (large) regions, but their early ionization lowers the 21 cm signal power, while the rest of the IGM remains neutral and $x_{\rm HI}$ dominates the large-scale power spectrum (Furlanetto et al. 2004). After that phase, from $\overline{x}_i = 0.21$ to $\overline{x}_i = 0.54$, the power increases on large-scale as a consequence of the fast growth of the ionized bubbles (e.g., Zahn et al. 2007). In the range $0.1 < k < 1\,h\,\mathrm{Mpc}^{-1}$, the power spectrum reaches its maximum at the mid-point of reionization and, from this moment on, begins to flatten out. As $\overline{x}_i$ increases, the amplitude of Δ^2_{21} decreases to zero. In the standard scenario, this happens at $z \approx 6$, when the only neutral hydrogen in the Universe can be found within galaxies and the IGM is completely ionized.

2.4.1 Reionization sources: Galaxies vs AGN

Currently there is no general consensus on the sources driving the reionization. A long standing debate is related to the relative contribution to reionization from AGNs and galaxies. It is generally accepted that galaxies emit enough photon to reionize the Universe (Barkana and Loeb 2001; Robertson et al. 2010), as the AGN abundance decreases at $z > 3$ (e.g., Micheva et al. 2017). Willott et al. (2010) estimated that at $z = 6$ the ionizing background emitted by AGN can be two orders of magnitude lower than required for reionization. However, recent deep observations identified faint AGNs at $z > 4$ (Giallongo et al. 2015) and, if their high emissivity persists up to $z \approx 10$, Madau and Haardt (2015) suggested that faint AGNs can drive reionization, with a little contribution from star-forming galaxies. Both scenarios satisfy the optical depth measured from the CMB.

Observations of the 21 cm signal may be conclusive in discriminating between the two scenarios. If reionization is AGN-driven, the 21 cm power spectrum is one order of magnitude brighter on large-scales (Kulkarni et al. 2017), as AGNs form inside the most massive DM halos, i.e. the density and ionization fields are correlated. The evolution of the 21 cm power spectrum could also help disentangling the two scenarios as in an AGN dominated reionization, ionizing sources form later and reionization is delayed (Kulkarni et al. 2017). The most likely scenario is that ANG plays a role during reionization, which, however, remains driven by galaxies (Hassan et al. 2018).

2.5 Current status of observations

The number of instruments that attempt to detect the 21 cm cosmological signal has increased in the last ten years. In particular, interferometric arrays have been developed to study the spatial fluctuations, whereas the global signal is probed by single dipoles. In both cases, the target epochs are the EoR and the Cosmic Dawn.

With regard to fluctuations, the Giant Metrewave Radio Telescope[3] (GMRT; Kapahi and Ananthakrishnan 1995) was the first instrument to provide an upper limit of the power spectrum during the EoR (Paciga et al. 2011; Paciga et al. 2013). After that, the Precision Array for Probing the Epoch of Reionization[4] (PAPER; Parsons et al. 2010) was developed as an EoR power spectrum experiment (see §4), providing several upper limits during the cosmic reionization (Pober et al. 2013; Parsons et al. 2014; Ali et al. 2015; Jacobs et al. 2015; Kolopanis et al. 2019). The Murchison Widefield Array[5] (MWA; Tingay et al. 2013) has provided the best upper limits at $z = 7$ (Barry et al. 2019) and $z = 6.5$ (Trott et al. 2020),

---

[3] `http://www.gmrt.ncra.tifr.res.in/`

[4] `http://eor.berkeley.edu/`

[5] `http://www.mwatelescope.org/`

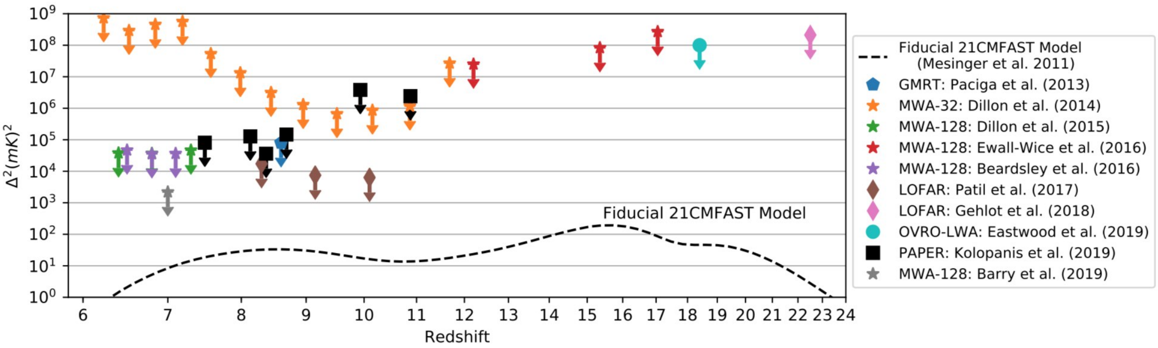

Figure 2.7 Current upper limits on EoR and Cosmic Dawn power spectrum measurements (Eq. 2.22). Values are from different k modes for each instrument, but still in the range $0.1 < k < 1\,h\,\mathrm{Mpc}^{-1}$ the theoretical dimensionless power spectrum is relatively spatially flat. The dashed line represents the simulated fiducial model from Mesinger et al. (2011). From Liu and Shaw (2019).

preceded by earlier results (Dillon et al. 2014; Dillon et al. 2015; Beardsley et al. 2016), including at the Cosmic Dawn (Ewall-Wice et al. 2016). In the last years, the LOw Frequency ARray[6] (LOFAR; van Haarlem et al. 2013) probed the Cosmic Dawn at the currently highest redshift ($20 < z < 25$) (Gehlot et al. 2019) and provided the best results on the EoR in the redshift range $z = 8 - 10.5$ (Patil et al. 2017; Mertens et al. 2020). At the lowest frequencies, the new Owens Valley Radio Observatory Long Wavelength Array[7] (OVRO-LWA) gave the first power spectrum limit at $z \approx 18$ (Eastwood et al. 2019), All these results are shown in Figure 2.7, where they are compared with the simulated model of Mesinger et al. (2011).

Global signal experiments provide an alternative path to the measurement of the 21 cm signal. The Shaped Antenna measurement of background RAdio Spectrum[8] (SARAS; Patra et al. 2013) constrained the EoR duration in the range $z = 6-10$, disfavoring rapid reionization models with $\mathrm{d}\left(\overline{\delta T_b}\right)/\mathrm{d}z \geq 120\,\mathrm{mK}$ (Singh et al. 2017; 2018). Their results were confirmed by the Experiment to Detect the Global EoR Signature[9] (EDGES; Bowman et al. 2008), which rejected at 2σ significance all models with a reionization duration $\Delta z \leq 0.4$ if the mid-point is in the $z = 6.7 - 11.7$ range and all scenarios with $\Delta z \leq 1$ if the mid-point is $z = 8.5$ (Monsalve et al. 2017). These results assume a hot reionization scenario, i.e. where $T_\mathrm{s} \gg T_\gamma$. Monsalve et al. (2017) relaxed this assumption and considered also the cold reionization model (see §2.3), where the IGM is not heated by X-ray sources before reionization ($T_\mathrm{s} = T_\mathrm{k} < T_\gamma$). They rejected at high significance (i.e., more than 2σ) all models with duration $\Delta z < 2$ if the mid-point is in the range $z = 6.5 - 11$. These later results are somewhat in tension with constraints on the duration of reionization from CMB anisotropy measurements $\Delta z < 3$ at 1σ significance (George et al. 2015), implying that the cold reionization scenario is disfavoured.

Bowman et al. (2018) reported the first 21 cm detection as an absorption profile centered at 78 MHz, i.e. $z \approx 18$, with a width at half-maximum of approximately 19 MHz and an amplitude of about 500 mK. This result is still very controversial. Indeed, the amplitude is a factor of two larger than expected (Cohen et al. 2017), which can be explained if the baryon-photon decoupling occurs at $z > z_\mathrm{dec}$ or with undetected high-redshift radio sources which increase the CMB temperature (Fialkov and Barkana 2019). Also exotic scenarios has been proposed, such as interactions between baryons and little charged DM particles (Barkana 2018) or DM annihilation (Cheung et al. 2019). Recently, Natwariya and Bhatt (2020) try to explain the excess in the amplitude with the α-effect (Sur et al. 2008; Brandenburg and Subramanian 2007) due to the gas turbulence, which twists and enhance magnetic field lines at the cost of

---

[6] `http://www.lofar.org/`

[7] `http://www.tauceti.caltech.edu/LWA/`

[8] `http://www.rri.res.in/DISTORTION/saras.html/`

[9] `https://www.haystack.mit.edu/ast/arrays/Edges/`

gas energy. With this mechanism, the gas temperature can be lowered to 3.2 K at $z \approx 17$, explaining the observed absorption feature with no requirement of new physics. Furthermore, the duration of the absorption feature is so narrow to require a star formation rate higher than expected (Mirocha and Furlanetto 2019). Thus, there are many open questions about the EDGES results and how they were obtained. Indeed, Singh and Subrahmanyan (2019) used a different data analysis method and found results consistent with the standard cosmology and astrophysics. Future experiments, such as the Large-Aperture to Detect the Dark Ages[10] (LEDA; Bernardi et al. 2015; Price et al. 2018) and the Probing Radio Intensity at high-Z from Marion (PRI$^{\rm Z}$M; Philip et al. 2019), will need to confirm their findings.

---

[10] `http://www.tauceti.caltech.edu/leda/`

Chapter 3

Foregrounds

This chapter aims to provide an overview of the observational challenges of the 21 cm experiments, in particular those concerning the foreground emission. We summarize the basic concepts of interferometry, the different foreground components relevant to 21 cm observations and, finally, the current methods used for their mitigation.

3.1 Fundamentals of radio interferometry

The 21 cm line emitted from HI during the EoR is redshifted from 1420 MHz to frequencies below 200 MHz (which correspond to $z = 6$, see §2.2.1). Celestial radio signals can be observed from the Earth surface as the atmosphere is transparent in the radio window. At cm-wavelengths, parabolic dishes are generally built to collect celestial radio waves and focus them in the focal plane where it is placed a feed, a device that converts radio waves into electrical signals.

The angular resolution θ_b of a single dish with a diameter D is given by λ/D, where λ is the wavelength of the observed radiation. The bigger the dish, the higher the resolution power (defined as the inverse of the angular resolution). The construction of very large single dish telescopes is, however, limited by engineering and economic perspectives. Higher angular resolutions are achieved with *interferometric arrays*, where many antennas are connected together to “synthesize” an aperture of diameter equivalent to the maximum separation between antennas b:

$$\theta_b \approx \frac{\lambda}{b}, \tag{3.1}$$

where b is also known as the maximum *baseline* of the array. Orders of magnitude improvement in the angular resolution can be achieved using this method.In next section we summarize the formalism needed to understand interferometric measurements.

3.1.1 Interferometry

The simplest interferometric array is the two-element interferometer (Figure 3.1a): an array of N antennas is simply $N(N-1)/2$ independent two-element arrays. Let us, therefore, consider a two-element interferometer that consists of two identical antennas separated by a baseline length $b = |\mathbf{b}|$ and observing along the direction $\hat{\mathbf{s}}$. Any sky source is sufficiently distant that its incoming radiation can be safely approximated as a plane wave. If the antennas observe the source at an angle θ respect to zenith, the wavefront received by the left antenna experiences an extra delay τ with respect to the right one:

$$\tau = \frac{\mathbf{b} \cdot \hat{\mathbf{s}}}{c} = \frac{b \sin\theta}{c}, \tag{3.2}$$

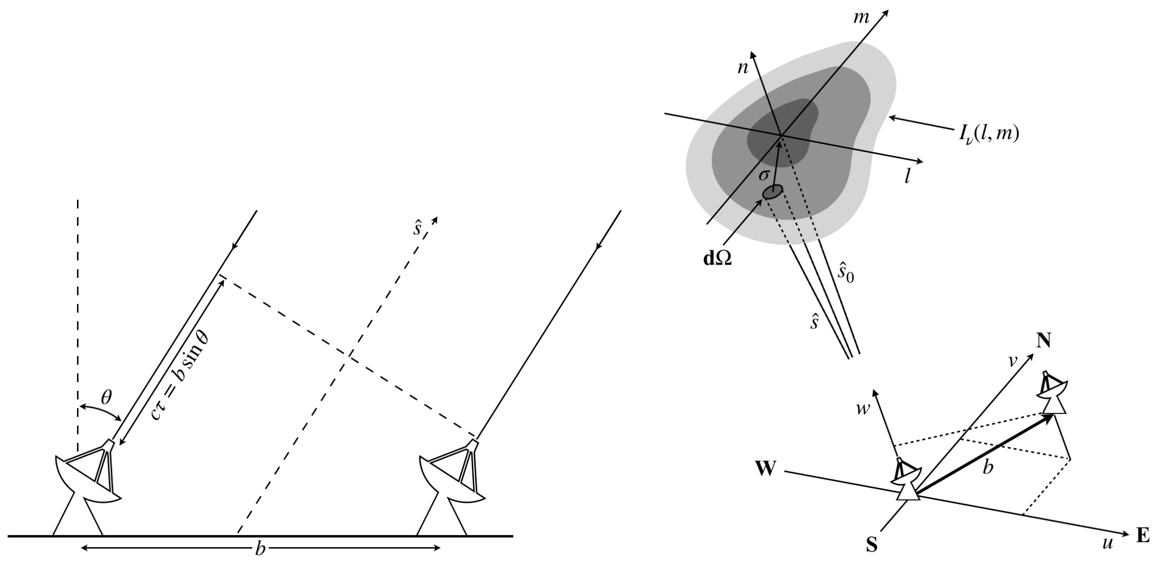

(a) **(b)**

Figure 3.1 (a) Geometry of a two-element interferometer, where b is the baseline length and $\hat{\mathbf{s}}$ is the observing direction with an angle θ with respect to zenith. (b) Relationship between sky coordinates (l, m, n), where the source has a brightness distribution $I_\nu(l, m)$, and the uv-plane. The interferometer is pointing in the direction $\hat{\mathbf{s}}_0$ and observing a source with solid angle $\mathrm{d}\Omega$ in the direction $\hat{\mathbf{s}} = \hat{\mathbf{s}}_0 + \boldsymbol{\sigma}$. Cardinal points are reported.

where τ is often referred to as the *geometric time delay*. The two signals are combined by the *correlator*. In particular, the voltage induced at the right antenna can be written as $\mathcal{V}(t) = \mathcal{V}\cos(2\pi\nu t)$ and the correlator performs the time average between the signals of the two antennas (e.g., Thompson et al. 2017):

$$\begin{aligned} r = \langle \mathcal{V}_i(t)\,\mathcal{V}_j(t)\rangle &= \langle \mathcal{V}^2 \cos[2\pi\nu(t-\tau)]\cos(2\pi\nu t)\rangle \\ &= \frac{\mathcal{V}^2}{2}\langle \cos(4\pi\nu t - 2\pi\nu\tau) + \cos(2\pi\nu\tau)\rangle \\ &= \frac{\mathcal{V}^2}{2}\langle \cos(2\pi\nu t)\cos(4\pi\nu\tau) + \sin(2\pi\nu t)\sin(4\pi\nu\tau) + \cos(2\pi\nu\tau)\rangle, \end{aligned} \tag{3.3}$$

where $\langle\rangle$ indicates the time average, i and j are the left and right antennas, respectively, t is the time, ν the observing frequency and the geometrical delay was added to the signal received by the left antenna. For any observing frequency ν, the quantity νt varies faster than $\nu\tau$ and, if the correlator averages over a period $\gg 1/\nu$, $\langle\cos(2\pi\nu t)\rangle = \langle\sin(2\pi\nu t)\rangle = 0$ and Eq. 3.3 can be written as (e.g., Thompson et al. 2017)

$$r(\tau) \approx \frac{\mathcal{V}^2}{2}\cos(2\pi\nu\tau) = \frac{\mathcal{V}^2}{2}\cos\left(2\pi\nu\frac{\mathbf{b}\cdot\hat{\mathbf{s}}}{c}\right). \tag{3.4}$$

The correlator output is therefore a square voltage that varies sinusoidally with time, known as *fringe pattern*. Eq. (3.4) is valid for a point source, but also describes the contribution from a source element of solid angle $\mathrm{d}\Omega$ in the direction $\hat{\mathbf{s}} = \hat{\mathbf{s}}_0 + \boldsymbol{\sigma}$ as shown in Figure 3.1b, where $\hat{\mathbf{s}}_0$ is the reference position on the sky, known as *phase center*, where the visibility phase is zero by construction (i.e., $\mathbf{b}\cdot\hat{\mathbf{s}}_0 = 0$). Thus, the *fringe phase* can be defined as

$$\phi_f = 2\pi\nu\frac{\mathbf{b}\cdot\boldsymbol{\sigma}}{c}, \tag{3.5}$$

such that a source observed at the phase center has $\phi_f = 0$, and, therefore, a constant amplitude $r = \mathcal{V}^2/2$.

The visibility expression for an extended source can be obtained by integrating $r(\tau)$ over the source size Ω (e.g., Bernardi 2019):

$$R(\mathbf{b},\nu) = \int_\Omega \frac{\mathcal{V}^2}{2}\left[\cos\left(2\pi\nu\frac{\mathbf{b}\cdot\hat{\mathbf{s}}}{c}\right) - i\sin\left(2\pi\nu\frac{\mathbf{b}\cdot\hat{\mathbf{s}}}{c}\right)\right]\mathrm{d}\Omega = \int_\Omega \frac{\mathcal{V}^2}{2}\, e^{-2\pi i\nu\frac{\mathbf{b}\cdot\hat{\mathbf{s}}}{c}}\,\mathrm{d}\Omega, \tag{3.6}$$

where an odd (sine) function is added to the even cosine component in order to describe any general, complex-value function. Indeed, the source signal is a real function that generally has both even and odd parts, then to sample it completely the complex correlator adds a 90° phase shift to one of the signal paths before cross-multiplication, obtaining the sine component of Eq. (3.6). Furthermore, the signal amplitude $\mathcal{V}^2/2$ is proportional to the source brightness $I_\nu(\boldsymbol{\sigma})$, which is a direction dependent quantity. Thus, Eq. (3.6) can be written as (e.g., Bernardi 2019)

$$R(\mathbf{b},\nu) = e^{-2\pi i\nu\frac{\mathbf{b}\cdot\hat{\mathbf{s}}_0}{c}}\int_\Omega A_\nu(\boldsymbol{\sigma})I_\nu(\boldsymbol{\sigma})\, e^{-2\pi i\nu\frac{\mathbf{b}\cdot\boldsymbol{\sigma}}{c}}\,\mathrm{d}\Omega, \tag{3.7}$$

where we substituted $\hat{\mathbf{s}} = \hat{\mathbf{s}}_0 + \boldsymbol{\sigma}$ and added the *primary beam* response $A_\nu(\boldsymbol{\sigma})$, which takes into account the fact that the antenna sensitivity decreases away from the pointing direction. The exponential term outside the integral in Eq. (3.7) varies with time and is generally canceled out adding a time delay equal and opposite to the exponent. The additional delay can be applied on the correlator itself in tracking telescopes or on the measured visibilities in drift scan telescopes, in order to combine observations made at different times. This operation is known as fringe stopping or delay tracking: for a given set of observations, we choose a reference time, fixing the phase center, and re-phase all data to that with a rotation of the fringes phase (more details in Thompson et al. 2017).

Eq. (3.7) defines the complex *visibility* V, i.e. the fundamental quantity measured by an interferometer (van Cittert 1934; Zernike 1938):

$$V_{ij}(\mathbf{b},\nu) = |V_{ij}|e^{i\phi_v} = \int_\Omega A_\nu(\boldsymbol{\sigma})I_\nu(\boldsymbol{\sigma})\, e^{-2\pi i\nu\frac{\mathbf{b}\cdot\boldsymbol{\sigma}}{c}}\,\mathrm{d}\Omega, \tag{3.8}$$

where ij is the baseline between antenna i and j, $|V_{ij}|$ and ϕ_v are the visibility amplitude and phase respectively, given by

$$|V_{ij}| = \sqrt{\mathrm{Re}\{V_{ij}\}^2 + \mathrm{Im}\{V_{ij}\}^2} \quad ; \quad \phi_v = \tan^{-1}\left(\frac{\mathrm{Im}\{V_{ij}\}}{\mathrm{Re}\{V_{ij}\}}\right) \tag{3.9}$$

and correspond to the fringe amplitude and phase (Eq. 3.5), the latter measured relative to the fringe phase at $\hat{\mathbf{s}}_0$. Eq. 3.8 is also known as the *Van Cittert-Zernike* theorem.

Visibilities are often defined in a different coordinate system, where the baseline vector $\mathbf{b}$ has components (u, v, w) as shown in Figure 3.1b: the uv-plane is normal to the phase center direction, such that w is measured in the direction $\hat{\mathbf{s}}_0$. In particular, u is measured toward North and v toward East. Similarly, a coordinate system for imaging can be defined by taking the unit vector $\hat{\mathbf{s}}$ with components (l, m, n): the lm-plane is tangent to celestial sphere, its origin ($l = m = 0$) is at the phase center, and n is along the w direction. The coordinates (l, m) are called *direction cosines* because they are defined as

$$l = \sin\theta_x \quad ; \quad m = \sin\theta_y, \tag{3.10}$$

where θ_x and θ_y are the sky coordinates, and hence they are the cosines of angles with respect to the u and v directions. Both (l, m, n) and (u, v, w) are dimensionless coordinates, as the latter are defined as $\mathbf{u} = \mathbf{b}/\lambda = \mathbf{b}\nu/c$, where $\mathbf{u} = (u, v, w)$.

In these new systems, we can write (e.g., Thompson et al. 2017)

$$\frac{\nu\mathbf{b}\cdot\hat{\mathbf{s}}_0}{c} = w \quad ; \quad \frac{\nu\mathbf{b}\cdot\hat{\mathbf{s}}}{c} = ul + vm + wn \quad ; \quad \mathrm{d}\Omega = \frac{\mathrm{d}l\,\mathrm{d}m}{n} = \frac{\mathrm{d}l\,\mathrm{d}m}{\sqrt{1 - l^2 - m^2}} \tag{3.11}$$

and Eq. (3.8) becomes

$$V_{ij}(u,v,w,\nu) = \int_\Omega A_\nu(l,m) I_\nu(l,m)\, e^{-2\pi i[ul+vm+w(\sqrt{1-l^2-m^2}-1)]}\, \frac{\mathrm{d}l\,\mathrm{d}m}{\sqrt{1-l^2-m^2}}, \tag{3.12}$$

where we have taken into account that $\mathbf{b}\cdot\boldsymbol{\sigma} = \mathbf{b}\cdot\hat{\mathbf{s}} - \mathbf{b}\cdot\hat{\mathbf{s}}_0$. Note that if the source is in the phase center the argument of the exponential term is zero, the visibility phase is also zero, that means that the imaginary part is zero, and hence the amplitude of the signal, i.e. the flux density, corresponds to the real part of the visibility.

If we consider a small region of the sky such that the flat-sky approximation holds and $w = 0$, Eq. (3.12) can be rewritten as

$$V_{ij}(u,v,\nu) = \int_\Omega A_\nu(l,m) I_\nu(l,m)\, e^{-2\pi i(ul+vm)}\, \mathrm{d}l\,\mathrm{d}m, \tag{3.13}$$

which is the two dimensional Fourier transform of the spatial brightness distribution of the sky, where $l \approx \theta_x$ and $m \approx \theta_y$[1]. The sky brightness can be obtained by inverse Fourier transform of Eq. (3.13):

$$A_\nu(l,m) I_\nu(l,m) = \int V_{ij}(u,v,\nu)\, e^{2\pi i(ul+vm)}\, \mathrm{d}u\,\mathrm{d}v. \tag{3.14}$$

We note that, in the flat-sky approximation, the sky coordinates are the Fourier conjugate of the (u,v) coordinates. Each projected baseline samples one point in the uv-plane: in order to fill the uv-plane, one can either increase the number of unique baselines, i.e. baselines that have different lengths and orientations than any other baseline, or take advantage of the Earth rotation, which changes the (u,v) coordinates with time – a technique known as *rotation synthesis* (Ryle and Hewish 1960).

In real applications, however, it is impossible to completely reconstruct the sky brightness distribution, the uv-plane has inevitable gaps[2]. The sky brightness distribution reconstructed with a limited number of uv-modes is referred to as a *dirty image*:

$$I_\mathrm{D}(l,m,\nu) \approx \int S(u,v,\nu) V_{ij}(u,v,\nu)\, e^{2\pi i(ul+vm)}\, \mathrm{d}u\,\mathrm{d}v, \tag{3.15}$$

where $S(u,v,\nu)$ is the sampling function in the uv-plane, i.e. the uv-coverage.

Using the convolution theorem, Eq. 3.15 can be rewritten as

$$I_\mathrm{D}(l,m,\nu) = \widetilde{S}(u,v,\nu) * \widetilde{V}_{ij}(u,v,\nu) = \mathrm{PSF}(l,m,\nu) * I_\nu(l,m), \tag{3.16}$$

where the tilde indicates the Fourier transform and PSF is the Point Spread Function, and, essentially, describes the response of the interferometer to a point source. As $S(u,v,\nu)$ is a discrete, non continuous function, the PSF shows sidelobes that extend over the whole uv-plane. Deconvolution techniques are needed to remove the sidelobe contamination from the dirty image (e.g., Högbom 1974; Clark 1980).

3.1.2 From visibilities to power spectra

As we have seen in §2.5, current arrays do not have enough sensitivity to obtain images of the spatial distribution of the cosmological 21 cm signal, which may be achieved by HERA and the SKA. Current experiments aim to perform a statistical detection by measuring the

---

[1] This Fourier transform convention is different than the definition given in §1.4, but both are standard. In particular, the expression with the 2π factor in the complex exponential is generally used in radio astronomy, whereas the expression without the 2π factor is used in the cosmological context.

[2] For example, the minimum baseline cannot be shorter than the antenna size, thus modes corresponding to $u < D/\lambda$, i.e. large-scale sky emission, cannot be probed. This means, for instance, that an interferometer can not observe an isotropic emission.

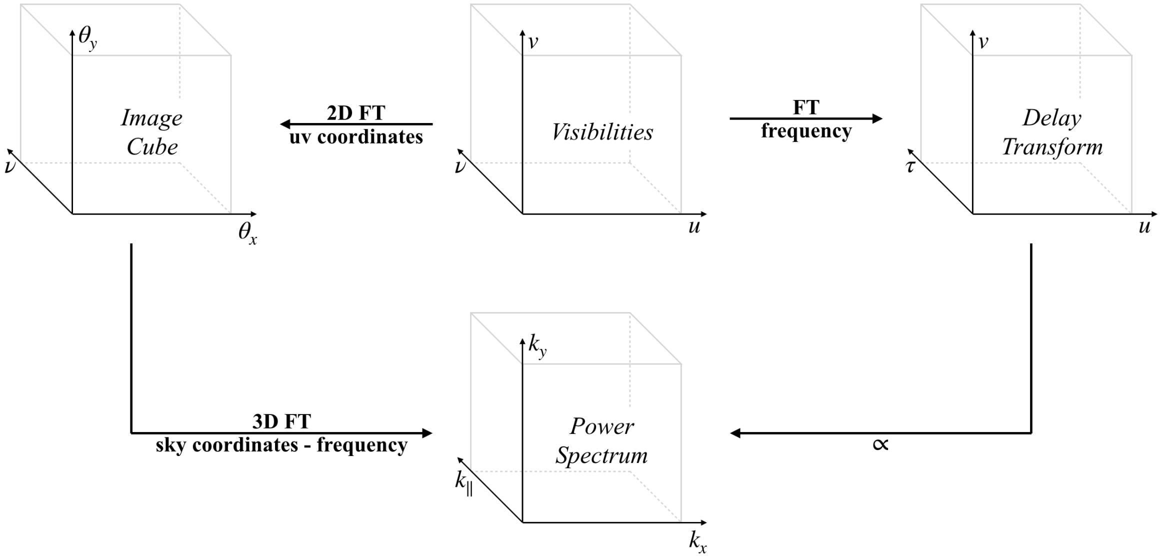

Figure 3.2 Interferometers measure visibilities in the uv-plane as a function of the frequency ν (Eq. 3.13). Power spectra can be obtained in two ways: a spatial, two dimensional Fourier transform of visibilities generate a "standard" image cube with $(\theta_x, \theta_y, \nu)$ coordinates. A three dimensional Fourier transform converts the image plane coordinates to power spectrum coordinates $(k_x, k_y, k_\parallel)$. Alternatively, a Fourier transform along the frequency axis takes the visibilities to the (u, v, τ) coordinates, which are simply proportional to the power spectrum coordinates (see text for details).

21 cm power spectrum. Here we describe how power spectra are related to interferometric measurements.

Figure 3.2 describes two approaches to achieve power spectra. Visibilities are measured by interferometers in the (u, v, ν) space and can be Fourier transformed along the (u, v) coordinates (Eq. 3.14) to obtain an image cube. The specific intensity I_ν can be expressed as a brightness temperature $T(\theta_x, \theta_y, \nu)$ according to Eq. (2.4). If we define $\mathbf{x} = (\theta_x, \theta_y, \nu)$, the power spectrum can be obtained from the image cube first with a three dimensional Fourier transform,

$$\widetilde{T}(\mathbf{k}) \equiv \int_{-\infty}^{\infty} T(\mathbf{x})\, e^{-i\mathbf{k}\cdot\mathbf{x}}\, \mathrm{d}^3x, \tag{3.17}$$

and then by averaging over k-modes of the same length (Eq. (2.21)):

$$\langle \widetilde{T}(\mathbf{k})\, \widetilde{T}^*(\mathbf{k}')\rangle = (2\pi)^3 \delta_{\mathrm{D}}(\mathbf{k} - \mathbf{k}') P(k), \tag{3.18}$$

where * indicates the complex conjugate operator.

On the other hand, the 21 cm power spectrum can be directly obtain from visibilities, as different baselines sample different k-modes. It can be noted from Eq. (3.13) that an interferometer already performs a spatial, two dimensional Fourier transform of the brightness distribution $T(\mathbf{x})$. Visibilities can further Fourier transformed along the frequency axis into a *delay transform* (Parsons and Backer 2009; Parsons et al. 2012a):

$$\widetilde{V}_{ij}(u, v, \tau) = \int_B V_{ij}(u, v, \nu)\, e^{-2\pi i \nu\tau}\, \mathrm{d}\nu, \tag{3.19}$$

where B is the bandwidth of the observation and τ is the Fourier conjugate of the frequency ν. The bandwidth B is generally taken to be $8 - 10$ MHz, over which there is no significant cosmological evolution of the 21 cm signal (e.g., Santos et al. 2005). We note that as visibilities have units of Jy, delay transformed visibilities have units of Jy Hz. Substituting Eq. (3.13) into Eq. (3.19) we obtain

$$\widetilde{V}_{ij}(u, v, \tau) = \frac{2k_{\mathrm{B}}}{\lambda^2} \int A_\nu(l, m) T(l, m, \nu)\, e^{-2\pi i(ul + vm + \nu\tau)}\, \mathrm{d}l\, \mathrm{d}m\, \mathrm{d}\nu, \tag{3.20}$$

where we have expressed the specific intensity I_ν as the brightness temperature $T(l, m, \nu)$ and λ is the observing wavelength.

It can be shown that the (u, v, τ) coordinate system maps into $(k_x, k_y, k_\parallel)$ and, therefore, the delay transform $\widetilde{V}$ is essentially equivalent to $\widetilde{T}(\mathbf{k})$. Let us consider the narrow-field, flat-sky approximation, such that $l \approx \theta_x$ and $m \approx \theta_y$, and neglect the variation of (u, v) coordinates with delay (i.e., $\mathbf{u} = \mathbf{b}\nu/c$), an approximation that is valid for baselines shorter than 300 m (Parsons et al. 2012a). The observational quantities $(\theta_x, \theta_y, \nu)$ can now be related to the cosmological $\mathbf{x} = (\mathbf{x}_\perp, x_\parallel)$, where $\mathbf{x}_\perp$ and $x_\parallel$ are the comoving position vectors perpendicular and parallel to the line of sight, respectively. Eq. (1.10) describes the comoving distance between the present time (i.e., $z_{\rm obs} = 0$) and the redshift z, and can be rewritten as

$$x(z) = \frac{c}{H_0} \int_0^z \frac{{\rm d}z'}{E(z')}, \tag{3.21}$$

where in the ΛCDM model $E(z) = \sqrt{\Omega_{0,m}(1+z)^3 + \Omega_{0,\Lambda}}$ since both $\Omega_{0,K}$ and $\Omega_{0,\gamma}$ are negligible (see §1.2). In the small-angle approximation, the comoving transverse distance is then defined as $\mathbf{x}_\perp = x(z)\,\boldsymbol{\theta}$, where $\boldsymbol{\theta} = (\theta_x, \theta_y)$. Supposing $\theta_x = \theta_y = \theta$, the components of the vector $\mathbf{x}_\perp$ are $D_c = x(z)\,\theta$ and have units of h^{-1}Mpc rad. Eq. (3.21) is also useful to express the radial comoving distance corresponding to a redshift interval Δz centered at z:

$$\Delta x_\parallel = \Delta x(z) = \frac{c\Delta z}{H_0 E(z)} = \frac{c\Delta\nu(1+z)^2}{\nu_{21} H_0 E(z)}, \tag{3.22}$$

where Δz was derived as a function of $\Delta\nu$ from the relation $\nu = \nu_{21}(1+z)^{-1}$. As the frequency and the radial distance are measured relative to the central value of the observational band, we can replace $\Delta x_\parallel$ and $\Delta\nu$ with $x_\parallel$ and ν, respectively. Similarly to the transverse comoving distance, we can indicate with ΔD_c the radial distance $\Delta x_\parallel$, which has units of h^{-1}Mpc. At this point, we can relate the Fourier mode $\mathbf{k} = (\mathbf{k}_\perp, k_\parallel)$ to the position vector $\mathbf{x} = (D_c, D_c, x_\parallel)$:

$$\mathbf{k}_\perp = \frac{2\pi\nu}{cD_c}\mathbf{b} \quad ; \quad k_\parallel = \frac{2\pi\nu_{21} H_0 E(z)}{c(1+z)^2}\,\tau. \tag{3.23}$$

Finally, the power spectrum can be expressed related to the the delay transformed visibilities (Parsons et al. 2012a; Thyagarajan et al. 2015):

$$P(k) = |\widetilde{V}_b(\tau)|^2 \left(\frac{\lambda^2}{2k_{\rm B}}\right)^2 \left(\frac{D_c^2\,\Delta D_c}{B}\right)\left(\frac{1}{\Omega B}\right), \tag{3.24}$$

where λ is the center wavelength of the observing bandwidth, $\Omega \approx \lambda^2/A_{\rm eff}$ is the field of view (FOV) solid angle, with $A_{\rm eff}$ the effective area of the antenna. The units of Eq. (3.24) are mK^2(h^{-1}Mpc)^3.

3.2 Foreground emission

At low radio frequencies, the sky emission is dominated by Galactic and extragalactic foregrounds, which are three to four orders of magnitude brighter than the redshifted 21 cm signal, (Figure 3.3a, Shaver et al. 1999; Jelić et al. 2008). The Galactic emission is associated with diffuse synchrotron and free-free radiations from the Milky Way, whereas the extragalactic one is mainly due to point sources, such as radio AGNs and galaxy clusters. In Figure 3.3b the angular power spectrum of the 21 cm signal (solid blue line) is compared with the various foreground emission components at 150 MHz: the Galactic component dominates at large angular scales and accounts for about 70% of the total power, while the extragalactic one dominates at small angular scales and accounts for the remaining ∼ 30% (Santos et al. 2005). The contribution of the CMB anisotropies is negligible. A deep knowledge of foreground emission is then fundamental for 21 cm observations, in order to separate it from the cosmological signal.

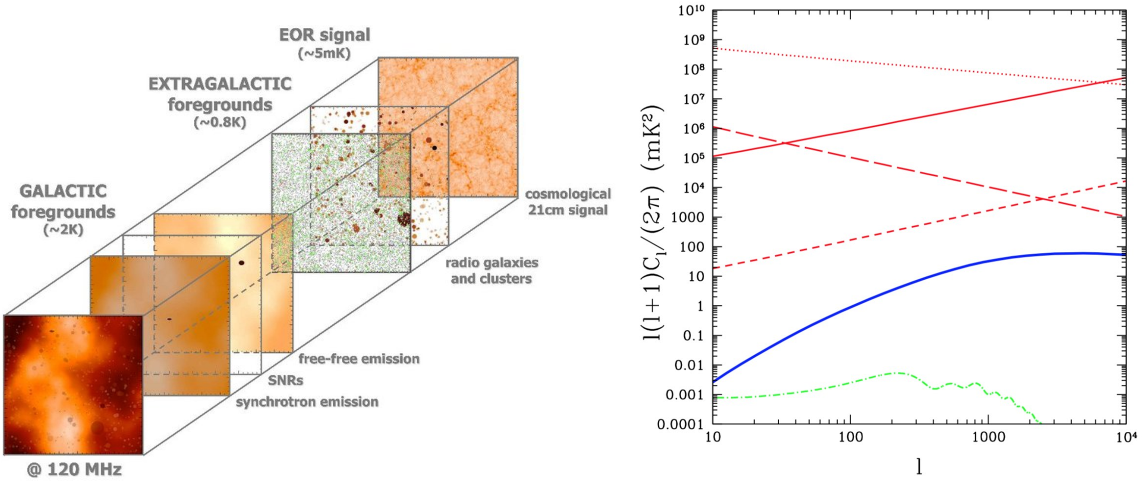

(a) **(b)**

Figure 3.3 (a) Illustration of the various foreground components affecting observations of the cosmological 21 cm signal (Jelić et al. 2008). Typical brightness temperatures of Galactic and extragalactic foregrounds and EoR signal are reported. From `https://www.researchgate.net/profile/Sarod_Yatawatta`. (b) The angular power spectrum at 140 MHz ($z \approx 9.2$) of the 21 cm signal (solid blue line), extragalactic free-free (dashed red line), Galactic free-free (long-dashed red line), point sources (solid red line), Galactic synchrotron (dotted red line) and the CMB (dot-dashed curve). Note that EoR signal is dominated by foreground emission at all scales. From Santos et al. (2005).

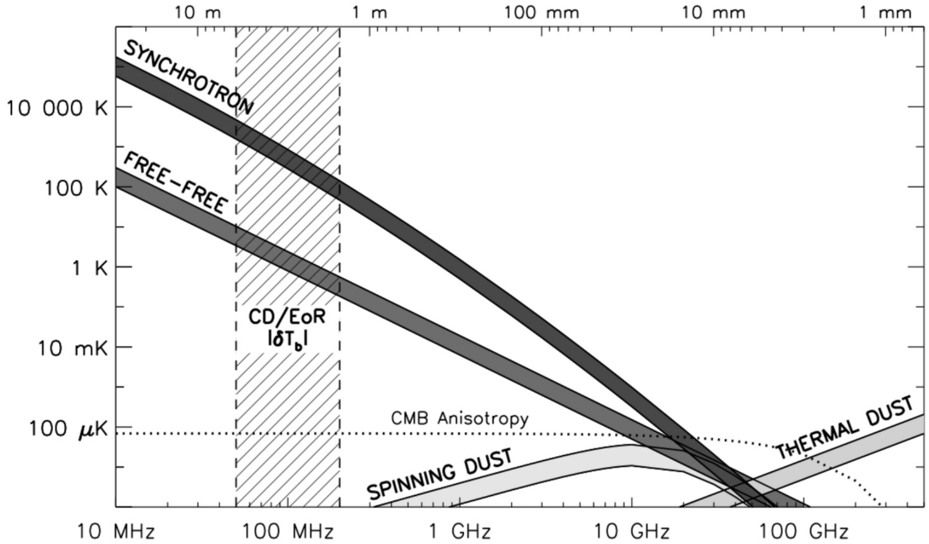

Figure 3.4 Spectra of the various foreground components: Galactic synchrotron, free-free, spinning dust grains and thermal dust. Over the whole frequency range of the Cosmic Dawn and EoR frequencies (dark grey area) the Galactic synchrotron emission is few orders of magnitude brighter than the 21 cm signal. The dotted curve represents the CMB anisotropy spectrum, which is the brightest component in the $30 - 100$ GHz range, after which there is the transition from a synchrotron-dominated foreground to a thermal dust-dominated one. From Chapman and Jelić (2019).

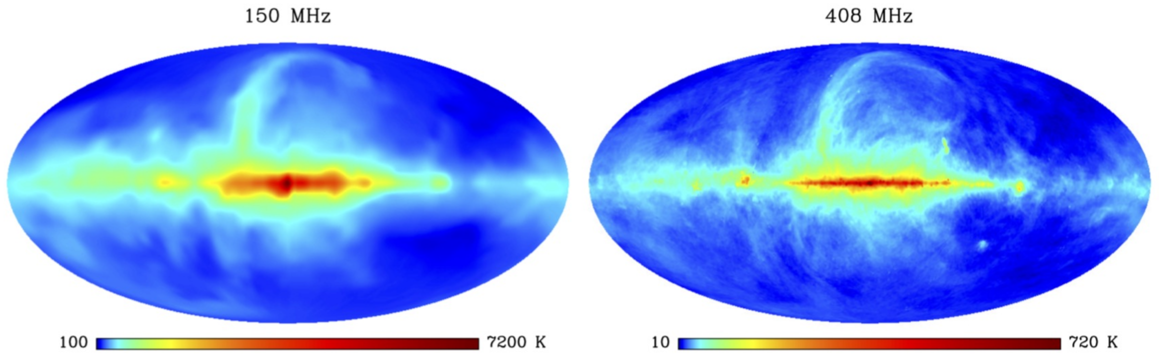

Figure 3.5 All sky maps in brightness temperature of Galactic synchrotron emission at 150 MHz (left, Landecker and Wielebinski 1970) and at 408 MHz (right, Haslam et al. 1982).

3.2.1 Galactic foreground

Galactic synchrotron emission is the dominant component in the EoR frequency range, whereas the free-free emission due to the ionized gas is about three orders of magnitude fainter (Figure 3.4). Free-free is also mostly concentrated in the Galactic plane, with HII regions (e.g., Planck Collaboration et al. 2016a).

Non-thermal synchrotron radiation is emitted when charged particles, essentially cosmic-ray electrons, are accelerated in a magnetic field. The radiation power (energy per unit of time) emitted by a single electron is (e.g., Rybicki and Lightman 1979):

$$\frac{\mathrm{d}E}{\mathrm{d}t} \propto \gamma^2 H^2 \sin^2(\theta_p). \tag{3.25}$$

where γ is the Lorentz factor, H is the magnetic field strength and θ_p is the pitch angle between the electron velocity and the magnetic field. Thus, in the electron rest frame the synchrotron radiation is distributed with a dipole pattern, while it is beamed along the direction of motion in the observer reference frame because of relativistic effects. As the electron spirals around magnetic field lines, it emits radiation over a range of frequencies, peaking at the critical frequency $\nu_{\mathrm{cr}} \propto \gamma^2 H$. This means that the more energetic the electrons the higher frequency of the emitted radiation.

In the Milky Way, relativistic electrons with $\gamma \approx 10^4$ are essentially produced by SNe in the Galactic plane and spiral around the Galactic magnetic field, which has a strength of about 10 µG (e.g., Haverkorn 2015). Their synchrotron emission therefore peaks at radio frequencies, between 10 MHz and 100 GHz. The superposition of broad synchrotron spectra with different critical frequencies leads to an observed power law for the flux density S_ν:

$$S_\nu = S_0 \left(\frac{\nu}{\nu_0}\right)^{-\alpha}, \tag{3.26}$$

where S_0 is the flux density at the reference frequency ν_0 and α is the spectral index. The spectral index changes with observing frequencies: at $\nu > 1$ GHz $0.8 < \alpha < 1$ (Reich and Reich 1988; Platania et al. 1998), whereas at $\nu < 500$ MHz the spectral index is flatter, with $0.1 < \alpha < 0.7$ (Guzmán et al. 2011). The difference between low and high frequencies is due to radiative losses: Eq. (3.25) shows that more energetic particles, whose spectrum peaks at higher frequencies, loose energy more quickly. A population of old particles is therefore expected to have a spectrum that steepens at higher frequencies (e.g., Strong et al. 2007). The most accurate measurements of the synchrotron spectral index at low frequencies are from Mozdzen et al. (2017), which found $0.60 < \alpha < 0.62$ in the $\nu = 90 - 190$ MHz range.

Galactic synchrotron emission also shows a high degree of spatial variations, more concentrated in the Galactic plane but with spurs and structures extending well beyond it (Figure 3.5).

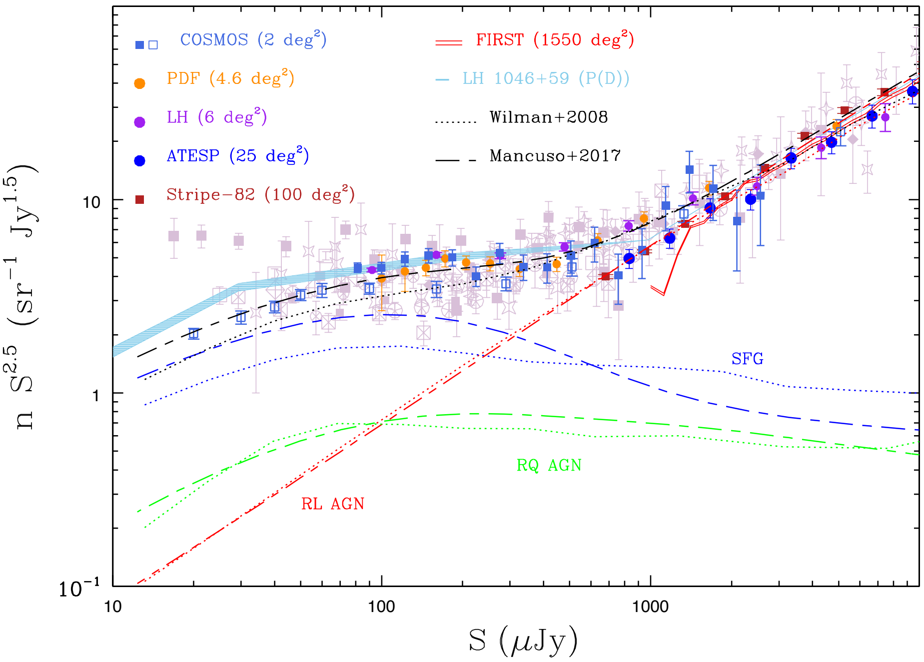

Figure 3.6 Normalized 1.4 GHz differential source counts. Colored symbols indicate different surveys (see Prandoni 2018, for more details). Dotted and dashed lines represent predicted counts from different models (Wilman et al. 2008; Wilman et al. 2010), where colours indicate different populations: SFG (blue), RL AGN (red), RQ AGN (green), and their sum in black. From Prandoni (2018).

This is due to fluctuations in the cosmic-ray density and magnetic field strength across the Galaxy (Chapman and Jelić 2019). At high Galactic latitudes, the synchrotron emission varies between 150 and 250 K at 150 MHz (Landecker and Wielebinski 1970).

3.2.2 Extragalactic foreground

Extragalactic sources are mainly AGNs and star forming galaxies (SFGs). The radio emission in AGNs, known in this case as radio-loud (RL) AGNs, is due to relativistic jets produced by the central accretion disk and extending up to Mpc scales (e.g., Urry and Padovani 1995; Heckman and Best 2014). These jets generate a diffuse plasma of electrons, which emits synchrotron radiation because of the high magnetic field strength in the AGN nucleus. RL AGNs are typically at the center of elliptical galaxies, whereas radio-quiet (RQ) AGNs[3], i.e. AGNs with no large-scale radio jets, can be found also in spiral ones (e.g., Kormendy and Ho 2013). Indeed, SFGs have an high infrared luminosity, that is generally associated to the star-formation rate (Jarvis et al. 2010).

Normalized differential source counts at 1.4 GHz are shown in Figure 3.6 for different flux density thresholds. SFGs dominate the extragalactic emission below approximately 100 µJy, whereas RL AGNs contribute the most at flux densities greater than 1 mJy. Deep surveys in the frequency range of the redshifted 21 cm line are important to understand the spatial distribution of foreground sources and their spectra.

Indeed, source clustering can affect the detection of the cosmological signal on large angular scales, i.e. at $k < 0.6\,h\,\mathrm{Mpc}^{-1}$ (Murray et al. 2017; 2018). The knowledge of radio spectra is instead fundamental in the foreground separation methods (see §3.3), which are based on the assumption of spectral smoothness (Bernardi et al. 2015). Deviations from the spectral smoothness of extragalactic sources are expected at low-frequencies as a consequence

---

[3] An AGN is defined radio-loud when the ratio between the radio luminosity at 5 GHz and the optical luminosity in the blue filter is greater than 10, otherwise it is defined radio-quiet AGN (Kellermann et al. 1989).

of synchrotron self-absorption, that leads to a spectral index $\alpha \approx -0.5$ below a turnover frequency that generally is between 10 MHz and 1 GHz (Kellermann and Pauliny-Toth 1969; Pacholczyk 1970). Current surveys, however, do not show strong evidence for spectral curvature. Callingham et al. (2017) studied sources in the the Galactic and Extragalactic All-sky MWA (GLEAM; Hurley-Walker et al. 2017) survey, finding that only $\sim 4.5\%$ of them have a turnover between 72 MHz and 1.4 GHz. Also the spectrum of Fornax A (RA $= 3^{\mathrm{h}}22^{\mathrm{m}}41.72^{\mathrm{s}}$, Dec $= -37^{\circ}12'29.62''$; Shaya et al. 1996), which is one of the brightest source in the Southern sky, is very smooth, as Bernardi et al. (2013) measured a spectral index $\alpha = -0.88 \pm 0.05$ in the range $30 - 400$ MHz. Thus, deviations from smooth power-law spectra seem to be insignificant for the foreground mitigation, which we will describe in the next section.

3.3 Foreground Mitigation

In the previous section we have seen that Galactic and extragalactic foregrounds are mainly due to synchrotron emission, whose spectrum is expected to be smooth over tens of MHz. Conversely, the coherence scale of the 21 cm signal is of the order of a few MHz (Di Matteo et al. 2002; Santos et al. 2005). This different spectral behaviour allows us to separate the foreground emission from the cosmological signal. Specifically, foregrounds can either be modeled and subtracted, or avoided.

3.3.1 Foreground Subtraction

The foreground subtraction approach relies on modeling the foreground emission and fitting it to the observed data. The best fit is then removed from the data. The first step is the subtraction of bright compact sources. Generally, this is done in the visibility space (Yatawatta et al. 2013; Carroll et al. 2016), often including a correction for the instrumental corruptions (e.g., Smirnov 2011). Conversely, LOFAR and MWA may apply the subtraction also in the image plane, fitting a smooth spectral model to each pixel to remove sources in each line of sight (e.g., Morales et al. 2006; Wang et al. 2006). Some of the brightest sources, however, can have complicated, extended morphologies: failures in accurate modeling and, therefore, subtracting these sources leaves residual foreground contamination that may prevent the 21 cm detection (e.g., Procopio et al. 2017).

After bright source subtraction, the sky brightness is dominated by the diffuse foreground emission (e.g., Bernardi et al. 2010; Bernardi et al. 2013). Modeling and subtraction of diffuse synchrotron emission is performed via two main spectral fitting methods:

- **Parametric Fitting**. This method assumes a foreground spectral model whose coefficients are fitted to the data on an image pixel basis (Wang et al. 2006; Bowman et al. 2009; Liu et al. 2009). The most used parametric method is fitting a polynomial function to the foreground spectrum for every pixel of the observed image cube (McQuinn et al. 2006; Bowman et al. 2009). Removal methods may, however, lead to overfit and loose a fraction of the 21 cm signal (Cheng et al. 2018; Wang et al. 2013).

- **Non-parametric Fitting**. In this case, the functional form used to model foregrounds is not fixed a priori, but general assumptions of foreground properties and their statistics are assumed (e.g., Harker et al. 2009; Paciga et al. 2013; Mertens et al. 2018). Although non parametric methods are generally more flexible and robust, they are still vulnerable to calibration errors that introduce spectral structures on the observed foreground spectra.

After subtraction of diffuse foregrounds, residual errors may still be present and, at present, power spectra from observations are hardly ever compatible with thermal noise, indicating a dominating foreground contamination (e.g., Morales and Hewitt 2004; Morales et al. 2006). In

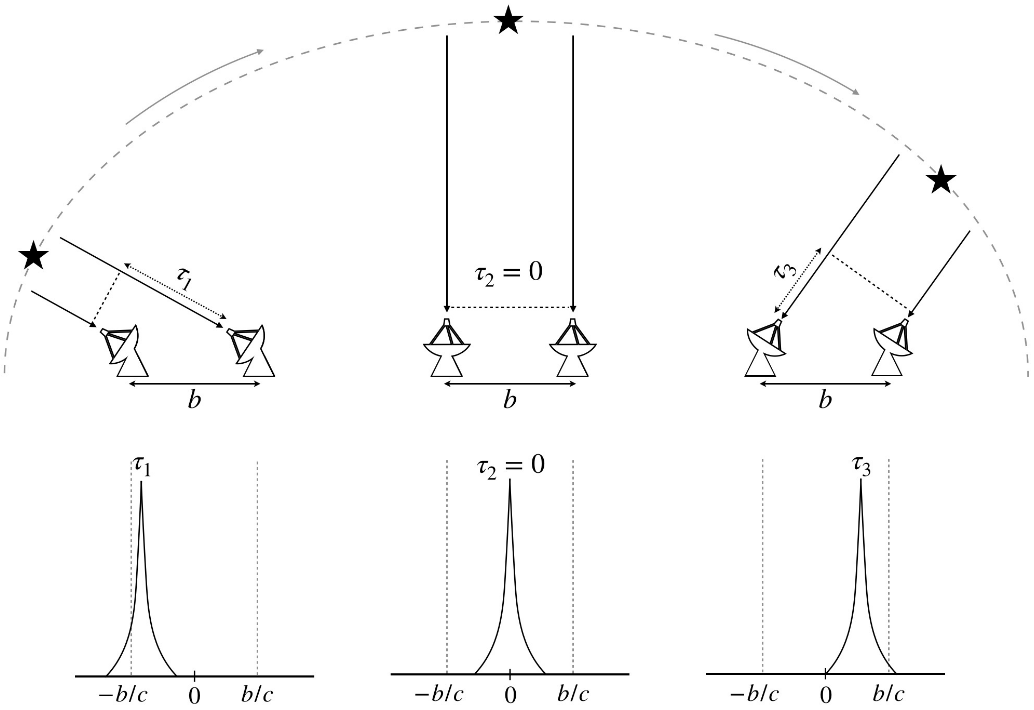

Figure 3.7 Pictorial representation of delay spectra of a flat spectrum source measured by two antennas separated by a baseline b. The source has different delays τ when is at different positions in the sky. Note that at the zenith $\tau = 0$. The bottom part of the cartoon shows the delay response of the antenna pair, where vertical dashed lines denote the horizon limit and the solid lines are the delay transforms of the source at each position, centered at the corresponding delay.

order to remove residual errors, Morales (2005) suggests to simulate power spectra coming from subtraction errors and then subtracting the template that best fits the residuals. This method may be promising to statistically remove the residual contamination but it requires extensive and realistic simulations (Morales et al. 2006) and has not been applied to data so far.

A middle way between subtraction and avoidance methods is represented by *mode weighting*: rather than removing foreground emission, modes with high foreground contamination are downweighted (e.g., Liu and Tegmark 2011; Trott et al. 2016). Indeed, in these modes the cosmological signal is not exactly zero. This method is based on the optimal quadratic estimator formalism, where the covariance matrix describing the various sky components is inverted to downweight foreground emission (Liu and Tegmark 2012; Dillon et al. 2013). The power spectrum is then estimated over all k-modes, each mode weighted by the inverse covariance matrix, such that foreground dominated ones are negligible but not completely zero. This is particularly important in those k-space regions where foreground and EoR signal can be comparable, i.e. near the wedge (see §3.3.2), which are instead rejected in the avoidance method. The challenge with the mode weighting method is related to the modelling of foreground covariance, which is difficult at low-frequencies due to incompleteness of current surveys (Liu and Shaw 2019). However, the current best power spectrum values at $z < 8$ have been obtained by Trott et al. (2020) using the mode weightning technique (see §2.5 and Figure 5.7).

3.3.2 Foreground Avoidance

The avoidance method is based on the fact that foregrounds and the cosmological 21 cm signal have different spectral behaviours, which leave different footprints in the power spectrum domain. In order to illustrate the basics of avoidance, we consider two antennas separated

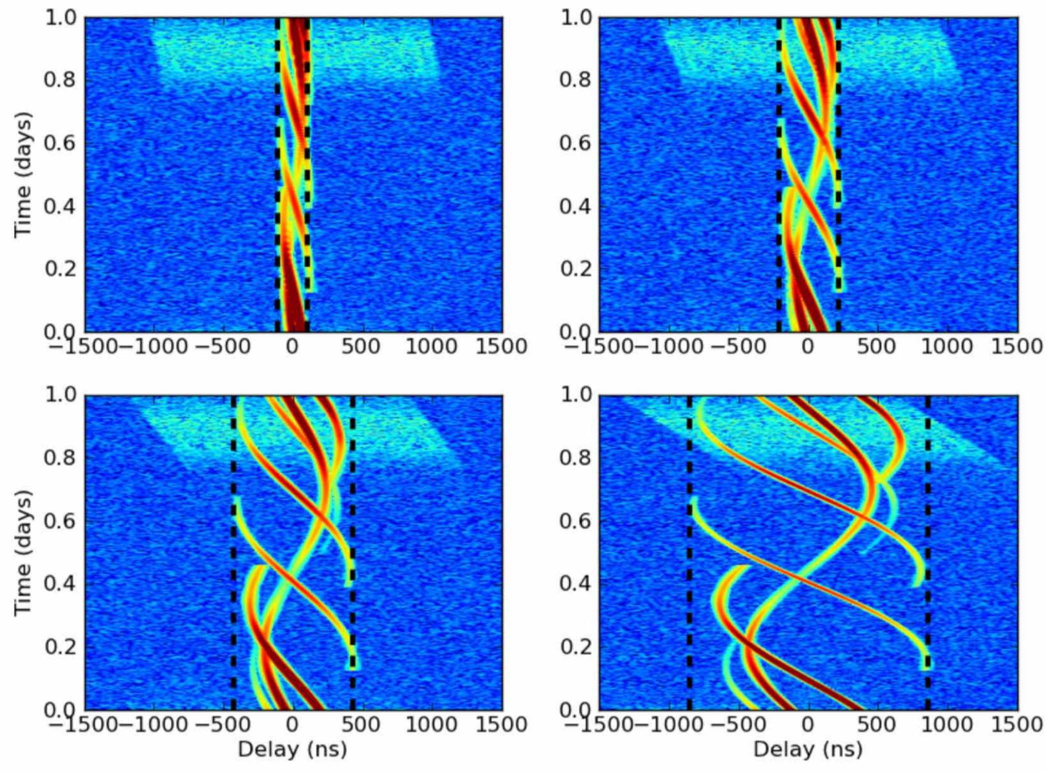

Figure 3.8 Amplitude of delay transformed visibilities as a function of time and delay for a simulated sky, including power-law spectra point sources for a 32 m (top left), 64 m (top right), 128 m (bottom left) and 256 m (bottom right) baseline (see Parsons et al. 2012a, for further details). Light blue colour refers to a 21 cm toy model. Color scale is logarithmic, ranging from 1 in blue to 5 in red. Black dashed lines mark the horizon limits for each baseline length. Note that smooth spectrum sources are confined inside the horizon, whereas the 21 cm signal spread to high delay values. From Parsons et al. (2012a).

by a baseline of length b and observing a point source (Figure 3.7). The signal observed from a flat spectrum source is a delta function centered at a given geometrical delay τ. As the source moves across the sky, it will appear at different locations in delay space (Parsons et al. 2012a). The maximum delay allowed, however, is always bound by a physical limit that corresponds to the separation between the two antennas, $\tau_{\max} = b/c$, which occurs when the source is at the horizon and is, therefore, named horizon limit (Vedantham et al. 2012; Parsons et al. 2012b). This simple scenario holds as long as the sky emission remains frequency smooth: a power-law emission will still remain bound in delay space, although extending a little beyond the horizon limit. Conversely, unsmooth emission is not bound to any specific delay limit, but has power across the whole delay range (Figure 3.8). In other words, the EoR signal varies on a few MHz scales (see §2.4) and, therefore, has non negligible power beyond the horizon limit where smooth spectrum foregrounds are confined. This region is referred to as the EoR region because the 21 cm signal is expected to be stronger than foregrounds and, in principle, detectable without subtraction.

The boundaries of the EoR window depend upon the instrumental configuration and are highlighted in the two dimensional, cylindrical $(k_{\parallel}, k_{\perp})$ power spectrum – as $k_{\perp} \propto b$ and $k_{\parallel} \propto \tau$ (Eq. 3.23) – shown in Figure 3.9. The boundaries of this plane are (Vedantham et al. 2012; Chapman et al. 2014):

$$k_{\perp,\max} = \frac{2\pi\nu_{21} b_{\max}}{c(1+z)D_c} \quad ; \quad k_{\perp,\min} = \frac{2\pi\nu_{21} b_{\min}}{c(1+z)D_c} \tag{3.27}$$

$$k_{\parallel,\max} = \frac{2\pi\nu_{21} H_0 E(z)}{c(1+z)^2\Delta\nu} \quad ; \quad k_{\parallel,\min} = \frac{2\pi\nu_{21} H_0 E(z)}{c(1+z)^2 B}, \tag{3.28}$$

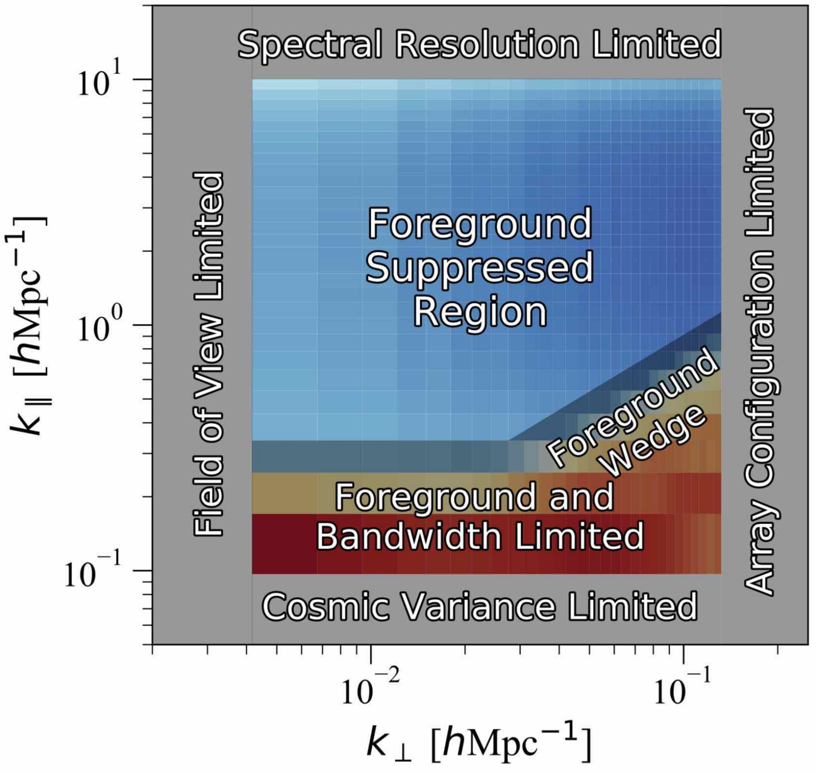

Figure 3.9 Cartoon representation of the two dimensional, cylindrical $(k_\parallel, k_\perp)$ power spectrum relevant for the avoidance method. Smooth spectrum foreground emission should be contained in the horizontal band at small $k_\parallel$ values, but the intrinsic chromaticity of interferometers leaks power at higher $k_\parallel$, in the region known as wedge. The blue remaining region is the EoR window, where foreground is suppressed because of their smooth spectra. From Liu and Shaw (2019).

where $\Delta\nu$ is the channel width, and $b_{\rm min}$ and $b_{\rm max}$ are the minimum and maximum baseline of the array, respectively. Note that $b_{\rm min}$ cannot be smaller than the antenna size, so that $k_{\perp,{\rm min}}$ is associated to the FOV. The lower boundary of the EoR region corresponds to the maximum delay $\tau_{\rm max}$:

$$\tau_{\rm max} = \frac{b}{c} = \frac{D_c}{2\pi\nu}\,k_\perp = \frac{D_c(1+z)}{2\pi\nu_{21}}\,k_\perp \tag{3.29}$$

and, substituting it in the definition of $k_\parallel$ (Eq. 3.23), we obtain the horizon limit relation in k-space (e.g., Thyagarajan et al. 2013):

$$k_\parallel = \frac{2\pi\nu_{21}H_0E(z)}{c(1+z)^2}\,\tau_{\rm max} = \frac{H_0E(z)D_c}{c(1+z)}\,k_\perp. \tag{3.30}$$

The horizon limit marks the boundary of the *foreground wedge* (Datta et al. 2010; Liu et al. 2014a; 2014b). The foreground wedge is due to the intrinsic chromaticity of interferometers, because its (u, v) sampling changes with frequency, i.e. $u = b\nu/c$. Eq. (3.30) shows that the extension of the foreground dominated region is larger for longer baselines (Parsons et al. 2012a; Morales et al. 2012). Observations often show emission that bleeds outside the horizon limit, likely due to the instrument primary beam, calibration errors and intrinsic unsmooth foreground emission (e.g., Pober et al. 2013).

Unlike foreground subtraction, the avoidance method does not require foreground imaging and modeling. If no imaging is needed, then deploying baselines on a regular grid is advantageous as it boosts the power spectrum sensitivity on a number of limited $k_\perp$ modes (Parsons et al. 2012a). This was the rationale behind the construction of several arrays, including PAPER, whose data analysis was the topic of this thesis and will be described in the next chapters.

Chapter 4

PAPER observations

In this chapter, we describe the Donald C. Backer Precision Array to Probe the Epoch of Reionization (PAPER; Parsons et al. 2010) and the data taken with the 128-element configuration. In particular, we derive the noise statistics of our data and describe the method used to estimate the 21 cm power spectrum, validating it with simulations. For our analysis we develop Python scripts and make use of the Common Astronomy Software Applications (CASA) environment.

4.1 Observations and data analysis

PAPER was a low-frequency radio interferometer built to observe the power spectrum of the 21 cm line. It was located in the Karoo Desert, in the Northern Cape of South Africa, and was deployed in stages. The first deployment consisted of 8 antennas (Parsons et al. 2010), augmented to 32 elements (Pober et al. 2013; Parsons et al. 2014; Jacobs et al. 2015; Moore et al. 2017), 64 (Ali et al. 2015; Cheng et al. 2018; Kolopanis et al. 2019) and finally to 128 (Zhang et al. 2018). The configuration of the 128-element array (PAPER-128 henceforth), which we used in this Thesis work, is shown in Figure 4.1. It consists of 112 elements distributed on a 16×7 regular grid, in order to maximize the redundancy (see also Figure 4.2a), and 16 outrigger elements, placed outside the grid on a perimeter of about 300 m, in order to improve the uv-coverage.

The PAPER receiver consists of two crossed sleeved dipoles (Johnson 1993) between two aluminium disks, and mounted in a ground screen with planar wire-mesh reflectors positioned at an angle of 45° outward (Figure 4.2b). The resulting antenna has a collecting area of approximately $4\,\mathrm{m}^2$. The two dipoles measure two orthogonal polarization, i.e. x and y. In this Thesis work we analyse only the xx visibility data. PAPER operates at frequencies between 100 MHz and 200 MHz, divided in 203 channels with a spectral resolution of ~ 0.5 MHz.

The data used in this Thesis were taken during the longest observing season, between November 2013 and March 2014. This season is divided in two epochs, where the difference between them is is due to the number of available antennas, as reported in Table 4.1 (see also Figure 4.1). Visibilities are recorded with an integration time $t_{\rm int} = 31.65\,\mathrm{s}$ and written to disk in a single visibility file 10 minutes long that we will refer to as a snapshot. Although the PAPER correlator does not perform any fringe stopping, the visibilities in each snapshot were phased offline to the coordinates corresponding to the last observing time sample of the snapshot. The monochromatic uv-coverage for a 10 minutes snapshot at 150 MHz is shown in the left panel of Figure 4.3. At a given time, each antenna pair marks two point in the uv-plane, one with (u, v) coordinates and its Hermitian conjugate with $(-u, -v)$ coordinates. Figure 4.3 also shows the uv-coverage for a 10 MHz sub-band, which is used for the power spectrum analysis (see §4.1.1). The sampled uv-cell changes linearly with frequency for each baseline, resulting in a net increase in the uv-coverage.

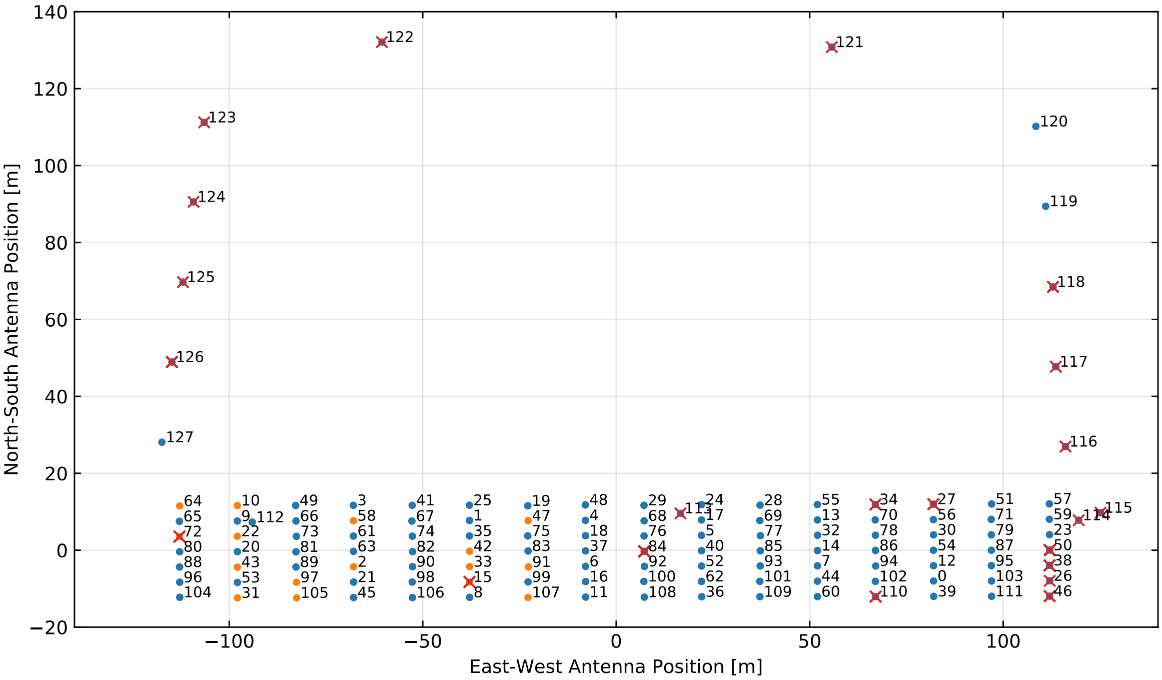

Figure 4.1 Antenna positions of PAPER-128. All antennas were working during epoch 2, while only the blue ones were functioning during epoch 1 (i.e., orange ones were off). Red crosses denote flagged antennas during the calibration and analysis process (see §4.1.2).

(a) **(b)**

Figure 4.2 (a) Aerial view of array in the Karoo region (South Africa from `https://www.astro.phy.cam.ac.uk/research/research-projects/paper-and-hera`. (b) Zoom into a single PAPER antenna, where we can see the crossed sleeved dipole between two aluminium disks (from `http://eor.berkeley.edu`).

Epoch	Calendar Date	Julian Date (JD)	Days	N
1	22/11/2013 – 12/12/2013	2456617 – 2456639	16	112
2	24/01/2014 – 22/02/2014	2456682 – 2456711	26	128

Table 4.1 Details of the observations analyzed in this work. We have 16 and 26 days from epoch 1 and 2, respectively, corresponding to the reported calendar and Julian dates (JD2000). The difference between the two epochs is due to the number of available antennas, indicated with N.

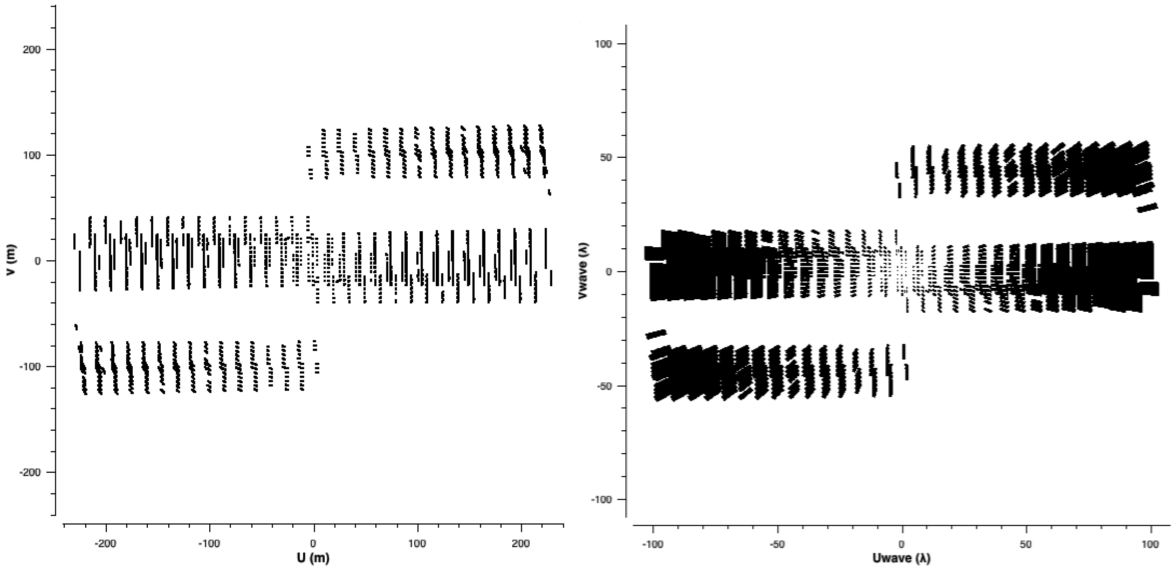

Figure 4.3 Monochromatic *uv*-coverage of a 10 minutes snapshot at 150 MHz (left panel) and over a 10 MHz bandwidth (right panel). Note that in the wide-band coverage the coordinates are in units of wavelength.

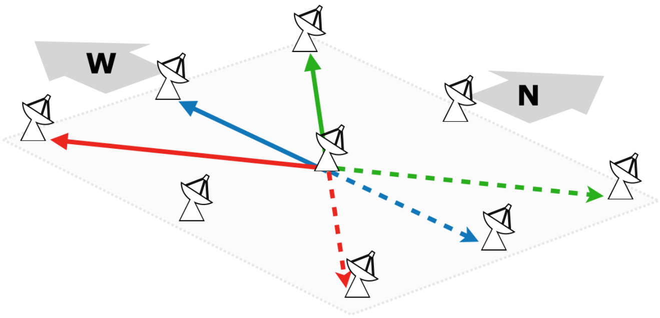

Figure 4.4 Representation of the baseline types used in the analysis: East-West (EW, blue solid arrow), East-West-North (EWN, green solid arrow), East-West-South (EWS, red solid arrow), West-East (WE, blue dashed arrow), West-East-South (WES, green dashed arrow) and West-East-North (WEN, red dashed arrow) baselines. Note that baselines plotted with arrows of the same color sample the same Fourier k-mode, but with inverted delay τ.

The redundant layout of PAPER-128 allows multiple measurements of few Fourier k-modes. The shortest North-South separation between two antennas is 4 m, while it is 15 m East-West. Although the 15 m baselines are the most numerous and would offer the greatest power spectrum sensitivity, in this Thesis we used the 30 m baselines which were always used in previous works (e.g., Ali et al. 2015; Kolopanis et al. 2019). The use of the 30 m baselines provides a more straightforward comparison with previous works and minimizes mutual coupling effects that are more prominent in shortest spacings (Kohn and Aguirre 2015).

We considered three types of 30 m baselines: East-West (EW), i.e. baselines from antennas with no row separation (e.g., 64-49, Figure 4.1), East-West-North (EWN), i.e. baselines from antennas with one row separation such that u and v have the same sign (e.g., 64-66), and East-West-South (EWS), i.e. baselines from antennas with one row separation such that u and v have the opposite sign (e.g., 22-58). EWN and EWS are diagonal baselines whose length is only 1% greater than the 30 m EW baselines and, therefore, can be included in the analysis as they essentially measure the same Fourier mode on the sky. Each type has a corresponding group, where the baseline orientation is inverted and the baseline is the complex conjugate

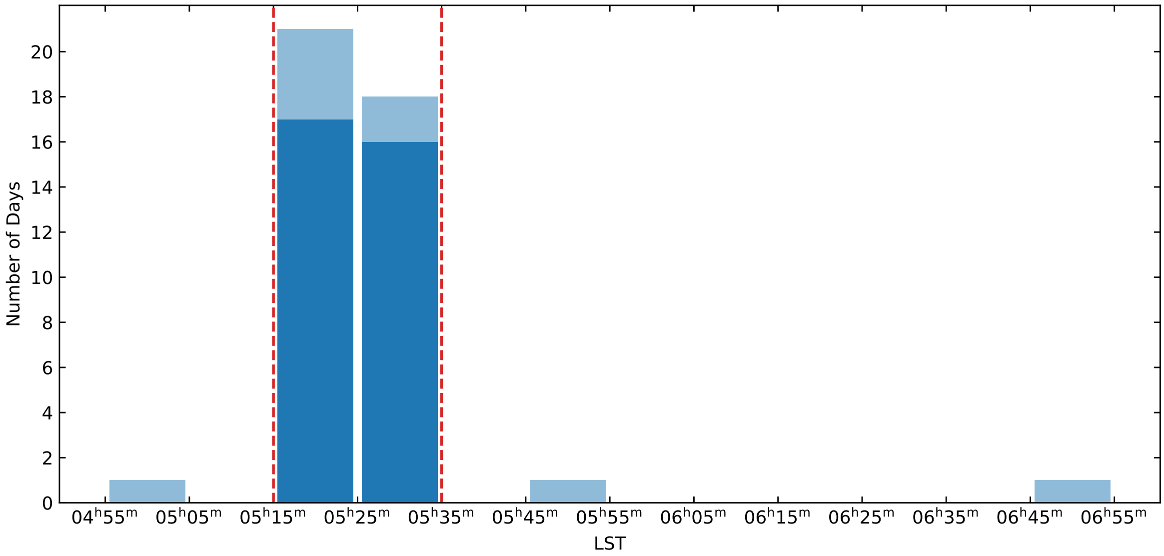

Figure 4.5 Number of days in each Local Sidereal Time (LST) bin, where days are selected based on their phase center coordinates. The light blue bars are the all 42 days, whereas the dark blue bars are the ones used for the analysis. We have re-phased visibilities in a common phase center at RA = $5^{\rm h}25^{\rm m}$, keeping the 39 days with a maximum pointing distance of 10 minutes from the new phase center, in order to avoid visibility decorrelation. The LST range considered is represented with vertical dashed red lines. Furthermore, six observations contained bad data (see text), so that only 33 days were retained in the analysis.

of itself[1] (Figure 4.4). In terms of power spectrum, the other three groups with the inverted baseline orientation still sample the same $|k|$ mode (they just have an opposite delay) and were included in the power spectrum analysis too.

4.1.1 Data selection

PAPER is a drift scan interferometer, i.e. it points at zenith while the sky drifts overhead as the Earth rotates. Although PAPER observes continuously over 24 hours, our analysis is limited to the $0^{\rm h} < {\rm RA} < 8^{\rm h}$ range, which is the coldest sky patch available as the Galactic center is below the horizon (e.g., Ali et al. 2015). In a drift scan array like PAPER pointing direction can be expressed in terms of local sidereal time (LST), which are observed over multiple days. Our analysis includes 42 days centered at LST $\approx 5^{\rm h}$, around Pictor A transit (RA = $5^{\rm h}19^{\rm m}49.72^{\rm s}$, Dec = $-45°46'43.78''$; Evans et al. 2010) that is used as a calibration source (see §4.1.2), for a total of $\sim$ 7 hours of observations. The LST distribution of the snapshots is reported in Figure 4.5.

We re-phased all snapshots from all days to a common phase center, in order to be able to image all the days and average the visibilities coherently (see §4.4). As data are distributed preferentially around LST $\approx 5^{\rm h}25^{\rm m}$, we chose this LST as the RA of the new phase center for all the snapshots. The re-phasing operation changes the uv-coverage, therefore it is important that the projected length of the 30 m baselines does not vary too much across each snapshots, in order to still measure the same $k_\perp$ mode. We found that the projected baselines changes less than 0.1% from the nominal 30 m length across 10 minutes. We excluded the three snapshots that are farthest away from LST $\approx 5^{\rm h}25^{\rm m}$ ad other six snapshots that suffered from calibration errors (see §4.1.2), leaving us with 33 days, for a total of 5.5 hours of observation.

---

[1] The reason for this lies in the baselines ordering required by CASA, where the first antenna needs to have an identifying number smaller than the second one. In principle the ordering could be inverted, but this would break the CASA convention and it would not be able to make images. We kept the current ordering for the purpose of this work.

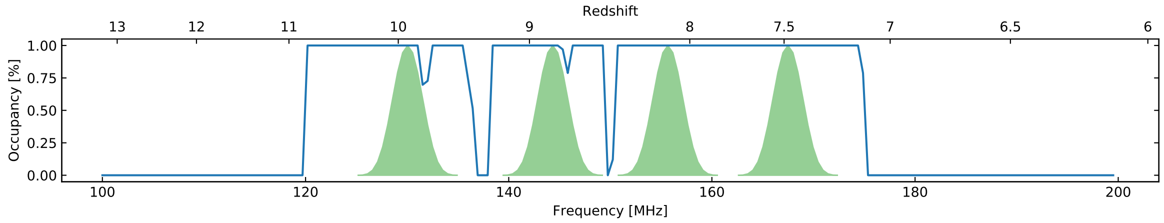

Figure 4.6 The relative fraction, i.e. occupancy, of unflagged days in each frequency channel (blue line). The four 10 MHz sub-bands selected for our analysis are shown with green areas, whose shape is the Blackman-Harris function used as a window function during the delay transform in order to decrease foreground leakages to large delays (e.g., Vedantham et al. 2012). The sub-band are chosen following Kolopanis et al. (2019) and their center was slightly shifted if necessary to avoid flagged channels. The top axis reports the redshift corresponding to each frequency.

A further data selection was carried out along frequency. The 21 cm power spectrum estimation is always made in sub-bands that are $8-10$ MHz wide, where the evolution of the cosmological 21 cm signal is negligible (Wyithe and Loeb 2004; Furlanetto et al. 2006). Here we followed Kolopanis et al. (2019) and selected four 10 MHz-wide spectral windows centered at 130.0 MHz, 144.3 MHz, 155.6 MHz and 167.5 MHz, corresponding to $z = 9.93$, 8.84, 8.13 and 7.48, respectively (Figure 4.6). The spectral windows were carefully chosen in order to avoid to have any channel permanently flagged, which can generate extended sidelobes in the delay space when the Fourier transform is applied to data along the frequency axis (Parsons and Backer 2009; Parsons et al. 2012a).

4.1.2 Flagging and calibration of data

Data used in this Thesis work were previously flagged and calibrated by Nunhokee (2018) and we will review the details in this section. Indeed, the first step of the data analysis is flagging bad data. Examples of data to be discarded include:

- malfunctioning antennas (red crosses in Figure 4.1) or corrupted baselines;
- scan edges;
- bad weather or pointing;
- sub-band edges (i.e., bandpass filter);
- radio frequency interference (RFI, due to satellites or airplanes, for instance).

RFI often appears as narrow-frequency spikes in the visibility data, with an amplitude that is a few orders of magnitude higher than the average visibility. Nunhokee (2018) flagged these bad data with the *tfcrop* algorithm implemented in the CASA software.

After flagging, interferometric calibration is needed because observed visibilities are corrupted by the instrumental response, which is mathematically expressed in terms of antenna based gains g (e.g., Hamaker et al. 1996; Smirnov 2011). Calibrated visibilities $V_{ij,\mathrm{cal}}$ are obtained as

$$V_{ij,\mathrm{cal}}(\nu) = [g_i(\nu)]^{-1}[g_j^*(\nu)]^{-1}V_{ij,\mathrm{obs}}(\nu), \tag{4.1}$$

where ij is the baseline between antenna i and j, and $V_{ij,\mathrm{obs}}(\nu)$ are the observed visibilities. The calibration process aims to determine the complex gains normally by observing a source with known properties, point-like and isolated, a so-called calibrator. Given the wide field of view, PAPER observations cannot effectively isolate sources. However, Nunhokee (2018) obtained a good calibration by considering a simple sky model, consisting only of Pictor A,

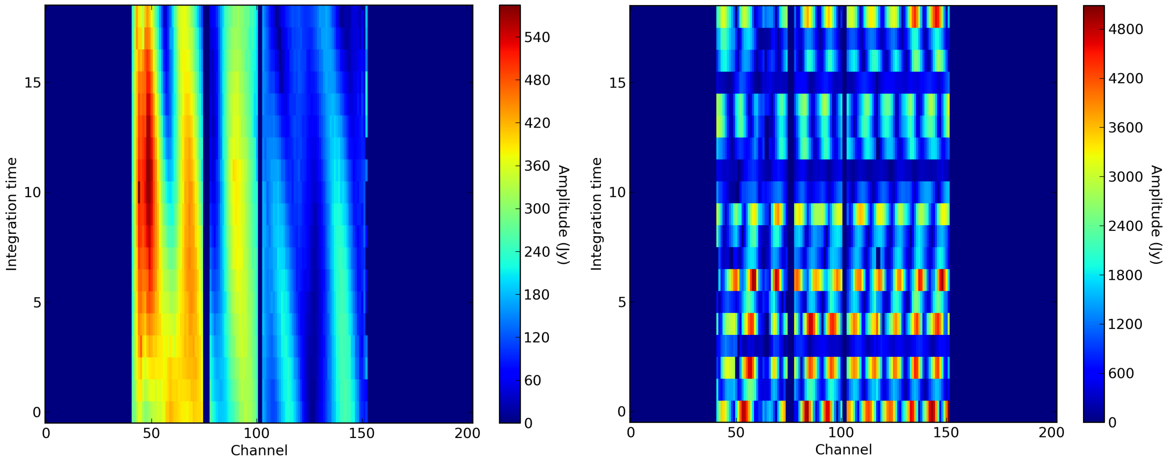

Figure 4.7 Visibility amplitudes as a function of time and frequency, averaged over all the 30 m baselines, from JD2456639 (left panel) and JD2456702 (right panel). The two data sets present an evident difference in the amplitude, which varies smoothly along channels in the former day but not in the latter. Here there are narrow peaks with amplitudes one order of magnitude larger than the maximum value observed in the left panel. Moreover, we expect negligible spectral variation across integration times. This is true for JD2456639 but not for JD2456702. These spectral differences between the two data sets may results from unflagged residual RFI or calibration errors in the latter day. Data sets with behaviours similar to JD2456702 are classified as bad data and discarded in the power spectrum analysis.

which is unresolved at the PAPER angular resolution of ~ 15 arcmin. When Pictor A is near the transit, it is the brightest sources and its visibilities dominate over the rest of the sky, allowing to be treated, in first approximation, as an individual calibrator (Nunhokee 2018). Absolute calibration was obtained by assuming a model for the primary beam and Pictor A to have a flux density $S_0 = 382$ Jy at $\nu_0 = 150$ MHz and a spectral index $\alpha = -0.76$ (Jacobs et al. 2013).

Despite a careful procedure, residual calibration errors are still present in six snapshots. In Figure 4.7 we see different spectral behaviours between data with (right panel) and without (left panel) calibration errors: bad data present narrow peaks along the frequency axis in almost all integration times, strongly affecting power spectrum estimates. These six snapshots are then discarded in the following analysis, as already mentioned in §4.1.1.

4.2 Sky images

After re-phasing, we combined the all the observing days into a single image for each sub-band of interest (Figure 4.8) using the CASA software. Images were made with the multi-frequency synthesis algorithm to improve the uv-coverage and uniform weights in order to suppress sidelobes over the whole field of view. Images were deconvolved using the Clark algorithm (Clark 1980). As we described in §3.1.1, a reconstruction of the sky brightness distribution needs deconvolution from the point spread function. Initially, the deconvolution process identifies the peak of the dirty image and assumes it to be intrinsic sky emission. A fraction of the peak intensity, set by the loop gain, convolved with the dirty beam in the peak position is subtracted at the peak position:

$$I_D = \gamma[\mathrm{CC}(\delta_\mathrm{D}) * \mathrm{PSF}] = I_R, \tag{4.2}$$

where $\mathrm{CC}(\delta_\mathrm{D})$ is the clean component, i.e. an ideal delta function, γ is the loop gain and I_R is the residual dirty map. This operation is repeated several times, using I_R as the new dirty image I_D, until minimum flux density is reached in the residual image. The ensemble of the

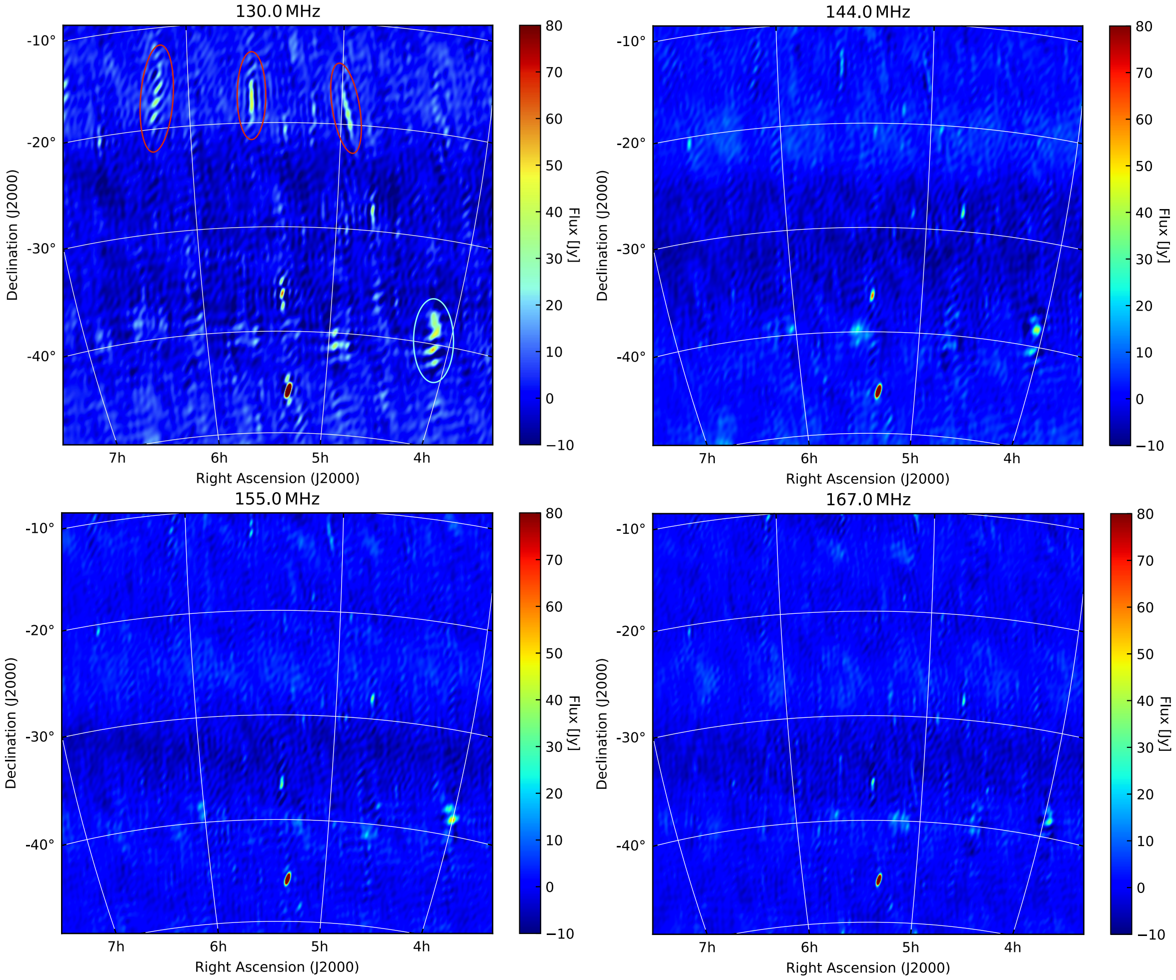

Figure 4.8 Images centered at RA = $5^{\mathrm{h}}25^{\mathrm{m}}0.0^{\mathrm{s}}$, Dec = $-30°46'17.5''$, obtained combining all the snapshot observations (5.5 hours) and using a 10 MHz bandwidth. Top left panel: image at 130.0 MHz, with $\sigma_{\mathrm{rms}} = 4.3\,\mathrm{Jy\,beam^{-1}}$ noise and $53.7 \times 18.1\,\mathrm{arcmin}^2$ angular resolution. Sidelobes due to Fornax A and Taurus A are indicated with red and cyan circles, respectively. Top right panel: image at 144.3 MHz, with $\sigma_{\mathrm{rms}} = 2.5\,\mathrm{Jy\,beam^{-1}}$ noise and $48.0 \times 16.3\,\mathrm{arcmin}^2$ angular resolution. Bottom left panel: image at 155.6 MHz, with $\sigma_{\mathrm{rms}} = 1.9\,\mathrm{Jy\,beam^{-1}}$ noise and $44.3 \times 15.0\,\mathrm{arcmin}^2$ angular resolution. Bottom right panel: image at 167.5 MHz, with $\sigma_{\mathrm{rms}} = 1.4\,\mathrm{Jy\,beam^{-1}}$ noise and $41.5 \times 13.9\,\mathrm{arcmin}^2$.

clean components form the model visibilities. The next step is the “restoring”, which convolves each CC(δ_D) with the cleaned beam. The latter is obtained with a Gaussian fit on the main lobe of the dirty beam, discarding sidelobes. The cleaned map is then obtained. The Clark algorithm we used applies the subtraction described by Eq. (4.2) in the uv-plane rather than in the image plane. We set the loop at $\gamma = 0.2$ and terminated deconvolution once the peak of the residual image was less than 10 Jy.

Images at the four frequencies are fairly consistent with each other and mostly show point source-like emission, with Pictor A being the brightest source. No specific diffuse emission is noticeable down to the sensitivity level, which is indicated with σ_{rms} (i.e., the root mean square). We note that the image quality remains limited due to the poor uv-coverage. A few artifacts remain visible in the maps, mostly at 130.0 MHz (top left panel): sidelobes from Fornax A and Taurus A (RA = $5^{\mathrm{h}}34^{\mathrm{m}}31.97^{\mathrm{s}}$, Dec = $+22°00'52.06''$; McNamara 1971), which are outside the field of view, are left in the image. To avoid their improper deconvolution we stopped the cleaning in this sub-band at a threshold of 70 Jy, which however left residual sidelobes around Pictor A too.

4.3 System Noise

An accurate knowledge of the system noise is relevant in our analysis as it establish a reference baseline for the residual power spectrum. In other words, it allows us to quantify whether the power spectrum modes measured in the EoR region are noise or systematic limited.

In the Rayleigh-Jeans domain, the signal power is generally expressed as an equivalent temperature T – i.e., the physical temperature of the matched load on the feed input – through the approximation of the black-body radiation law (Wrobel and Walker 1999):

$$P = k_{\mathrm{B}} T \Delta\nu, \tag{4.3}$$

where $\Delta\nu$ is the observing bandwidth. After the antenna, the power is amplified by a gain factor G (Thompson et al. 2017):

$$P = P_{\mathrm{a}} + P_{\mathrm{N}} = G k_{\mathrm{B}} \Delta\nu (T_{\mathrm{a}} + T_{\mathrm{sys}}), \tag{4.4}$$

where T_{a} is the *antenna temperature* associated to the power P_{a} of an observed source, and T_{sys} is the *system temperature* associated to the power P_{N} of the system noise. The system temperature is given by the internal thermal noise of the receiver, referred as *receiver temperature* T_{rcvr}, plus the atmospheric and sky emission. In the frequency range of interest, the atmospheric emission is negligible, and we are left with the sky term, which is the sum of Galactic T_{gal} and cosmic $T_{0,\gamma}$ backgrounds (Rogers and Bowman 2008):

$$T_{\mathrm{sky}} = T_{\mathrm{gal}} + T_{0,\gamma} = T_{150} \left(\frac{\nu}{150\,\mathrm{MHz}}\right)^{-\beta} + T_{0,\gamma}, \tag{4.5}$$

where T_{150} is the Galactic synchrotron temperature at 150 MHz and $\beta = \alpha + 2$ is the brightness temperature spectral index. According to the most recent results from EDGES, at RA = $5^{\mathrm{h}}30^{\mathrm{m}}$ we can assume a model with $T_{150} \approx 280$ K and $\beta \approx 2.60$ (Mozdzen et al. 2017), such that $T_{\mathrm{gal}} \gg T_{0,\gamma}$ and the system temperature can be written as

$$T_{\mathrm{sys}} = 280\,\mathrm{K} \left(\frac{\nu}{150\,\mathrm{MHz}}\right)^{-2.60} + T_{\mathrm{rcvr}}, \tag{4.6}$$

where the PAPER receiver temperature is assumed frequency independent, with a value of $T_{\mathrm{rcvr}} = 144$ K (Kolopanis et al. 2019).

The power from the source can be expressed also as a function of the flux density S:

$$P_{\mathrm{a}} = \frac{1}{2} G A_{\mathrm{eff}} S \Delta\nu = G k_{\mathrm{B}} K S \Delta\nu, \tag{4.7}$$

Sub-band (MHz)	A_{diff} -	$\overline{V}_{\text{diff}}$ (Jy)	σ_{diff} (Jy)	SEFD (Jy)	T_{sys} (K)
130.0	$1.13 \cdot 10^4$	-6.73	82	$3.2 \cdot 10^5$	470
144.3	$1.13 \cdot 10^4$	-3.72	74	$2.9 \cdot 10^5$	420
155.6	$1.75 \cdot 10^4$	-5.58	65	$2.5 \cdot 10^5$	370
167.5	$1.47 \cdot 10^4$	6.63	72	$2.8 \cdot 10^5$	410

Table 4.2 Second, third and fourth columns report best fit values to the Gaussian profile (Eq. 4.10) from the distributions in Figure 4.9 as a function of sub-band. SEFD and T_{sys} are reported in the last two columns.

where $K = A_{\text{eff}}/(2k_{\text{B}})$ is a measure of the antenna sensitivity in units of K Jy^{-1}, and the factor of 1/2 takes into account the fact that a single dipole receives only half of the total power from an unpolarized source (Thompson et al. 2017). Since $P_{\text{a}} = Gk_{\text{B}}\Delta\nu T_{\text{a}}$, from Eq. (4.7) we obtain $T_{\text{a}} = KS$. Using this expression for the system noise, we can define the *system equivalent flux density* SEFD as

$$\text{SEFD} = \frac{T_{\text{sys}}}{K} = \frac{2k_{\text{B}}}{A_{\text{eff}}} T_{\text{sys}}. \tag{4.8}$$

While K and T_{sys} give information about antenna and receiver, respectively, the system equivalent flux density is a global measure of the system performance. The SEFD is related to the standard deviation σ_v of the fluctuations in the correlator output signal, i.e. the visibility noise. For two identical antennas, the visibility noise (in Jy) is given by the *radiometer equation* (Wrobel and Walker 1999):

$$\sigma_v = \frac{\text{SEFD}}{\sqrt{2\Delta\nu t_{\text{int}}}}, \tag{4.9}$$

where t_{int} is the integration time. Eq. (4.9) describes the noise of the real and imaginary parts of a visibility.

We aim to estimate the visibility noise in our observations. Following Carilli (2017), we computed the difference per channel and baseline between two adjacent integration times in each sub-band. This operation is based on the assumption that baselines of the same length, at a given LST, observe the same sky signal but have a different thermal noise realization. This is particularly true if we consider adjacent integration times, where the time interval covering two integration times is ~ 1 minute and the sky changes only by $\sim 0.07\%$. The difference is therefore expected to cancel out the sky signal and leave residual visibilities with only the difference between the two noise realizations. The distribution of the real and imaginary parts of these *residual visibilities* V_{diff} should follow a Gaussian distribution:

$$N_{\text{diff}} = A_{\text{diff}} \exp\left[-\frac{(V_{\text{diff}} - \overline{V}_{\text{diff}})^2}{2\sigma^2_{\text{diff}}}\right], \tag{4.10}$$

where A_{diff} is a normalization factor, $\overline{V}$ is the mean – expected to be zero – and σ_{diff} is the standard deviation of residual visibilities. Figure 4.9 displays the distribution of the real part of the residual visibilities $\text{Re}\{V_{\text{diff}}\}$ for 30 m EW baselines[2]. Eq. (4.10) is then used to fit the distributions, with A_{diff}, $\overline{V}_{\text{diff}}$ and σ_{diff} as free parameters. Best fit profiles are plotted with red lines, whose parameter values are reported in Table 4.2. We found a good agreement between the Gaussian profiles and the distribution in each sub-band.

The relationship between the standard deviation σ_{diff} and the visibility noise σ_v is given by the standard propagation error:

$$\sigma_{\text{diff}} = \sqrt{\sigma^2_{v,i} + \sigma^2_{v,i+1}} \approx \sqrt{2}\,\sigma_v, \tag{4.11}$$

---

[2] We considered only EW baselines in order to reduce the computing load.

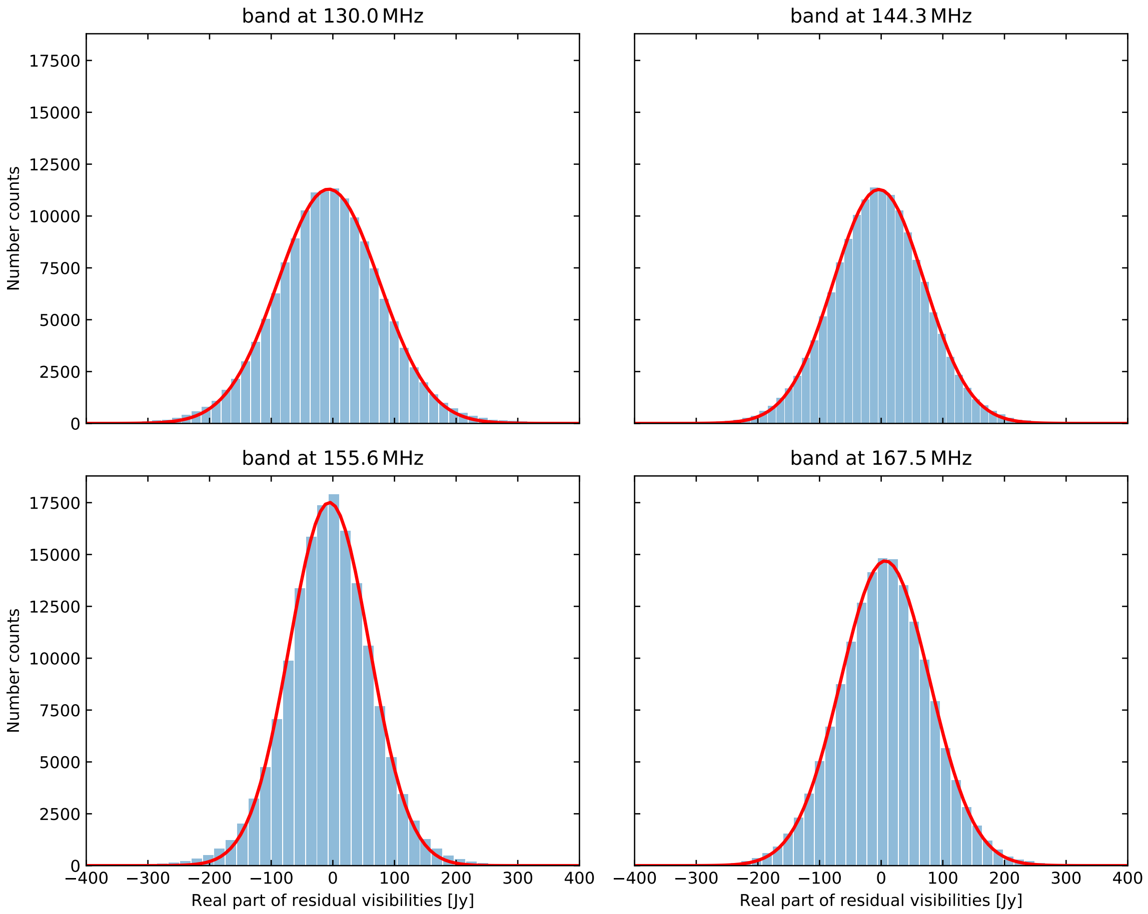

Figure 4.9 Distribution of the real part of the residual visibilities in the sub-bands centered at 130.0 MHz (top left), 144.3 MHz (top right), 155.6 MHz (bottom left) and 167.5 MHz (bottom left) for 30 m EW baselines. Red curves are the Gaussian best fit (Eq. 4.10) to the distributions. Best fit values are reported in Table 4.2. The analysis of the imaginary part of the residual visibilities gave consistent results.

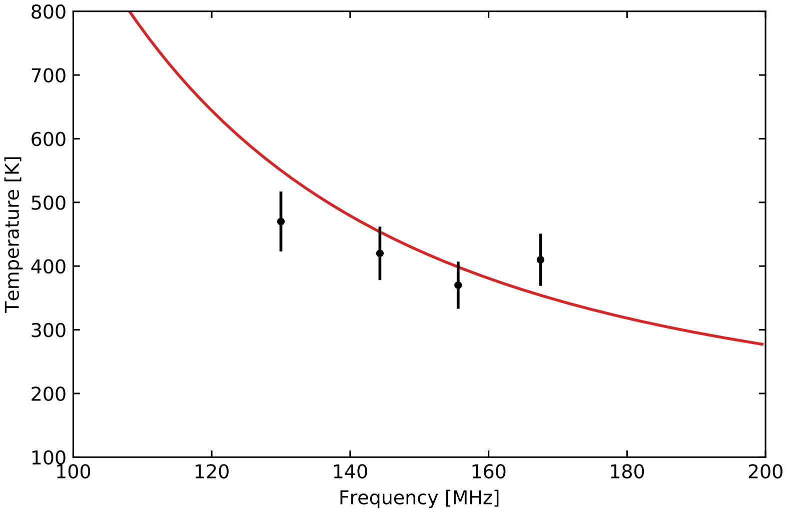

Figure 4.10 Estimated system temperatures as a function of frequency (black points). Error bars are calculated as twice the propagated errors associated to the absolute calibration, which is $\sim 5\%$ (Jacobs et al. 2013). The system temperature expected from Eq. (4.6) is plotted in red. We note the fair agreement between estimates and model predictions.

where i indicates the integration time. Eq. 4.11 holds because the thermal noise in each integration time is a realization from the same zero-mean Gaussian distribution with standard deviation σ_v, i.e. $\sigma_v = \sigma_{v,i} = \sigma_{v,i+1}$ (Eq. 4.9).

Finally, we estimated the SEFD and the system temperature for each sub-band from Eq. (4.9) and Eq. (4.8), respectively, approximating the antenna effective area A_{eff} to the geometrical area, i.e. $\sim 4\,\text{m}^2$ (Table 4.2). Figure 4.10 shows a fair agreement between our system temperature estimates and the model predictions (Eq. 4.6), supporting our assumptions and methodology.

4.4 Power spectrum estimation methodology

In §3.1.2 we introduced the delay transform in order to estimate the power spectrum for a single baseline at a given time, as described by Eq. (3.24). That expression is a good estimator if the delay transform measures only the cosmological signal, but it no longer holds in presence of a dominant noise component. Generally, interferometric measurements take advantages of long observations to reduce the noise. This is obtained through imaging, where all the visibilities are gridded in the *uv*-plane. In particular, visibilities are combined within a *uv*-cell where the averaging is *coherent*, i.e. it preserves phases, and the noise is reduced by $1/\sqrt{N_t}$ (Eq. 4.9). As the power spectrum is proportional to the square of the signal, coherent averaging reduces the power spectrum noise by $1/N_t$. On the other hand, the average of N_t power spectra is *incoherent*, i.e. original phase information is not retained and only the power is averaged, therefore the resulting noise decreases by the usual number of independent measurements, i.e. $1/\sqrt{N_t}$. In other words, coherent averaging reduces the noise level faster than incoherent averaging and should be preferred, when possible. Traditional imaging coherently combines the visibilities, then it is an optimal estimator of the power spectrum and it is used by interferometers who can combine many different baselines, like LOFAR and MWA (e.g., Patil et al. 2017; Barry et al. 2019).

In redundant arrays like PAPER, however, the bulk of the sensitivity comes from one or two (short) baselines and their combination with longer ones does not actually increase the sensitivity but, conversely, reduces the size of the EoR window available for a detection (see §3.3.2). The standard approach used with PAPER observations is to adopt a *single baseline* (i.e., a 30 m baseline length) power spectrum estimator, and we will follow this approach here too. Our power spectrum methodology reduces, then, to the question of how long we can coherently integrate a 30 m baseline before estimating the power spectrum using Eq. (3.24). In other words, we need to estimate how long we can integrate that baseline before its time average decorrelates the signal and degrades the SNR. Ideally, we would like to coherently average each baseline within each snapshot (i.e., over 10 minutes) and over the 33 days. The latter is possible because we have re-phased the visibilities to a common center and we have verified that this operation does not modify the $k_\perp$ value over the snapshot length (see §4.1.1).

In order to verify that visibilities do not decorrelate once averaged over 10 minutes, we performed a simple simulation where a 1 Jy, flat spectrum source is placed at increasing distance from the phase center. We calculated the visibility corresponding to the source for a 30 m EW baseline and for each integration time within a snapshot. Then, we averaged the visibilities over time. We considered distances up to 6 hours in LST, in steps of 30 minutes. The result is shown in the left panel of Figure 4.11: there is no decorrelation - i.e., the visibility amplitude remain constant, equal to the input model - until the offset is less than one hour and decreases rapidly beyond two hours. When the source is three hours away from the phase center, the amplitude is decorrelated by $\sim 10\%$. The right panel of Figure 4.11 is a simulation where we increased the time resolution to 5 minutes, up to a one hour maximum displacement.

Our simulations show that a 30 m baseline can be averaged over time up to one hour with a decorrelation of only 0.1%, which becomes negligible over 10 minutes. This confirms that we

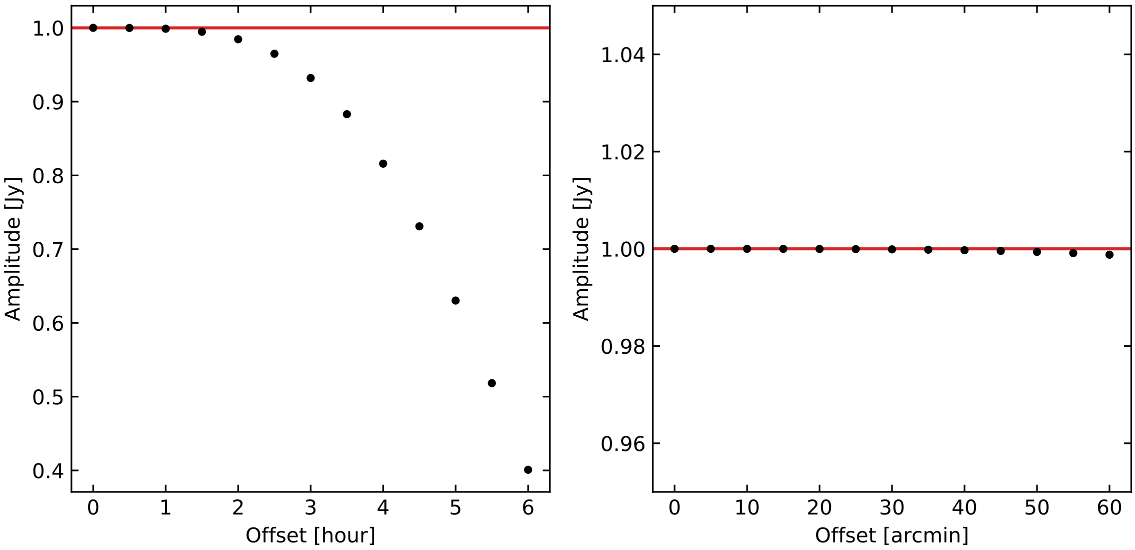

Figure 4.11 Amplitude of the time averaged, 30 m baseline visibility as a function of the source distance from the phase center, where the source has a flux density of 1 Jy (marked with the red line). Decorrelation starts to become significant beyond two hours (left panel) and completely negligible within one hour (right panel). Ali et al. (2015) found similar conclusions based on an analytic estimate of the decorrelation rate.

can average each baseline coherently over time and days and we will follow this approach in estimating the power spectrum.

4.4.1 Power spectrum validation through sky simulations

After visibilities were coherently averaged in time and across days, power spectra can be obtained from Eq. (3.24), i.e. essentially squaring the visibility of each baseline, and then averaging power spectra over all the baselines with the same length. Power spectra obtained following this procedure are also called *auto-spectra*. If we consider the visibility corresponding to a sky signal $V_{\rm S}$ and its noise contribution $V_{\rm N}$, the corresponding delay transform for the baseline b becomes

$$\widetilde{V}_b = \widetilde{V}_{\rm S} + \widetilde{V}_{\rm N}. \tag{4.12}$$

The auto-spectrum averaged over all baselines of the same redundant group then becomes

$$P_{\rm auto} \propto \langle (\widetilde{V}_{\rm S} + \widetilde{V}_{\rm N})(\widetilde{V}_{\rm S}^* + \widetilde{V}_{\rm N}^*) \rangle = \langle |\widetilde{V}_{\rm S}|^2 + \widetilde{V}_{\rm S}\widetilde{V}_{\rm N}^* + \widetilde{V}_{\rm S}^*\widetilde{V}_{\rm N} + |\widetilde{V}_{\rm N}|^2 \rangle \approx P_{\rm S} + P_{\rm N}, \tag{4.13}$$

where the ensemble average of the cross-terms tends to zero under the assumption that sky and noise are not correlated and in the limit of an infinite number of realizations. The average of a number of auto-spectra is then, generally, a biased estimator, because it is a positive defined quantity and the noise power spectrum is added to the sky power spectrum. Such bias is especially relevant in the EoR window, where SNR $\ll 1$.

One way to mitigate the noise bias is to estimate the power spectrum as the average of *cross-power spectra* (i.e., Parsons et al. 2012b). Let us consider two baseline b_i and b_j of same length and orientation, such that the measured delay transforms are $\widetilde{V}_{b_i} = \widetilde{V}_{\rm S} + \widetilde{V}_{{\rm N}_i}$ and $\widetilde{V}_{b_j} = \widetilde{V}_{\rm S} + \widetilde{V}_{{\rm N}_j}$, respectively. The cross-spectrum is obtained as

$$P_{\rm cross} \propto \langle \widetilde{V}_{b_i}\widetilde{V}_{b_j}^* \rangle = \langle |\widetilde{V}_{\rm S}|^2 + \widetilde{V}_{\rm S}\widetilde{V}_{{\rm N}_i}^* + \widetilde{V}_{\rm S}^*\widetilde{V}_{{\rm N}_j} + \widetilde{V}_{{\rm N}_i}\widetilde{V}_{{\rm N}_j}^* \rangle \approx P_{\rm S} + \langle \widetilde{V}_{{\rm N}_i}\widetilde{V}_{{\rm N}_j}^* \rangle, \tag{4.14}$$

where the average is made on $N_b(N_b-1)/2$ terms, given N_b redundant baselines, with $j > i$

to ensure that only unique baselines are considered and auto-spectra are discarded[3]. The term $\langle \widetilde{V}_{\mathrm{N}_i} \widetilde{V}^*_{\mathrm{N}_j} \rangle$ averages to zero in the limit of an infinite ensemble average, i.e. the cross-spectrum is an unbiased estimator.

Thus, we can rewrite Eq. (3.24) as

$$P(k) = \langle \widetilde{V}_{b_i} \widetilde{V}^*_{b_j} \rangle \left(\frac{\lambda^2}{2k_{\mathrm{B}}} \right)^2 \left(\frac{D_c^2 \Delta D_c}{B_{\mathrm{eff}}} \right) \left(\frac{1}{\Omega B_{\mathrm{eff}}} \right), \tag{4.16}$$

where $\Omega \approx 1.70\,\mathrm{sr}$ is the solid angle subtended by the PAPER primary beam (Parsons et al. 2014). We substituted the bandwidth with an effective bandwidth as we included a window function $W(\nu)$ in the delay transform (e.g., Parsons et al. 2012a):

$$\widetilde{V}_b(\tau) = \int_B V_b(u, v, \nu) W(\nu)\, e^{-2\pi i \nu \tau}\, \mathrm{d}\nu, \tag{4.17}$$

where we took a Blackman-Harris window function (Blackman et al. 1960; Harris 1978). The purpose of introducing a window function is to further reduce foreground spectral leakage at high delays (Vedantham et al. 2012; Parsons et al. 2014; Ali et al. 2015; Kolopanis et al. 2019). This means that the effective width of each sub-band is no longer 10 MHz but

$$B_{\mathrm{eff}} = \int_B W(\nu)\, \mathrm{d}\nu \approx 3.6\,\mathrm{MHz}. \tag{4.18}$$

We validated our power spectrum methodology through a set of simple simulations. First, we simulated noiseless visibilities for 30 m baselines from a 380 Jy point source (Pictor A-like, Jacobs et al. 2013) at the phase center. We considered only the two days that, before re-phasing, had the phase center at the edges of the selected LST range (see §4.1.1), i.e. JD2456638 (RA = $5^{\mathrm{h}}19^{\mathrm{m}}46.37^{\mathrm{s}}$) and JD2456631 (RA = $5^{\mathrm{h}}32^{\mathrm{m}}26.44^{\mathrm{s}}$). This choice is driven by the fact that, in the re-phasing procedure, the maximum change in the uv-coverages and visibilities occurs in these two days, which are then the worst cases to test our method. If it is valid for them, we are sure that it is also valid for all intermediate days. Then, we added a noise realization drawn by a complex Gaussian distribution $\mathcal{CN}(0, \sigma_v)$, where σ_v are reported in Table 4.2, generating a data set of random noise with same shape and flags of our observed data. This is a fundamental difference from previous works, like that of Kolopanis et al. (2019), where σ_v is estimated assuming a system temperature model. In this Thesis, instead, we derived the noise level from data themselves, with no assumptions.

Power spectra per redshift bin and per baseline redundant group are then obtained in the following way:

1. visibilities for each baseline were coherently averaged within each snapshot and over days, in order to have one visibility per channel and baseline $[V_{b_i}(\nu, t) \to V_{b_i}(\nu)]$;
2. visibilities were delay transformed using the Fast Fourier Transforms (FFT) algorithm $[V_{b_i}(\nu) \to \widetilde{V}_{b_i}(\tau)]$;
3. auto-spectra and cross-spectra were computed per baseline pair (selected with the above explained criterion) within a redundant group $[\widetilde{V}_{b_i}(\tau) \to P_{b_i b_j}(k)$ with $j > i]$;
4. incoherent averaging of all the power spectra (i.e., over considered baselines pairs), in order to obtain one estimate per redshift bin and redundant group $(P_{b_i, b_j}(k) \to P_b(k))$.

---

[3] We want the power spectrum estimator to be a complex value, with both real and imaginary parts. Consider two complex number $X = a + ib$ and $Y = a' + ib'$, such that the average of their cross-products is

$$\frac{1}{2}(XY^* + YX^*) = \frac{1}{2}[aa' + bb' + i(ba' - ab') + a'a + b'b - i(a'b - b'a)] = aa' + bb'. \tag{4.15}$$

The imaginary part cancels out, resulting in a real number.

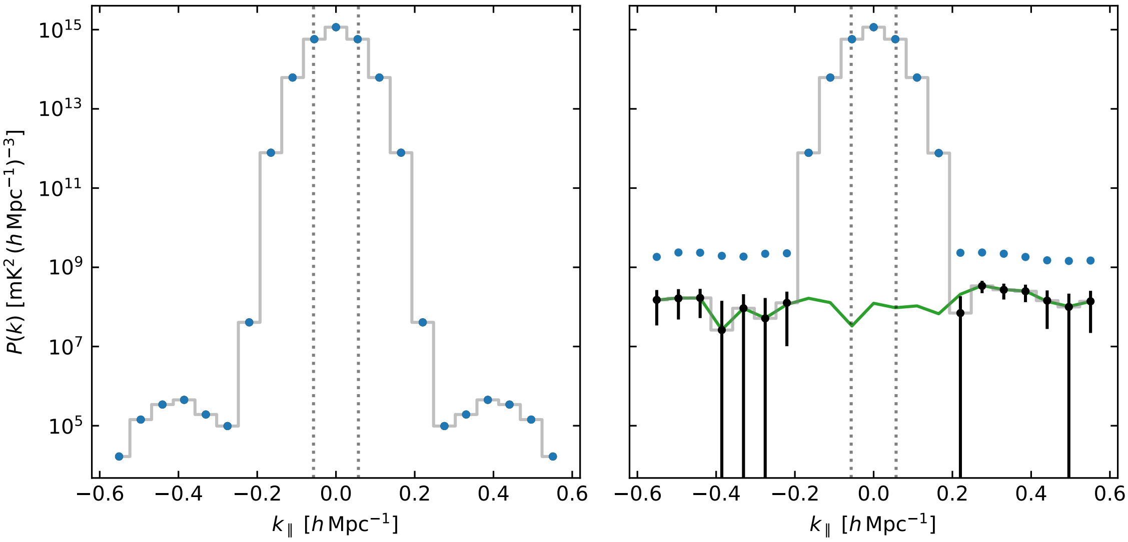

Figure 4.12 Simulated power spectrum at $z = 7.48$ (167.5 MHz) for 30 m baselines of the WE redundant group – see text for details. The vertical dotted lines denote the horizon limit for a 30 m baseline. The left panel shows the comparison between the auto-spectrum (blue dots) and the cross-spectrum (black dots, linked with gray line), obtained from Eq. (3.24) and Eq. (4.16), respectively, for the noiseless case. As expected, the two quantities correspond perfectly. This is no longer true in the right panel, where noise is included (green line). Error bars are twice the noise power averaged over the sampled $k_\parallel$.

The procedure is repeated for the simulations that included noise.

Figure 4.12 shows the resulting power spectra for the WE redundant group and the sub-band centered at 167.5 MHz, corresponding to $z = 7.48$ (similar results were obtained for the others baseline groups and sub-bands). The window function broadens the signal beyond the horizon limit: there is, however, a 10 orders of magnitude foreground suppression between the wedge and the EoR window ($|k_\parallel| > 0.2\,h\text{Mpc}^{-1}$). In absence of noise, the auto-spectrum (blue dots) coincides with the cross-spectrum (black dots, linked with the gray line). This is no longer true when noise is added to data, as shown in the right panel. As explained in §3.3.2, the power of a flat-spectrum source, such as the simulated one, is confined inside the wedge, where its power is five order of magnitude larger than the noise (i.e., SNR $\gg 1$). This is why auto-spectra and cross-spectra have the same value inside the foreground dominated region. At higher $\left|k_\parallel\right|$ the source power decreases and the noise power (green curve) dominates. In the regime of SNR $\ll 1$ the difference between the two estimators is clear: the auto-spectrum is higher than the cross-spectrum because of the noise bias which does not cancel out in the average. At $|k_\parallel| > 0.2\,h\,\text{Mpc}^{-1}$, instead, the cross-spectrum is fully compatible with noise, confirming that the cross-spectrum is an unbiased estimator. The error bars associated to the cross-spectrum data are calculated as twice the noise power averaged over the sampled $k_\parallel$. This is possible in simulations because the visibility noise corresponds exactly to the variance of the underlying distribution.

Finally, we combined cross-spectra of different redundant groups in order to obtain a single power spectrum estimate for each sub-bands [$P_b(k) \to P(k)$]. The results of this average are plotted in Figure 4.13, where all redshift bins are shown for completeness. In particular, the real and imaginary components were plotted separately. As the source is simulated at the phase center, the imaginary part of its visibilities should be zero. However, we note that the imaginary part is significantly different from zero inside the wedge. This seems to be due to the limited statistics that leads the cross terms in Eq. (4.14) not to cancel out completely. In particular, the remaining imaginary components are the product of signal and noise real parts.

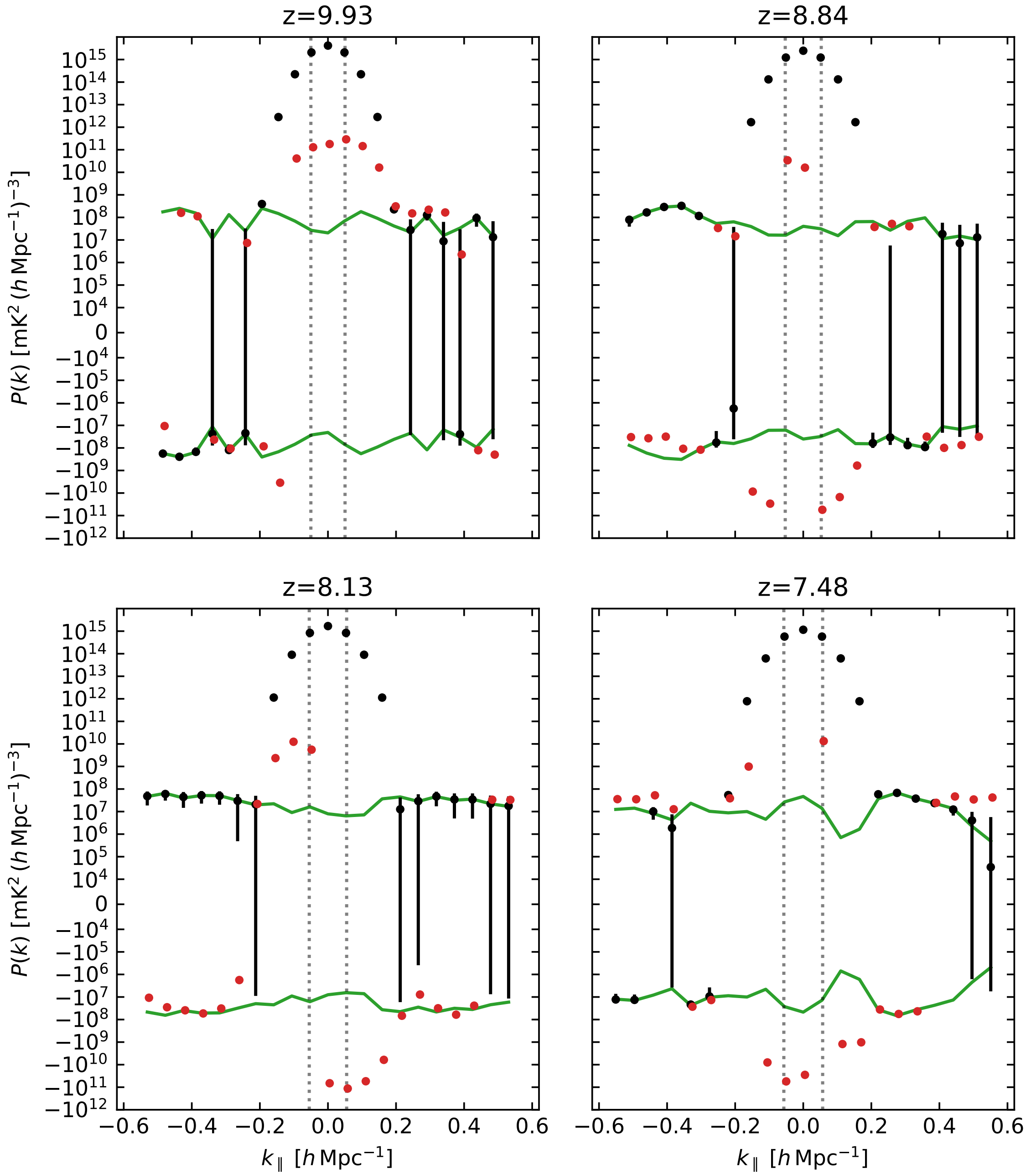

Figure 4.13 Real (black dots) and imaginary (red dots) parts of cross-spectra averaged over redundant groups. All four sub-bands are shown with the corresponding redshift. The green curve represents the real part of the noise power spectrum. Error bars are estimated as in Figure 4.12. The horizon limits are represented with vertical dotted lines. Note that inside and near the wedge the imaginary part of the power spectrum is higher than the noise, even if orders of magnitude lower than the real component.

Eventually, the power of the imaginary part is more than three orders of magnitude lower than the real part – i.e., $< 0.01\%$ of the real part –, and the power spectrum amplitude is not affected. Indeed, a comparison with Figure 4.12 immediately shows that the power spectrum amplitude has values similar to the real component. As expected, at $k_{\parallel} > 0.2\,h\,\mathrm{Mpc}^{-1}$ the two components are consistent with the noise level.

Chapter 5

Power spectrum results

In this chapter, we apply the power spectrum method outlined in §4.4.1 to our data. We derive upper limits on the 21 cm power spectrum that, in turn, we converted into lower limits on the IGM temperature during the Epoch of Reionization.

5.1 Multi-redshift power spectrum

Sky simulations described in §4.4.1 validate our power spectrum methodology. We then used Eq. (4.16) to calculate cross-products between 30 m baselines within the same redundant group. The resulting cross-spectra are then averaged in order to have one estimate per group and per redshift bin. These results are shown in Figure 5.1-5.4, where we plot both real (black dots) and imaginary (red dots) components of the power spectrum. The green line is a realization of the noise power, derived as described in §4.4.1.

The overall power spectrum behaviour is consistent across all the redundant groups – as one would qualitatively expect from the redundancy argument. Modes inside the horizon (i.e., $|k_{\parallel}| < 0.05\,h\,\mathrm{Mpc}^{-1}$) are dominated by foreground emission, although a significant foreground power bleeds outside the horizon, up to $|k_{\parallel}| \approx 0.2\,h\,\mathrm{Mpc}^{-1}$. At higher $|k_{\parallel}|$ values, the power spectrum starts flatten, which is the behaviours expected when thermal noise dominates – although features are present in a few cases. The foreground power spectrum is effectively suppressed by $6-7$ orders of magnitude outside the wedge. These results are in broad qualitative agreement with all the previously published results from PAPER observations (e.g., Parsons et al. 2014; Jacobs et al. 2015; Ali et al. 2015; Kolopanis et al. 2019).

We note two peculiar features of our results.

- The imaginary component of the power spectrum is fairly consistent with the real component at high k-modes. Within the wedge, however, the imaginary part remains significantly higher than the thermal noise power spectrum, whereas we would to cancel it out for redundant baselines. This may suggest that we are witnessing a (not unlikely) deviation from redundancy, as it was already suggested by Kolopanis et al. (2019). This means that nominally redundant baselines can be non-redundant (e.g., with slightly different antenna positions), introducing small differences in visibility phases, i.e. in the imaginary parts. However, we note that the imaginary component remains more than three orders of magnitude fainter than the real part everywhere in the wedge, not affecting the power spectrum amplitude.

- Cross-spectra at $z = 7.48$ (Figure 5.4) show a dip at $k_{\parallel} = 0$ (i.e., $\tau = 0$) and the average power inside the horizon is lower compared to other redundant groups. We do not have an obvious explanation for this effect, that requires further investigation. However, as the power spectrum wings are in agreement with other groups, we still retain EW and WE baselines for the following analysis.

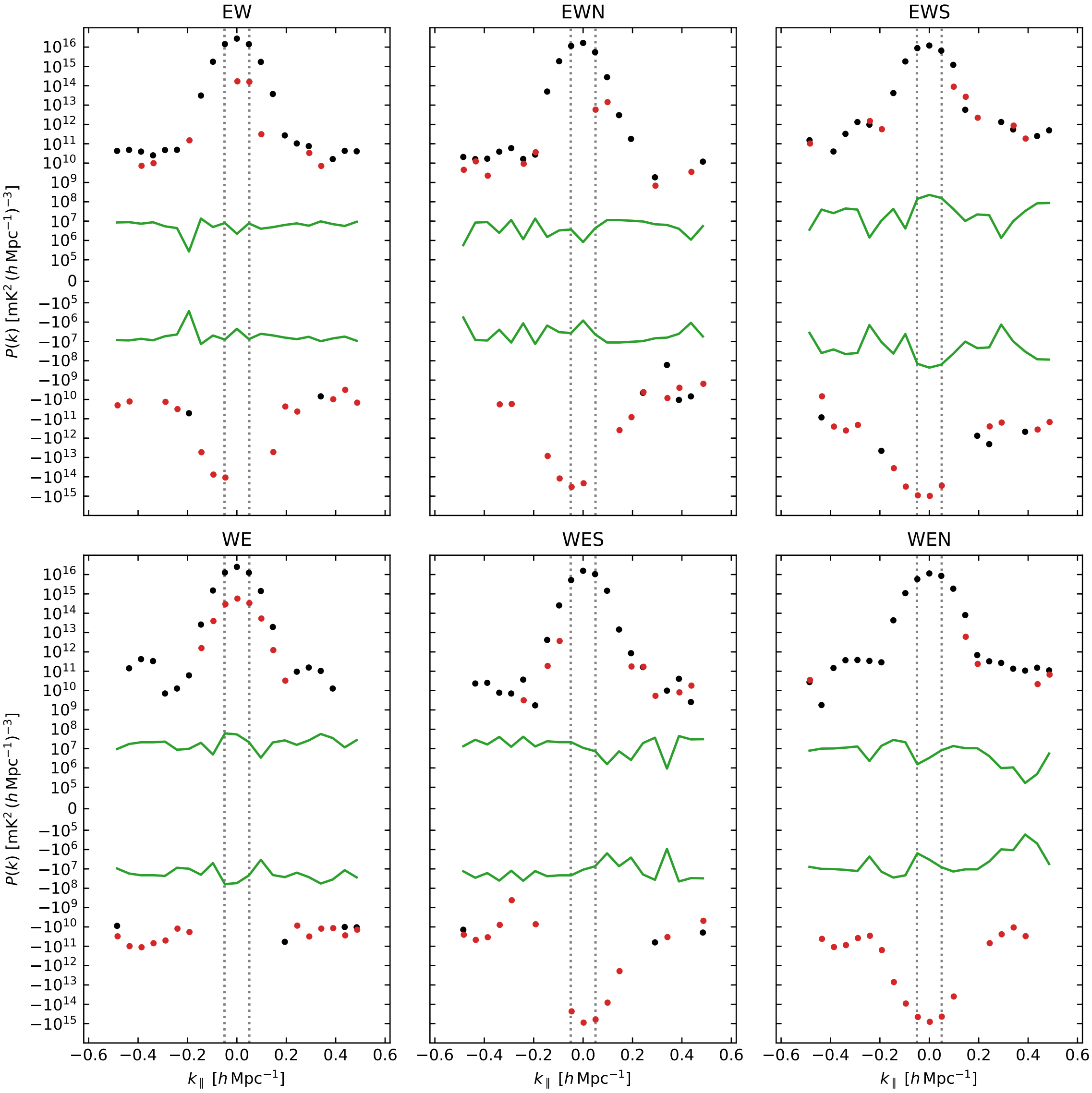

Figure 5.1 Cross-power spectra (Eq. 4.16) from our data at $z = 9.93$ (130.0 MHz) for all redundant groups of 30 m baselines. Real and imaginary components are denoted with black and red dots, respectively. The green line represents the noise power spectrum. Horizon limits are marked by vertical dotted lines.

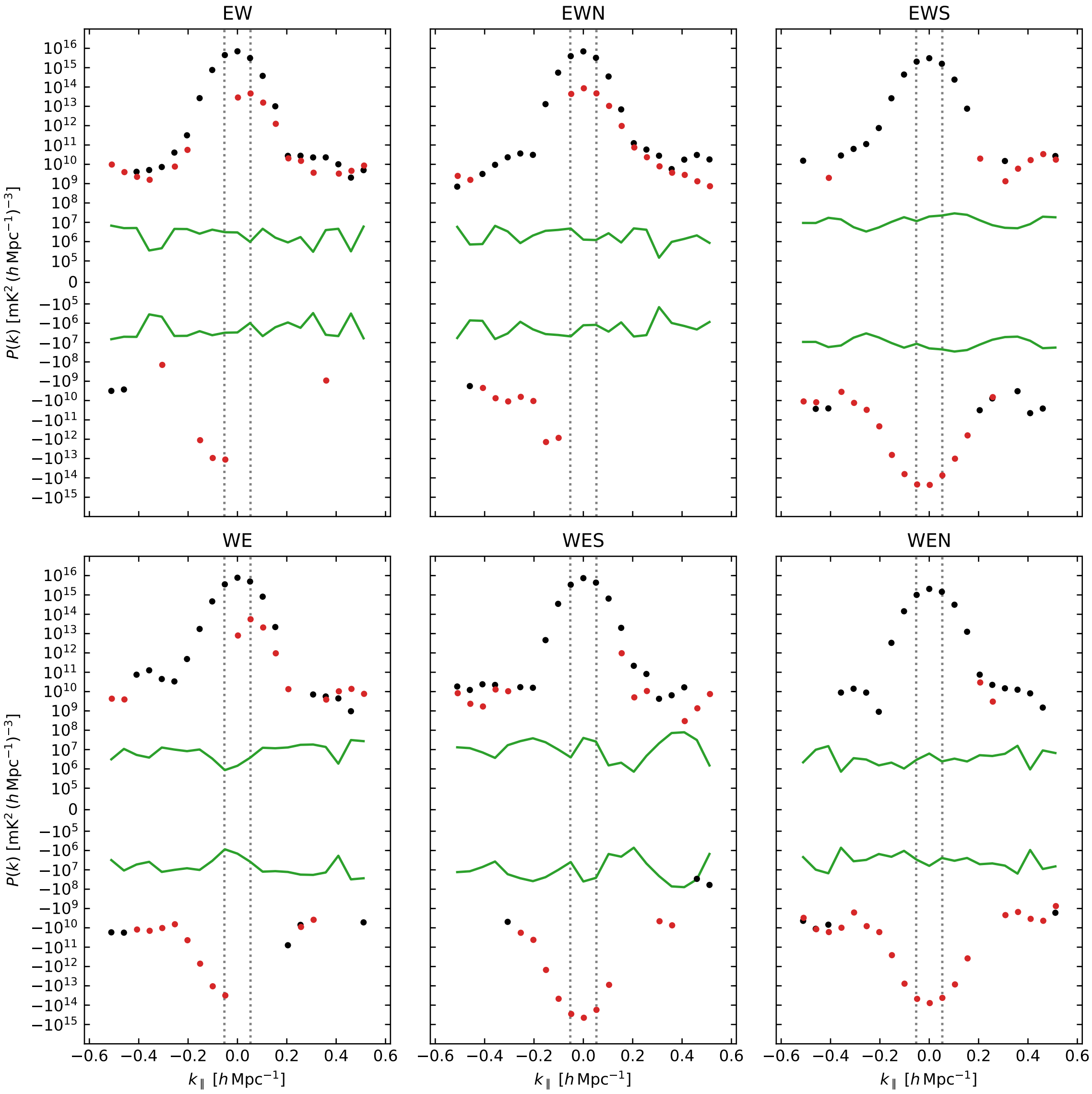

Figure 5.2 Same as Figure 5.1, but at $z = 8.84$ (144.3 MHz).

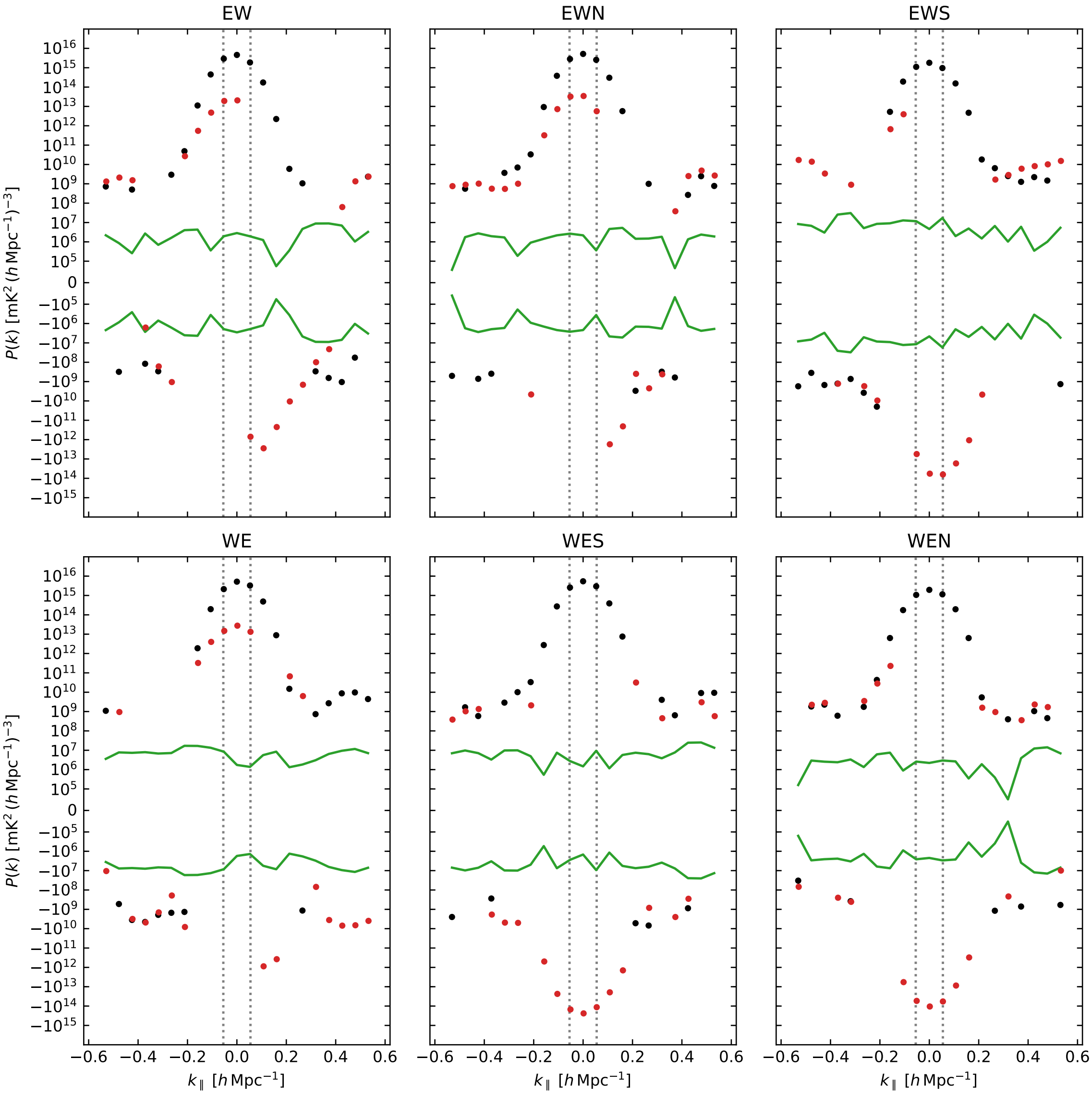

Figure 5.3 Same as Figure 5.1, but at $z = 8.13$ (155.6 MHz).

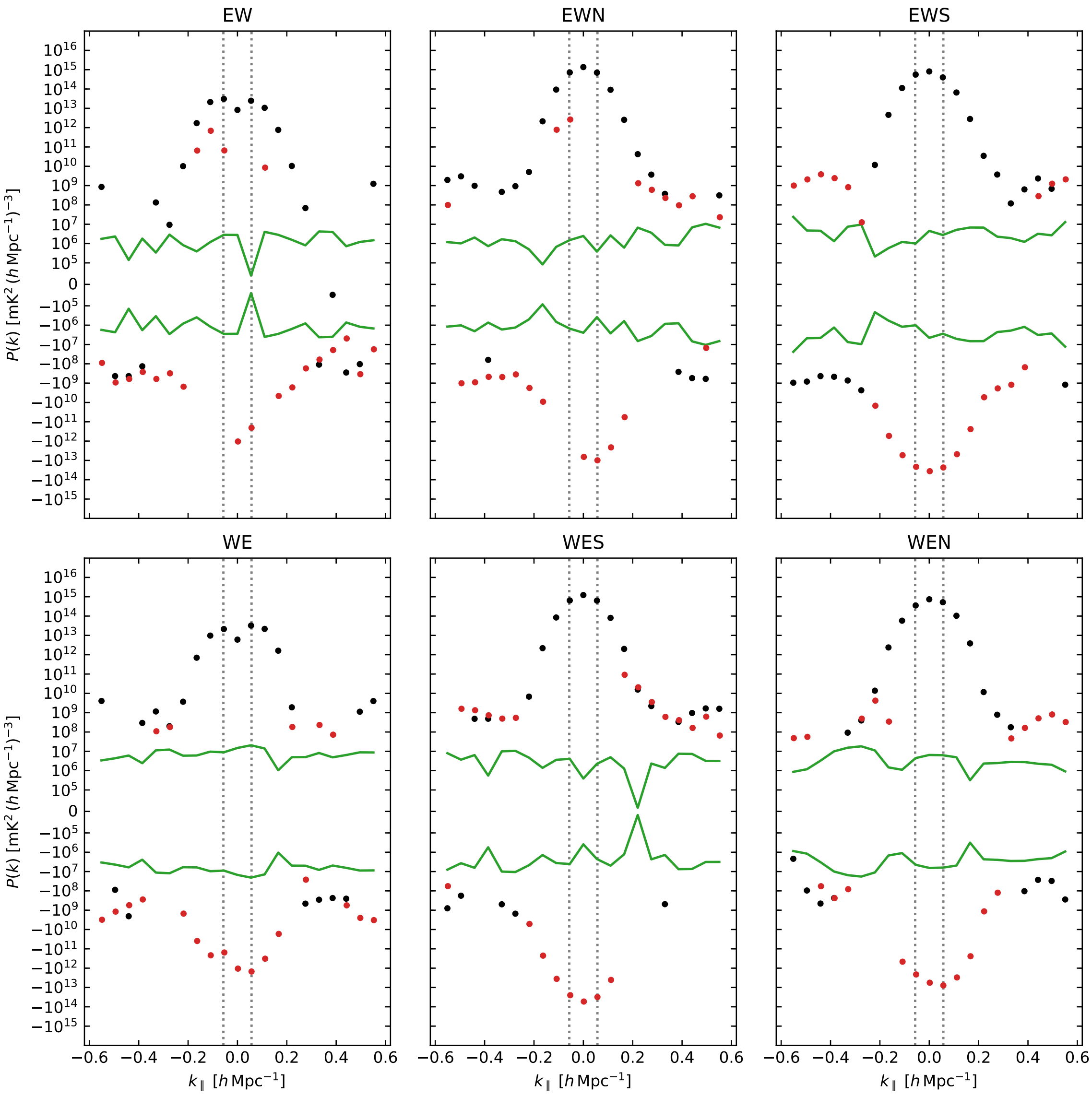

Figure 5.4 Same as Figure 5.1, but at $z = 7.48$ (167.5 MHz). Note that power spectra from EW and WE redundant groups have maximum power on horizons and a dip at $k_\parallel = 0$ (i.e., $\tau = 0$) – see text for details.

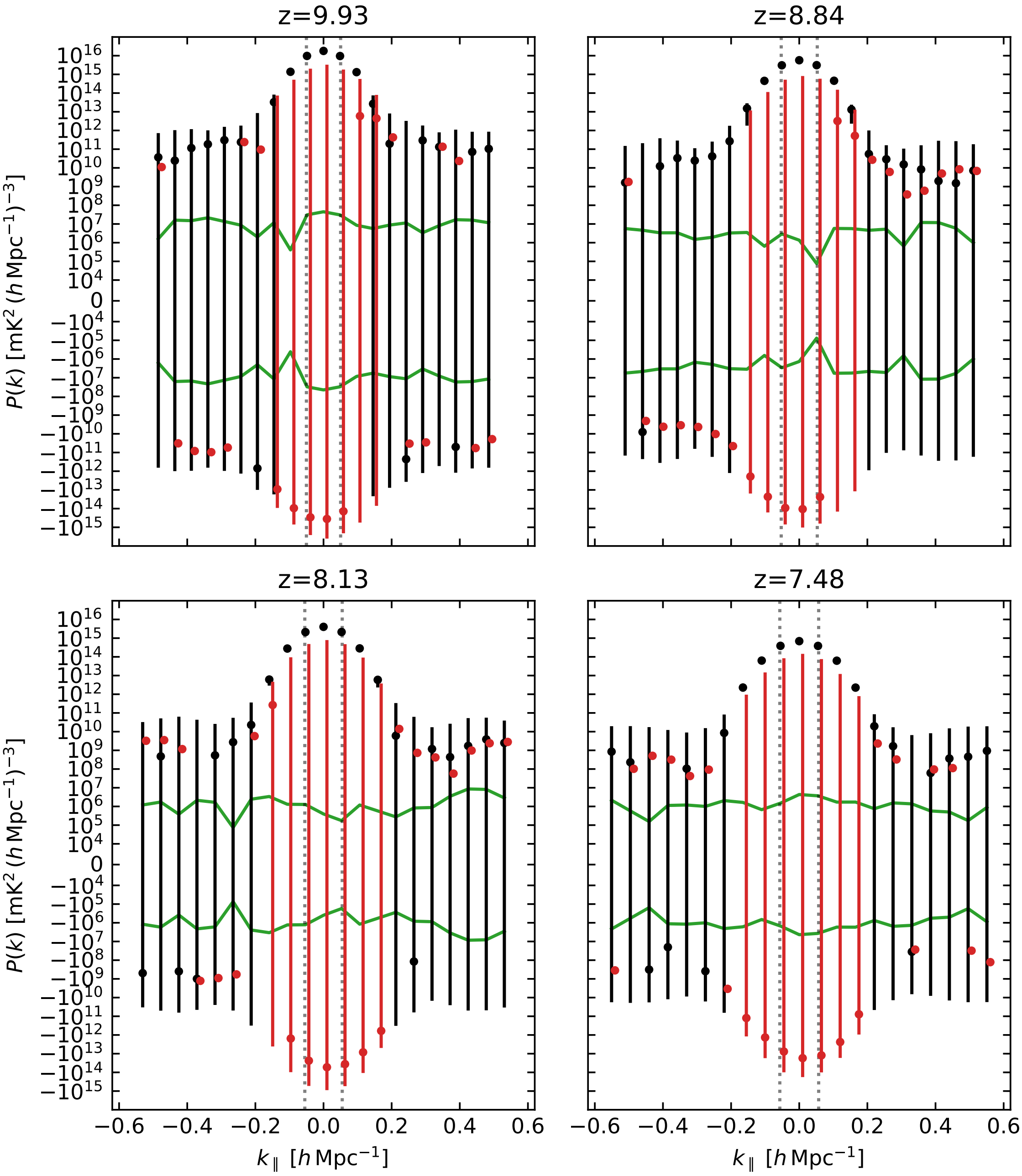

Figure 5.5 Final cross-power spectra obtained averaging over redundant groups within each sub-bands (same color scheme of Figure 5.1). Error bars at the 2σ confidence level for both real and imaginary parts (see text for more details). Errors of imaginary components are plotted for $|k_\parallel| < 0.2\, h\,\mathrm{Mpc}^{-1}$ only, for clarity. However, the imaginary component of the power spectrum is consistent with noise values at any k value. The uncertainty on the real part of the power spectrum is smaller than the dot size within the wedge.

Final power spectra for each sub-band were obtained by averaging cross-power spectra over the different redundant groups, resulting in one power spectrum per redshift bin (Figure 5.5).

Estimates of power spectrum errors bars are an active research field (i.e., Trott et al. 2016; Barry et al. 2019; Mertens et al. 2018; Morales et al. 2019). The pure thermal noise contribution to the uncertainties is estimated through our propagation method, resulting in the green line in Figure 5.5. We note, however, that both the real and imaginary parts of or power spectra remain systematically above the simulated noise level in each redshift bin. This suggests that some residual, systematic errors are present at high k-modes, most likely in the combined form of foreground leakage and calibration errors (e.g., Barry et al. 2016; Byrne et al. 2019). Taking into account the effect of calibration errors and systematic effects on power spectrum uncertainties is not trivial and, for example, Kolopanis et al. (2019) adopts a bootstrapping technique for the purpose of re-sampling the actual, underlying statistics of the data. Here we took a simplified approach and estimated error bars as the standard deviation of the distribution of cross-spectra within each redundant group (Figure 5.1-5.4). Thus, if δP_i is the power spectrum uncertainty (real or imaginary part) of the redundant group i, the uncertainty associated to the averaged cross-spectrum is given by

$$\delta\overline{P} = \frac{1}{N_{\mathrm{rg}}}\left[\sum_{i=1}^{N_{\mathrm{rg}}}(\delta P_i)^2\right]^{1/2}, \tag{5.1}$$

where $N_{\mathrm{rg}} = 6$ is the number of redundant groups for 30 m baselines. Both δP_i and $\delta\overline{P}$ are calculated for each $k_\parallel$ independently.

The broad features of the final power spectra are similar to what is seen in the individual groups – as expected. The overall power within the wedge increases with redshift (i.e., decreases with frequency), which is the expectation if it were due to synchrotron foreground. Outside the wedge, the power remains fairly flat, with a minimum at $z = 7.48$. The power spectrum in the EoR region ($|k_\parallel| > 0.2\,h\,\mathrm{Mpc}^{-1}$) remains systematically above the thermal noise expectations, but not inconsistent with it, given the relatively large error bars.

5.1.1 21 cm upper limits

The last step in our analysis is to compute the spherically averaged power spectrum. By invoking the isotropy argument (see §1.1), we first average the power spectrum over constant $|k_\parallel|$ values, operation known as *folding*, and then compute the dimensionless power spectrum using Eq. (2.22), with $k = \sqrt{k_\perp^2 + k_\parallel^2}$. We note that $k_\perp < 0.01\,h\,\mathrm{Mpc}^{-1}$ (Eq. 3.23) for all sub-bands and hence k is essentially given by $k_\parallel$. The amplitude power spectrum uncertainty is given by a combination of real and imaginary part errors:

$$\delta\Delta^2(k) = \frac{k^3}{2\pi^2 P}\sqrt{\mathrm{Re}\{P\}^2\,\mathrm{Re}\{\delta P\}^2 + \mathrm{Im}\{P\}^2\,\mathrm{Im}\{\delta P\}^2}, \tag{5.2}$$

where $P = P(k)$. Results are reported in Table 5.1 and plotted in Figure 5.6. The power spectrum within the horizon is a clear detection of foreground emission. However, even the power spectrum values up to $k = 0.2\,h\,\mathrm{Mpc}^{-1}$ are inconsistent with the noise power spectrum (apart from the $k = 0.15\,h\,\mathrm{Mpc}^{-1}$ value at $z = 9.93$ which is consistent with noise). We consider these points as detections of foreground power that bled outside the horizon limit. Conversely, we used the power spectrum values that are noise-compatible to set upper limits on the 21 cm signal,computed as $\Delta^2_{\mathrm{up}}(k) = \Delta^2(k) + 2\delta\Delta^2(k)$.

Current lowest upper limits (including the ones computed here) are reported in Figure 5.7. The best estimate per redshift bin from this Thesis work is at $k > 0.2\,h\,\mathrm{Mpc}^{-1}$, which is bold-faced in Table 5.1 and plotted as red square. Thus, we obtain $(35\,000\,\mathrm{mK})^2$, $(11\,000\,\mathrm{mK})^2$, $(51\,000\,\mathrm{mK})^2$ and $(3200\,\mathrm{mK})^2$ at $z = 9.93$, 8.84, 8.13 and 7.48, respectively.

Redshift	Frequency	k	$\Delta^2(k)$	$2\delta\Delta^2(k)$	$\Delta^2_{\mathrm{up}}(k)$
-	(MHz)	($h\,\mathrm{Mpc}^{-1}$)	(mK^2)	(mK^2)	(mK^2)
9.93	130.0	0.01	$5.6 \cdot 10^{8}$	$9.7 \cdot 10^{7}$	-
		0.05	$5.8 \cdot 10^{10}$	$8.2 \cdot 10^{9}$	-
		0.10	$6.3 \cdot 10^{10}$	$1.4 \cdot 10^{10}$	-
		0.15	$4.7 \cdot 10^{9}$	$5.5 \cdot 10^{9}$	$1.0 \cdot 10^{10}$
		0.19	$1.4 \cdot 10^{8}$	$2.2 \cdot 10^{9}$	$2.3 \cdot 10^{9}$
		0.24	$7.5 \cdot 10^{7}$	$1.1 \cdot 10^{9}$	$\mathbf{1.2 \cdot 10^{9}}$
		0.29	$3.8 \cdot 10^{8}$	$1.2 \cdot 10^{9}$	$1.6 \cdot 10^{9}$
		0.34	$3.2 \cdot 10^{8}$	$1.0 \cdot 10^{9}$	$1.3 \cdot 10^{9}$
		0.39	$1.3 \cdot 10^{8}$	$2.1 \cdot 10^{9}$	$2.2 \cdot 10^{9}$
		0.44	$2.8 \cdot 10^{8}$	$2.6 \cdot 10^{9}$	$2.9 \cdot 10^{9}$
		0.49	$4.1 \cdot 10^{8}$	$2.9 \cdot 10^{9}$	$3.4 \cdot 10^{9}$
8.84	144.3	0.01	$2.6 \cdot 10^{8}$	$4.1 \cdot 10^{7}$	-
		0.05	$2.2 \cdot 10^{10}$	$2.8 \cdot 10^{9}$	-
		0.10	$2.5 \cdot 10^{10}$	$4.9 \cdot 10^{9}$	-
		0.15	$2.6 \cdot 10^{9}$	$1.6 \cdot 10^{9}$	-
		0.20	$7.0 \cdot 10^{7}$	$3.9 \cdot 10^{8}$	$4.6 \cdot 10^{8}$
		0.26	$3.0 \cdot 10^{7}$	$1.1 \cdot 10^{8}$	$1.4 \cdot 10^{8}$
		0.31	$2.9 \cdot 10^{7}$	$9.3 \cdot 10^{7}$	$\mathbf{1.2 \cdot 10^{8}}$
		0.36	$4.8 \cdot 10^{7}$	$3.4 \cdot 10^{8}$	$3.9 \cdot 10^{8}$
		0.41	$2.5 \cdot 10^{7}$	$8.0 \cdot 10^{8}$	$8.3 \cdot 10^{8}$
		0.46	$2.2 \cdot 10^{7}$	$7.7 \cdot 10^{8}$	$8.0 \cdot 10^{8}$
		0.51	$4.2 \cdot 10^{7}$	$7.5 \cdot 10^{8}$	$8.0 \cdot 10^{8}$
8.13	155.6	0.01	$2.5 \cdot 10^{8}$	$4.2 \cdot 10^{7}$	-
		0.05	$1.7 \cdot 10^{10}$	$2.2 \cdot 10^{9}$	-
		0.11	$1.7 \cdot 10^{10}$	$2.9 \cdot 10^{9}$	-
		0.16	$1.2 \cdot 10^{9}$	$4.9 \cdot 10^{8}$	-
		0.21	$8.5 \cdot 10^{6}$	$1.2 \cdot 10^{8}$	$1.2 \cdot 10^{8}$
		0.27	$1.2 \cdot 10^{6}$	$3.8 \cdot 10^{7}$	$4.0 \cdot 10^{7}$
		0.32	$1.5 \cdot 10^{6}$	$2.4 \cdot 10^{7}$	$\mathbf{2.6 \cdot 10^{7}}$
		0.37	$1.7 \cdot 10^{6}$	$6.4 \cdot 10^{7}$	$6.6 \cdot 10^{7}$
		0.42	$4.9 \cdot 10^{6}$	$1.6 \cdot 10^{8}$	$1.6 \cdot 10^{8}$
		0.48	$2.0 \cdot 10^{7}$	$2.0 \cdot 10^{8}$	$2.2 \cdot 10^{8}$
		0.53	$2.4 \cdot 10^{7}$	$2.0 \cdot 10^{8}$	$2.3 \cdot 10^{8}$
7.48	167.5	0.01	$5.6 \cdot 10^{7}$	$8.4 \cdot 10^{6}$	-
		0.06	$3.5 \cdot 10^{9}$	$3.7 \cdot 10^{8}$	-
		0.11	$4.3 \cdot 10^{9}$	$5.2 \cdot 10^{8}$	-
		0.17	$5.2 \cdot 10^{8}$	$1.4 \cdot 10^{8}$	-
		0.22	$7.6 \cdot 10^{6}$	$2.7 \cdot 10^{7}$	$3.4 \cdot 10^{7}$
		0.28	$7.2 \cdot 10^{5}$	$1.2 \cdot 10^{7}$	$1.2 \cdot 10^{7}$
		0.33	$6.5 \cdot 10^{4}$	$1.0 \cdot 10^{7}$	$\mathbf{1.0 \cdot 10^{7}}$
		0.39	$6.0 \cdot 10^{5}$	$2.7 \cdot 10^{7}$	$2.7 \cdot 10^{7}$
		0.44	$1.4 \cdot 10^{6}$	$6.0 \cdot 10^{7}$	$6.1 \cdot 10^{7}$
		0.50	$2.1 \cdot 10^{6}$	$8.2 \cdot 10^{7}$	$8.4 \cdot 10^{7}$
		0.55	$7.9 \cdot 10^{6}$	$1.1 \cdot 10^{8}$	$1.2 \cdot 10^{8}$

Table 5.1 Dimensionless power spectra and 2σ error bars per redshift bin and per k-mode. For the sake of completeness, we report also the central frequencies of the four sub-bands. When the error is larger than the expected value, we also include upper limits Δ^2_{up} in the last column. The most sensitive limit for $k > 0.2\,h\,\mathrm{Mpc}^{-1}$, where foreground leakage should be zero, is bold-faced, as the corresponding k value.

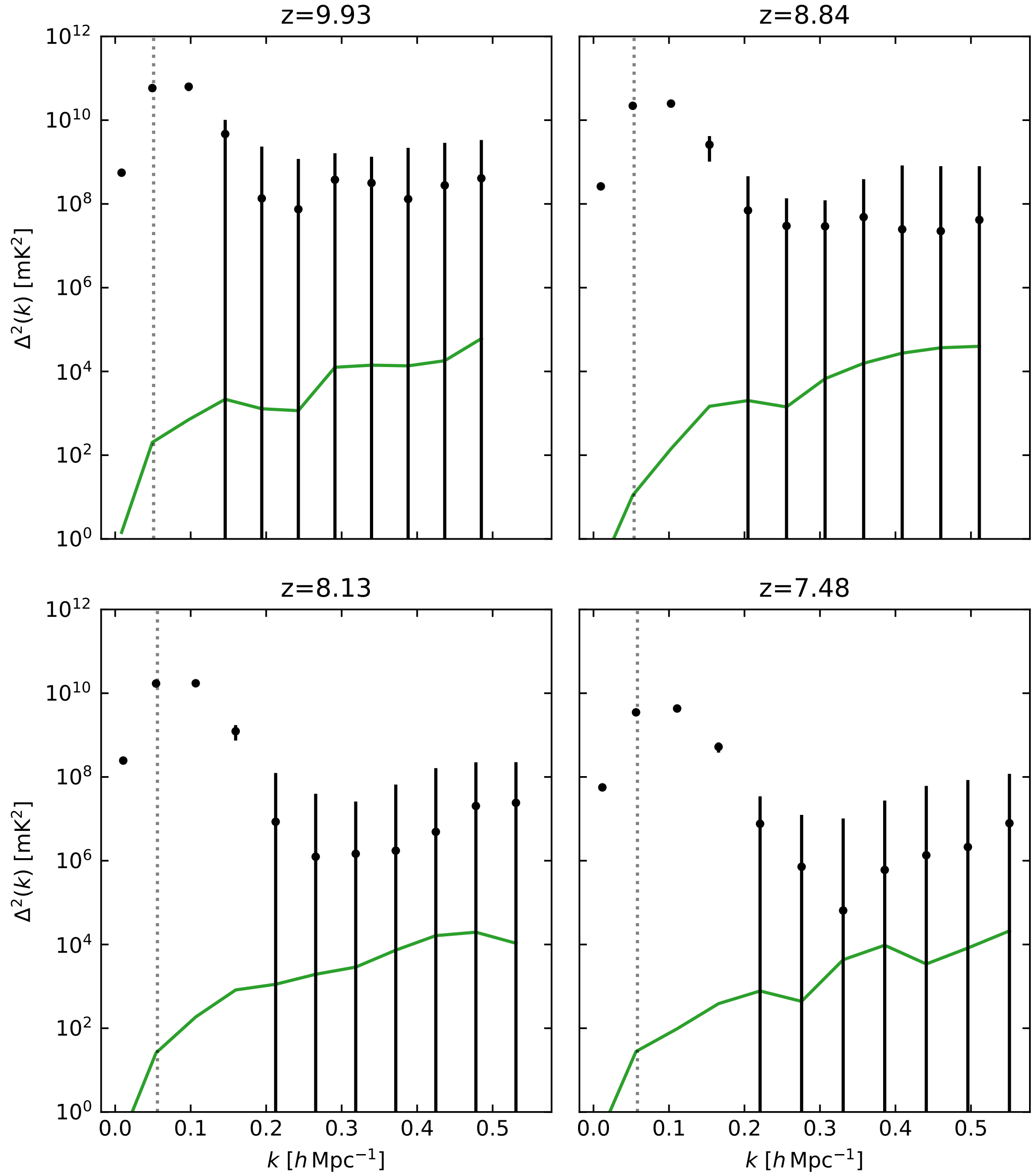

Figure 5.6 Dimensionless power spectra (Eq. 2.22) and 2σ error bars for each redshift bin in our observations (values in Table 5.1). The green line is the simulated thermal noise power spectrum. The horizon limit is denoted by the vertical dotted line.

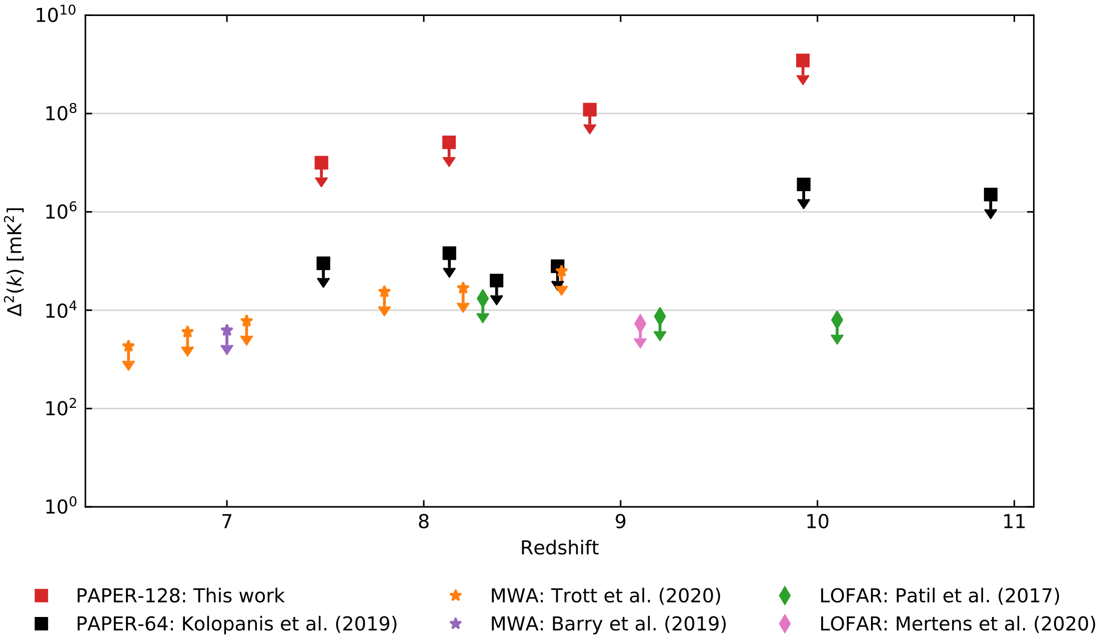

Figure 5.7 Comparison amongst current upper limits on the 21 cm power spectrum from different observations. Results from this Thesis are reported as red squares (bold-faced values of Table 5.1). Other upper limits are the best estimates from PAPER-64 (black squares; Kolopanis et al. 2019), MWA (stars; Trott et al. 2020; Barry et al. 2019) and LOFAR (diamonds; Patil et al. 2017; Mertens et al. 2020).

In the same figure, current upper limits on the 21 cm power spectrum from different observations are reported. In particular, consider the estimates from Kolopanis et al. (2019), which are indeed the best values from the PAPER experiments, coming however from the 64-elements deployment. This means that they had a number of baselines available four times lower than ours. On the other hand, their upper limits come from a much longer observation than ours, about a factor 200. If we scaled down by the relative observing time, their results would be consistent (to first approximation) with ours. In other words, the complete analysis of the two seasons of PAPER-128 data could improve the upper limits from Kolopanis et al. (2019).

5.2 Spin temperature constraints

Although our upper limits on the 21 cm signal are high, we still go through the exercise of using them to constrain the model parameters space. The most important constrain from multi-redshift upper limits would likely be on the HI neutral fraction which, however, requires sensitivities at the few (mK)^2 level. Conversely, the most extreme models (i.e., with the brightest power spectrum) are the cold reionization scenarios, where the spin temperature is not saturated (see §2.3). Here we attempt to constrain this models.

We considered our best upper limit at $z = 7.48$ and, following Ali et al. (2015), used a simple, analytic model of the 21 cm emission. Using cosmological parameters from Planck Collaboration et al. (2018a), reported in Table 1.1, we can rewrite the 21 cm brightness temperature (Eq. 2.10) as

$$\delta T_b(z) \approx T_0(z) x_{\mathrm{HI}}(z)[1 + \delta(z)]\xi(z), \tag{5.3}$$

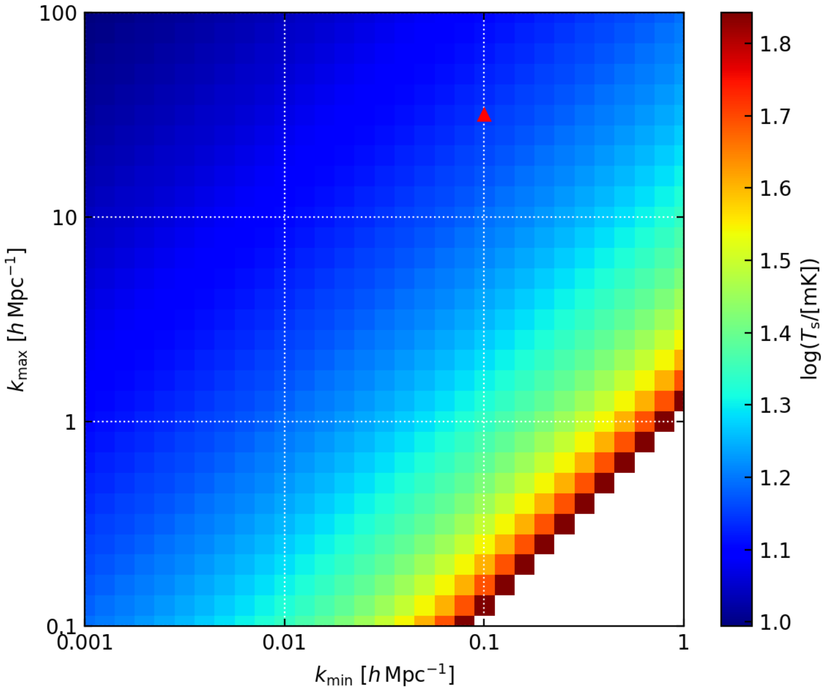

Figure 5.8 Constraints on the 21 cm spin temperature at $z = 7.48$ in the patchy reionization scenario (e.g., McQuinn et al. 2007). The red triangle corresponds to $k_{\rm min} = 0.1\,h\,{\rm Mpc}^{-1}$ and $k_{\rm max} = 30\,h\,{\rm Mpc}^{-1}$, which are representative scales in fiducial simulations (e.g., Zahn et al. 2007; Lidz et al. 2008).

where

$$T_0(z) \approx 27\left[\frac{1+z}{10}\right]^{1/2} {\rm mK} \quad ; \quad \xi(z) = 1 - \frac{T_\gamma(z)}{T_{\rm s}(z)}. \tag{5.4}$$

The maximum contrast between the spin temperature and CMB temperature happens if $T_{\rm s}$ is instantaneously coupled to $T_{\rm k}$ through the WF effect at $z \approx 30$ and when there are no sources that heat the IGM. In this case, the gas temperature keeps cooling adiabatically since decoupling, which occurs at $z_{\rm dec} \approx 200$. This assumption is obviously extreme and somewhat unrealistic, but is resembles the cold reionization scenario, where ionized regions are produced faster with respect to the hot reionization one (see Figure 2.3). With a negligible heating, we can assume the gas temperature spatially constant, so that ξ has no spatial dependency (Parsons et al. 2014). The dimensionless 21 cm power spectrum can therefore be written as

$$\Delta^2(k) = T_0^2 \xi^2(z) \Delta_i^2, \tag{5.5}$$

where $\Delta_i^2(k)$ is the dimensionless HI power spectrum. Assuming a patchy reionization model (e.g., McQuinn et al. 2007; Zahn et al. 2007), we have

$$\Delta_i^2(k) \equiv \frac{x_{\rm HI} - x_{\rm HI}^2}{\ln(k_{\rm max}/k_{\rm min})}, \tag{5.6}$$

where $k_{\rm min}$ and $k_{\rm max}$ are the minimum and maximum size of the ionized bubbles, respectively. Substituting in Eq. (5.5), we obtain an analytic model for the 21 cm power spectrum:

$$\Delta(k) = 730\left(1 - \frac{T_\gamma}{T_{\rm s}}\right)^2 \left(\frac{1+z}{10}\right)[]\frac{x_{\rm HI} - x_{\rm HI}^2}{\ln(k_{\rm max}/k_{\rm min})}]\,{\rm mK}^2. \tag{5.7}$$

If we replace the left hand side of Eq. (5.7) with our upper limit, we can derive a lower limit on the spin temperature as a function of the typical bubble sizes and the HI fraction.

Figure 5.8 shows the spin temperature constraints as a function of the k_{min} and k_{max}, assuming a neutral fraction $x_{\mathrm{HI}} \approx 0.3$ (Greig and Mesinger 2017). The most optimistic lower limit to the spin temperature is $T_{\mathrm{s}} = T_{\mathrm{k}} > 70\,\mathrm{mK}$. If we assume that the characteristic size of the ionized bubbles is between 0.03 and $10\,h^{-1}\,\mathrm{Mpc}$ (corresponding to $0.1 < k < 30\,h\,\mathrm{Mpc}^{-1}$) (Zahn et al. 2007; Lidz et al. 2008; Ghara et al. 2020), the spin temperature constraints weakens to $T_{\mathrm{s}} = T_{k} > 14\,\mathrm{mK}$.

Our upper limits are well within the range allowed by standard models. If we compute the gas temperature (Eq. 2.19) at $z = 7.48$ in the case of adiabatic cooling only, we find $T_{\mathrm{k}} = T_{\mathrm{s}} \approx 1\,\mathrm{K}$. In other words, our upper limits do not allow to significantly constrain the IGM temperature unless non standard physics is invoked (e.g., Barkana 2018; Fialkov and Barkana 2019).

Conclusion and future perspectives

In this Thesis work we analysed 5.5 hours of PAPER-128 data and estimated the 21 cm power spectra in four redshift intervals ($z = 7.48$, 8.13, 8.84 and 9.93). These results were obtained with custom developed Python scripts that average data over time, delay transform them and calculate cross-spectra of different 30 m baselines that are, in the end, averaged. Although this approach follows previous methods (e.g., Parsons et al. 2014; Kolopanis et al. 2019), we focused on an optimal data averaging and a simple approach that is free of possible signal losses (e.g., Cheng et al. 2018; Liu and Shaw 2019).

The delay transform is the basis of the foreground avoidance method that separates the Galactic and extragalactic foreground emission from the cosmological 21 cm signal. Indeed, foregrounds are confined to low k-modes due to their smooth spectra, therefore the EoR can be measured without foreground contamination at higher k-modes, in principle. In practice, current observations are still sensitivity limited at high k values.

We tested our methodology through sky and noise simulations, where the noise power was derived from the data themselves. This differs from previous works, such as Kolopanis et al. (2019), where a noise model was assumed.

We found power spectra dominated by foreground emission at $k < 0.2\,h\,\mathrm{Mpc}^{-1}$ and consistent with noise at $k > 0.2\,h\,\mathrm{Mpc}^{-1}$ at any redshift interval, from which we derived upper limits to the 21 cm power spectrum. Our lowest upper limits are $(35\,000\,\mathrm{mK})^2$, $(11\,000\,\mathrm{mK})^2$, $(51\,000\,\mathrm{mK})^2$ and $(3200\,\mathrm{mK})^2$ at $z = 9.93$, 8.84, 8.13 and 7.48, respectively.

We used our upper limit at $z = 7.48$ to estimate a lower limit on the IGM temperature. We assumed a simple, analytic model for the distribution of the ionized bubbles (McQuinn et al. 2007; Zahn et al. 2007), a fiducial $\overline{x}_{\mathrm{HI}} = 0.3$ (Greig and Mesinger 2017) and found that $T_{\mathrm{s}} = T_{\mathrm{k}} > 70\,\mathrm{mK}$.

The work presented can be extended in a few direction in the near future. It will be relatively straightforward to include the whole PAPER-128 observing season and to extend the analysis to include the 15 m baselines and both polarizations (i.e. XX and YY. In this way, our upper limits will become competitive with Kolopanis et al. (2019). Second, we noticed that our upper limits are broadly consistent with noise, but show a persistent power excess in the k range of interest. Future work will be dedicated to investigate this issue and its possible connection with foreground leakage and calibration errors. Alternative methods to estimate the power spectrum uncertainties will also be investigated as a cross check against the presence of systematic errors (e.g., Cheng et al. 2018). An increased sensitivity and solid control over systematic will allow us to place better constraints on the IGM temperature. Conversely, assuming complete gas heating before $z = 10$, we would be able to place initial constraints on the evolution of the IGM neutral fraction and, possibly, the characteristic size of the largest ionized regions (Zaroubi 2013; Ghara et al. 2020).

Next generation experiments will likely provide sufficient sensitivity to fully characterize the cosmic evolution of the IGM.

Bibliography

Ali, Z. S., et al. 2015. "PAPER-64 Constraints on Reionization: The 21 cm Power Spectrum at $z = 8.4$". *ApJ* 809 (1): 61. doi:10.1088/0004-637X/809/1/61.

Alpher, R. A., and R. C. Herman. 1949. "Remarks on the Evolution of the Expanding Universe". *Phys. Rev.* 75 (7): 1089–1095. doi:10.1103/PhysRev.75.1089.

Barkana, R. 2018. "Possible interaction between baryons and dark-matter particles revealed by the first stars". *Nature* 555 (7694): 71–74. doi:10.1038/nature25791.

Barkana, R., and A. Loeb. 2001. "In the beginning: the first sources of light and the reionization of the universe". *Phys. Rep.* 349 (2): 125–238. doi:10.1016/S0370-1573(01)00019-9.

— . 2007. "The physics and early history of the intergalactic medium". *Reports on Progress in Physics* 70 (4): 627–657. doi:10.1088/0034-4885/70/4/r02.

Barry, N., et al. 2016. "Calibration requirements for detecting the 21 cm epoch of reionization power spectrum and implications for the SKA". *MNRAS* 461 (3): 3135–3144. doi:10.1093/mnras/stw1380.

Barry, N., et al. 2019. "Improving the Epoch of Reionization Power Spectrum Results from Murchison Widefield Array Season 1 Observations". *ApJ* 884 (1): 1.

Beardsley, A. P., et al. 2016. "First Season MWA EoR Power spectrum Results at Redshift 7". *ApJ* 833 (1): 102. doi:10.3847/1538-4357/833/1/102.

Becker, R. H., et al. 2001. "Evidence for Reionization at z~6: Detection of a Gunn-Peterson Trough in a z=6.28 Quasar". *AJ* 122 (6): 2850–2857. doi:10.1086/324231.

Bennett, J., et al. 2009. *The essential cosmic perpective.* 6th Edition. Addison-Wesley.

Beringer, J., et al. 2012. "Review of Particle Physics". *Phys. Rev. D* 86 (1): 010001. doi:10.1103/PhysRevD.86.010001.

Bernardi, G. 2019. "21 cm observations: calibration, strategies, observables". *arXiv e-prints.* arXiv: 1909.11938.

Bernardi, G., M. McQuinn, and L. J. Greenhill. 2015. "Foreground Model and Antenna Calibration Errors in the Measurement of the Sky-averaged λ21 cm Signal at z~20". *ApJ* 799 (1): 90. doi:10.1088/0004-637X/799/1/90.

Bernardi, G., et al. 2013. "A 189 MHz, 2400 deg^2 Polarization Survey with the Murchison Widefield Array 32-element Prototype". *ApJ* 771 (2): 105. doi:10.1088/0004-637X/771/2/105.

Bernardi, G., et al. 2010. "Foregrounds for observations of the cosmological 21 cm line. II. Westerbork observations of the fields around 3C 196 and the North Celestial Pole". *A&A* 522:A67. doi:10.1051/0004-6361/200913420.

Blackman, R. B., J. W. Tukey, and T. Teichmann. 1960. "The Measurement of Power Spectra". *Physics Today* 13 (2): 52. doi:10.1063/1.3056826.

Bowman, J. D., M.l F. Morales, and J. N. Hewitt. 2009. “Foreground Contamination in Interferometric Measurements of the Redshifted 21 cm Power Spectrum”. *ApJ* 695 (1): 183–199. doi:10.1088/0004-637X/695/1/183.

Bowman, J. D., A. E. E. Rogers, and J. N. Hewitt. 2008. “Toward Empirical Constraints on the Global Redshifted 21 cm Brightness Temperature During the Epoch of Reionization”. *ApJ* 676 (1): 1–9. doi:10.1086/528675.

Bowman, J. D., et al. 2018. “An absorption profile centred at 78 megahertz in the sky-averaged spectrum”. *Nature* 555 (7694): 67–70. doi:10.1038/nature25792.

Brandenburg, A., and K. Subramanian. 2007. “Simulations of the anisotropic kinetic and magnetic alpha effects”. *Astronomische Nachrichten* 328 (6): 507. doi:10.1002/asna.200710772.

Buote, D. A., and C. R. Canizares. 1994. “Geometrical Evidence for Dark Matter: X-Ray Constraints on the Mass of the Elliptical Galaxy NGC 720”. *ApJ* 427:86. doi:10.1086/174123.

Buras, A. J., et al. 1978. “Aspects of the grand unification of strong, weak and electromagnetic interactions”. *Nucl. Phys. B* 135:66–92. doi:10.1016/0550-3213(78)90214-6.

Byrne, R., et al. 2019. “Fundamental Limitations on the Calibration of Redundant 21 cm Cosmology Instruments and Implications for HERA and the SKA”. *ApJ* 875 (1): 70. doi:10.3847/1538-4357/ab107d.

Callingham, J. R., et al. 2017. “Extragalactic Peaked-spectrum Radio Sources at Low Frequencies”. *ApJ* 836 (2): 174. doi:10.3847/1538-4357/836/2/174.

Carilli, C. L. 2017. *HERA Memo 60: System Noise from LST Differencing.* http://reionization.org/science/memos/.

Carroll, P. A., et al. 2016. “A high reliability survey of discrete Epoch of Reionization foreground sources in the MWA EoR0 field”. *MNRAS* 461 (4): 4151–4175. doi:10.1093/mnras/stw1599.

Chapman, E., and V. Jelić. 2019. “Foregrounds and their mitigation”. *arXiv e-prints.* arXiv: 1909.12369.

Chapman, E., et al. 2014. “The Effect of Foreground Mitigation Strategy on EoR Window Recovery”. *arXiv e-prints.* arXiv: 1408.4695.

Cheng, C., et al. 2018. “Characterizing Signal Loss in the 21 cm Reionization Power Spectrum: A Revised Study of PAPER-64”. *ApJ* 868 (1): 26. doi:10.3847/1538-4357/aae833.

Cheung, K., et al. 2019. “The impact of EDGES 21-cm data on dark matter interactions”. *Physics Letters B* 789:137–144. doi:10.1016/j.physletb.2018.11.058.

Ciardi, B., and A. Ferrara. 2005. “The First Cosmic Structures and Their Effects”. *Space Sci. Rev.* 116 (3): 625–705. doi:10.1007/s11214-005-3592-0.

Ciardi, B, and P Madau. 2003. “Probing beyond the Epoch of Hydrogen Reionization with 21 Centimeter Radiation”. *ApJ* 596 (1): 1–8. doi:10.1086/377634.

Clark, B. G. 1980. “An efficient implementation of the algorithm ’CLEAN’”. *A&A* 89 (3): 377.

Cohen, A., et al. 2017. “Charting the parameter space of the global 21-cm signal”. *MNRAS* 472 (2): 1915–1931. doi:10.1093/mnras/stx2065.

Coles, P., and F. Lucchin. 2002. *Cosmology: The Origin and Evolution of Cosmic Structure.* 2nd Edition. Wiley & Sons, Ltd.

Croft, R. A. C. 1998. “Characterization of Lyman Alpha Spectra and Predictions of Structure Formation Models: A Flux Statistics Approach”. In *Eighteenth Texas Symposium on Relativistic Astrophysics*, ed. by A. V. Olinto, J. A. Frieman, and D. N. Schramm, 664. arXiv: astro-ph/9701166.

Datta, A., J. D. Bowman, and C. L. Carilli. 2010. "Bright Source Subtraction Requirements for Redshifted 21 cm Measurements". *ApJ* 724 (1): 526–538. doi:10.1088/0004-637X/724/1/526.

DeBoer, D. R., et al. 2017. "Hydrogen Epoch of Reionization Array (HERA)". *PASP* 129 (974): 045001. doi:10.1088/1538-3873/129/974/045001.

Di Matteo, T., et al. 2002. "Radio Foregrounds for the 21 Centimeter Tomography of the Neutral Intergalactic Medium at High Redshifts". *ApJ* 564 (2): 576–580. doi:10.1086/324293.

Dicke, R. H., et al. 1965. "Cosmic Black-Body Radiation". *ApJ* 142:414–419. doi:10.1086/148306.

Dillon, J. S., A. Liu, and M. Tegmark. 2013. "A fast method for power spectrum and foreground analysis for 21 cm cosmology". *Phys. Rev. D* 87 (4): 043005. doi:10.1103/PhysRevD.87.043005.

Dillon, J. S., et al. 2015. "Empirical covariance modeling for 21 cm power spectrum estimation: A method demonstration and new limits from early Murchison Widefield Array 128-tile data". *Phys. Rev. D* 91 (12): 123011. doi:10.1103/PhysRevD.91.123011.

Dillon, J. S., et al. 2014. "Overcoming real-world obstacles in 21 cm power spectrum estimation: A method demonstration and results from early Murchison Widefield Array data". *Phys. Rev. D* 89 (2): 023002. doi:10.1103/PhysRevD.89.023002.

Eastwood, M. W., et al. 2019. "The 21 cm Power Spectrum from the Cosmic Dawn: First Results from the OVRO-LWA". *AJ* 158 (2): 84. doi:10.3847/1538-3881/ab2629.

Einstein, A. 1916. "Die Grundlage der allgemeinen Relativitätstheorie". *Annalen der Physik* 354 (7): 769–822. doi:10.1002/andp.19163540702.

— . 1917. "Kosmologische Betrachtungen zur allgemeinen Relativitätstheorie". *Sitzungsberichte der Königlich Preußischen Akademie der Wissenschaften (Berlin)*: 142–152.

Einstein, A., and W. de Sitter. 1932. "On the Relation between the Expansion and the Mean Density of the Universe". *Proceedings of the National Academy of Science* 18 (3): 213–214. doi:10.1073/pnas.18.3.213.

Evans, I. N., et al. 2010. "The Chandra Source Catalog". *ApJS* 189 (1): 37–82. doi:10.1088/0067-0049/189/1/37.

Ewall-Wice, A., et al. 2016. "First limits on the 21 cm power spectrum during the Epoch of X-ray heating". *MNRAS* 460 (4): 4320–4347. doi:10.1093/mnras/stw1022.

Faisst, A. L., et al. 2014. "Spectroscopic Observation of Lyα Emitters at z ~7.7 and Implications on Re-ionization". *ApJ* 788 (1): 87. doi:10.1088/0004-637X/788/1/87.

Fan, X., et al. 2006. "Constraining the Evolution of the Ionizing Background and the Epoch of Reionization with z~6 Quasars. II. A Sample of 19 Quasars". *AJ* 132 (1): 117–136. doi:10.1086/504836.

Fialkov, A., and R. Barkana. 2019. "Signature of excess radio background in the 21-cm global signal and power spectrum". *MNRAS* 486 (2): 1763–1773. doi:10.1093/mnras/stz873.

Fialkov, A., R. Barkana, and E. Visbal. 2014. "The observable signature of late heating of the Universe during cosmic reionization". *Nature* 506 (7487): 197–199. doi:10.1038/nature12999.

Field, G. B. 1958. "Excitation of the Hydrogen 21-CM Line". *Proceedings of the IRE* 46:240–250. doi:10.1109/JRPROC.1958.286741.

— . 1959. "The Spin Temperature of Intergalactic Neutral Hydrogen." *ApJ* 129:536. doi:10.1086/146653.

Fixsen, D. J. 2009. “The Temperature of the Cosmic Microwave Background”. *ApJ* 707 (2): 916–920. doi:`10.1088/0004-637x/707/2/916`.

Friedmann, A. 1922. “Über die Krümmung des Raumes”. *Zeitschrift fur Physik* 10:377–386. doi:`10.1007/BF01332580`.

Fuchs, B. 2001. “The Amount of Dark Matter in Spiral Galaxies”. In *Dark Matter in Astro- and Particle Physics*, ed. by H. V. Klapdor-Kleingrothaus, 25. arXiv: `astro-ph/0010358`.

Fuller, G. M., G. J. Mathews, and C. R. Alcock. 1988. “Quark-hadron phase transition in the early Universe: Isothermal baryon-number fluctuations and primordial nucleosynthesis”. *Phys. Rev. D* 37 (6): 1380–1400. doi:`10.1103/PhysRevD.37.1380`.

Furlanetto, S. R. 2016. “The 21-cm Line as a Probe of Reionization”. In *Understanding the Epoch of Cosmic Reionization: Challenges and Progress*, ed. by A. Mesinger, 423:247. doi:`10.1007/978-3-319-21957-8_9`.

Furlanetto, S. R., S. P. Oh, and F. H. Briggs. 2006. “Cosmology at low frequencies: The 21 cm transition and the high-redshift Universe”. *Phys. Rep.* 433 (4-6): 181–301. doi:`10.1016/j.physrep.2006.08.002`.

Furlanetto, S. R., M. Zaldarriaga, and L. Hernquist. 2004. “The Growth of H II Regions During Reionization”. *ApJ* 613 (1): 1–15. doi:`10.1086/423025`.

Gamow, G. 1946. “Expanding Universe and the Origin of Elements”. *Phys. Rev.* 70 (7-8): 572–573. doi:`10.1103/PhysRev.70.572.2`.

Gehlot, B. K., et al. 2019. “The first power spectrum limit on the 21-cm signal of neutral hydrogen during the Cosmic Dawn at z = 20-25 from LOFAR”. *MNRAS* 488 (3): 4271–4287. doi:`10.1093/mnras/stz1937`.

George, E. M., et al. 2015. “A Measurement of Secondary Cosmic Microwave Background Anisotropies from the 2500 Square-degree SPT-SZ Survey”. *ApJ* 799 (2): 177. doi:`10.1088/0004-637X/799/2/177`.

Ghara, R., et al. 2020. “Constraining the intergalactic medium at z ≈ 9.1 using LOFAR Epoch of Reionization observations”. *MNRAS*. doi:`10.1093/mnras/staa487`.

Giallongo, E., et al. 2015. “Faint AGNs at z > 4 in the CANDELS GOODS-S field: looking for contributors to the reionization of the Universe”. *A&A* 578:A83. doi:`10.1051/0004-6361/201425334`.

Greig, B., and A. Mesinger. 2017. “The global history of reionization”. *MNRAS* 465 (4): 4838–4852. doi:`10.1093/mnras/stw3026`.

Gunn, J. E., and B. A. Peterson. 1965. “On the Density of Neutral Hydrogen in Intergalactic Space.” *ApJ* 142:1633–1636. doi:`10.1086/148444`.

Guzmán, A. E., et al. 2011. “All-sky Galactic radiation at 45 MHz and spectral index between 45 and 408 MHz”. *A&A* 525:A138. doi:`10.1051/0004-6361/200913628`.

Hamaker, J. P., J. D. Bregman, and R. J. Sault. 1996. “Understanding radio polarimetry. I. Mathematical foundations.” *A&AS* 117:137–147.

Harker, G., et al. 2009. “Non-parametric foreground subtraction for 21-cm epoch of reionization experiments”. *MNRAS* 397 (2): 1138–1152. doi:`10.1111/j.1365-2966.2009.15081.x`.

Harris, F. J. 1978. “On the Use of Windows for Harmonic Analysis with the Discrete Fourier Transform”. *IEEE Proceedings* 66:51–83.

Harrison, E. R. 1970. “Fluctuations at the Threshold of Classical Cosmology”. *Phys. Rev. D* 1 (10): 2726–2730. doi:`10.1103/PhysRevD.1.2726`.

Haslam, C. G. T., et al. 1982. “A 408 MHz all-sky continuum survey. II. The atlas of contour maps.” *A&AS* 47:1–143.

Hassan, S., et al. 2018. “Constraining the contribution of active galactic nuclei to reionization”. *MNRAS* 473 (1): 227–240. doi:10.1093/mnras/stx2194.

Haverkorn, M. 2015. “Magnetic Fields in the Milky Way”. In *Magnetic Fields in Diffuse Media*, ed. by A. Lazarian, E. M. de Gouveia Dal Pino, and C. Melioli, 407:483. Astrophysics and Space Science Library. doi:10.1007/978-3-662-44625-6_17.

Heckman, T. M., and P. N. Best. 2014. “The Coevolution of Galaxies and Supermassive Black Holes: Insights from Surveys of the Contemporary Universe”. *ARA&A* 52:589–660. doi:10.1146/annurev-astro-081913-035722.

Hinshaw, G., et al. 2013. “Nine-year Wilkinson Microwave Anisotropy Probe (WMAP) Observations: Cosmological Parameter Results”. *ApJS* 208 (2): 19. doi:10.1088/0067-0049/208/2/19.

Högbom, J. A. 1974. “Aperture Synthesis with a Non-Regular Distribution of Interferometer Baselines”. *A&AS* 15:417.

Hubble, E. 1929. “A Relation between Distance and Radial Velocity among Extra-Galactic Nebulae”. *Proceedings of the National Academy of Science* 15 (3): 168–173. doi:10.1073/pnas.15.3.168.

Hurley-Walker, N., et al. 2017. “GaLactic and Extragalactic All-sky Murchison Widefield Array (GLEAM) survey - I. A low-frequency extragalactic catalogue”. *MNRAS* 464 (1): 1146–1167. doi:10.1093/mnras/stw2337.

Jacobs, D. C., et al. 2013. “A Flux Scale for Southern Hemisphere 21 cm Epoch of Reionization Experiments”. *ApJ* 776 (2): 108. doi:10.1088/0004-637X/776/2/108.

Jacobs, D. C., et al. 2015. “Multiredshift Limits on the 21 cm Power Spectrum from PAPER”. *ApJ* 801 (1): 51. doi:10.1088/0004-637X/801/1/51.

Jarvis, M. J., et al. 2010. “Herschel-ATLAS: the far-infrared-radio correlation at z < 0.5”. *MNRAS* 409 (1): 92–101. doi:10.1111/j.1365-2966.2010.17772.x.

Jelić, V., et al. 2008. “Foreground simulations for the LOFAR-epoch of reionization experiment”. *MNRAS* 389 (3): 1319–1335. doi:10.1111/j.1365-2966.2008.13634.x.

Johnson, R. C. 1993. *Antenna engineering handbook.*

Kaiser, N. 1987. “Clustering in real space and in redshift space”. *MNRAS* 227:1–21. doi:10.1093/mnras/227.1.1.

Kamionkowski, M. 2007. “Dark Matter and Dark Energy”. *arXiv e-prints.* arXiv: 0706.2986.

Kapahi, V. K., and S. Ananthakrishnan. 1995. “Astronomy with the Giant Metrewave Radio Telescope (GMRT)”. *Bulletin of the Astronomical Society of India* 23:265.

Kashikawa, N., et al. 2006. “The End of the Reionization Epoch Probed by Lyα Emitters at z = 6.5 in the Subaru Deep Field”. *ApJ* 648 (1): 7–22. doi:10.1086/504966.

Kellermann, K. I., and I. I. K. Pauliny-Toth. 1969. “The Spectra of Opaque Radio Sources”. *ApJ* 155:L71. doi:10.1086/180305.

Kellermann, K. I., et al. 1989. “VLA Observations of Objects in the Palomar Bright Quasar Survey”. *AJ* 98:1195. doi:10.1086/115207.

Kogut, A., et al. 2003. “First-Year Wilkinson Microwave Anisotropy Probe (WMAP) Observations: Temperature-Polarization Correlation”. *ApJS* 148 (1): 161–173. doi:10.1086/377219.

Kohn, S. A., and J. A. Aguirre. 2015. *Crosstalk measurements from PAPER-64*. http://reionization.org/wp-content/uploads/2015/01/xtalkmemo.pdf.

Kolopanis, M., et al. 2019. “A simplified, Lossless Reanalysis of PAPER-64”. *ApJ* 883 (2): 133. doi:10.3847/1538-4357/ab3e3a.

Konno, A., et al. 2014. "Accelerated Evolution of the Lyα Luminosity Function at z ~7 Revealed by the Subaru Ultra-deep Survey for Lyα Emitters at z = 7.3". *ApJ* 797 (1): 16. doi:10.1088/0004-637X/797/1/16.

Kormendy, J., and L. C. Ho. 2013. "Coevolution (Or Not) of Supermassive Black Holes and Host Galaxies". *ARA&A* 51 (1): 511–653. doi:10.1146/annurev-astro-082708-101811.

Kulkarni, G., et al. 2017. "Large 21-cm signals from AGN-dominated reionization". *MNRAS* 469 (4): 4283–4291. doi:10.1093/mnras/stx1167.

Landecker, T. L., and R. Wielebinski. 1970. "The Galactic Metre Wave Radiation: A two-frequency survey between declinations $+25^o$ and -25^o and the preparation of a map of the whole sky". *Australian Journal of Physics Astrophysical Supplement* 16:1.

Lemaître, G. 1927. "Un Univers homogène de masse constante et de rayon croissant rendant compte de la vitesse radiale des nébuleuses extra-galactiques". *Annales de la Société Scientifique de Bruxelles* 47:49–59.

Lewis, A. 2008. "Cosmological parameters from WMAP 5-year temperature maps". *Phys. Rev. D* 78 (2): 023002. doi:10.1103/PhysRevD.78.023002.

Li, R., et al. 2016. "Constraints on the identity of the dark matter from strong gravitational lenses". *MNRAS* 460 (1): 363–372. doi:10.1093/mnras/stw939.

Lidz, A., et al. 2008. "Detecting the Rise and Fall of 21 cm Fluctuations with the Murchison Widefield Array". *ApJ* 680 (2): 962–974. doi:10.1086/587618.

Lidz, A., et al. 2007. "Higher Order Contributions to the 21 cm Power Spectrum". *ApJ* 659 (2): 865–876. doi:10.1086/511670.

Linde, A. 2008. "Inflationary Cosmology". In *Inflationary Cosmology, Lecture Notes in Physics*, 738:1. Springer. doi:10.1007/978-3-540-74353-8_1.

Liu, A., A. R. Parsons, and C. M. Trott. 2014a. "Epoch of reionization window. I. Mathematical formalism". *Phys. Rev. D* 90 (2): 023018. doi:10.1103/PhysRevD.90.023018.

— . 2014b. "Epoch of reionization window. II. Statistical methods for foreground wedge reduction". *Phys. Rev. D* 90 (2): 023019. doi:10.1103/PhysRevD.90.023019.

Liu, A., and J. R. Shaw. 2019. "Data Analysis for Precision 21 cm Cosmology". *arXiv e-prints*. arXiv: 1907.08211.

Liu, A., and M. Tegmark. 2011. "A method for 21 cm power spectrum estimation in the presence of foregrounds". *Phys. Rev. D* 83 (10): 103006. doi:10.1103/PhysRevD.83.103006.

— . 2012. "How well can we measure and understand foregrounds with 21-cm experiments?" *MNRAS* 419 (4): 3491–3504. doi:10.1111/j.1365-2966.2011.19989.x.

Liu, A., et al. 2009. "An improved method for 21-cm foreground removal". *MNRAS* 398 (1): 401–406. doi:10.1111/j.1365-2966.2009.15156.x.

Loewenstein, M., and III White R. E. 1998. "Do elliptical galaxies have dark matter?" *Phys. Rep.* 307 (1): 75–81. doi:10.1016/S0370-1573(98)00059-3.

Madau, P., and F. Haardt. 2015. "Cosmic Reionization after Planck: Could Quasars Do It All?" *ApJ* 813 (1): L8. doi:10.1088/2041-8205/813/1/L8.

Madau, P., A. Meiksin, and M. J. Rees. 1997. "21 Centimeter Tomography of the Intergalactic Medium at High Redshift". *ApJ* 475 (2): 429–444. doi:10.1086/303549.

McGreer, I. D., A. Mesinger, and V. D'Odorico. 2015. "Model-independent evidence in favour of an end to reionization by z $\approx$ 6". *MNRAS* 447 (1): 499–505. doi:10.1093/mnras/stu2449.

McGreer, I. D., A Mesinger, and X. Fan. 2011. "The first (nearly) model-independent constraint on the neutral hydrogen fraction at z $\sim$ 6". *MNRAS* 415 (4): 3237–3246. doi:10.1111/j.1365-2966.2011.18935.x.

McNamara, B. J. 1971. "A Positional Determination of NP 0532". *PASP* 83 (494): 491. doi:`10.1086/129160`.

McQuinn, M., et al. 2006. "Cosmological Parameter Estimation Using 21 cm Radiation from the Epoch of Reionization". *ApJ* 653 (2): 815–834. doi:`10.1086/505167`.

McQuinn, M., et al. 2007. "Studying reionization with Lyα emitters". *MNRAS* 381 (1): 75–96. doi:`10.1111/j.1365-2966.2007.12085.x`.

Mellema, G., et al. 2013. "Reionization and the Cosmic Dawn with the Square Kilometre Array". *Experimental Astronomy* 36 (1-2): 235–318. doi:`10.1007/s10686-013-9334-5`.

Mertens, F. G., A. Ghosh, and L. V. E. Koopmans. 2018. "Statistical 21-cm signal separation via Gaussian Process Regression analysis". *MNRAS* 478 (3): 3640–3652. doi:`10.1093/mnras/sty1207`.

Mertens, F. G., et al. 2020. "Improved upper limits on the 21-cm signal power spectrum of neutral hydrogen at $\boldsymbol{z \approx 9.1}$ from LOFAR". *arXiv e-prints.* arXiv: `2002.07196`.

Mesinger, A., S. Furlanetto, and R. Cen. 2011. "21cmfast: a fast, seminumerical simulation of the high-redshift 21-cm signal". *MNRAS* 411 (2): 955–972. doi:`10.1111/j.1365-2966.2010.17731.x`.

Mesinger, A., B. Greig, and E. Sobacchi. 2016. "The Evolution Of 21 cm Structure (EOS): public, large-scale simulations of Cosmic Dawn and reionization". *MNRAS* 459 (3): 2342–2353. doi:`10.1093/mnras/stw831`.

Mesinger, A., et al. 2015. "Constraining the Astrophysics of the Cosmic Dawn and the Epoch of Reionization with the SKA". In *Advancing Astrophysics with the Square Kilometre Array (AASKA14)*, 11. arXiv: `1501.04106`.

Meszaros, P. 1974. "The behaviour of point masses in an expanding cosmological substratum." *A&A* 37 (2): 225–228.

Micheva, G., I. Iwata, and A. K. Inoue. 2017. "Lyman continuum leaking AGN in the SSA22 field". *MNRAS* 465 (1): 302–315. doi:`10.1093/mnras/stw1329`.

Mirocha, Jordan, and Steven R. Furlanetto. 2019. "What does the first highly redshifted 21-cm detection tell us about early galaxies?" *MNRAS* 483 (2): 1980–1992. doi:`10.1093/mnras/sty3260`.

Monsalve, R. A., et al. 2017. "Results from EDGES High-band. I. Constraints on Phenomenological Models for the Global 21 cm Signal". *ApJ* 847 (1): 64. doi:`10.3847/1538-4357/aa88d1`.

Moore, D. F., et al. 2017. "Limits on Polarized Leakage for the PAPER Epoch of Reionization Measurements at 126 and 164 MHz". *ApJ* 836 (2): 154. doi:`10.3847/1538-4357/836/2/154`.

Morales, M. F. 2005. "Power Spectrum Sensitivity and the Design of Epoch of Reionization Observatories". *ApJ* 619 (2): 678–683. doi:`10.1086/426730`.

Morales, M. F., J. D. Bowman, and J. N. Hewitt. 2006. "Improving Foreground Subtraction in Statistical Observations of 21 cm Emission from the Epoch of Reionization". *ApJ* 648 (2): 767–773. doi:`10.1086/506135`.

Morales, M. F., and J. Hewitt. 2004. "Toward Epoch of Reionization Measurements with Wide-Field Radio Observations". *ApJ* 615 (1): 7–18. doi:`10.1086/424437`.

Morales, M. F., et al. 2012. "Four Fundamental Foreground Power Spectrum Shapes for 21 cm Cosmology Observations". *ApJ* 752 (2): 137. doi:`10.1088/0004-637X/752/2/137`.

Morales, M. F., et al. 2019. "Understanding the diversity of 21 cm cosmology analyses". *MNRAS* 483 (2): 2207–2216. doi:`10.1093/mnras/sty2844`.

Mortlock, D. 2016. “Quasars as Probes of Cosmological Reionization”. In *Understanding the Epoch of Cosmic Reionization: Challenges and Progress*, ed. by A. Mesinger, 423:187. doi:10.1007/978-3-319-21957-8_7.

Mozdzen, T. J., et al. 2017. “Improved measurement of the spectral index of the diffuse radio background between 90 and 190 MHz”. *MNRAS* 464 (4): 4995–5002. doi:10.1093/mnras/stw2696.

Mukhanov, V. 2005. *Physical Foundations of Cosmology.* Cambridge University Press.

Murray, S. G., C. M. Trott, and C. H. Jordan. 2018. “A Clustered Extragalactic Foreground Model for the EoR”. In *Peering towards Cosmic Dawn*, ed. by Vibor Jelić and Thijs van der Hulst, 333:199–202. IAU Symposium. doi:10.1017/S174392131701119X.

— . 2017. “An Improved Statistical Point-source Foreground Model for the Epoch of Reionization”. *ApJ* 845 (1): 7. doi:10.3847/1538-4357/aa7d0a.

Natwariya, P. K., and J. R. Bhatt. 2020. “EDGES signal in presence of magnetic fields”. *arXiv e-prints.* arXiv: 2001.00194.

Nunhokee, C. D. 2018. “Observing cosmic reionization with PAPER: polarized foreground simulations and all sky images”. PhD thesis, Rhodes University, Grahamstown, South Africa. doi:http://hdl.handle.net/10962/68203.

O’Leary, R. M., and M. McQuinn. 2012. “The Formation of the First Cosmic Structures and the Physics of the $z \sim 20$ Universe”. *ApJ* 760 (1): 4. doi:10.1088/0004-637x/760/1/4.

Oesch, P. A., et al. 2016. “A Remarkably Luminous Galaxy at z=11.1 Measured with Hubble Space Telescope Grism Spectroscopy”. *ApJ* 819 (2): 129. doi:10.3847/0004-637X/819/2/129.

Ouchi, M., et al. 2010. “Statistics of 207 Lyα Emitters at a Redshift Near 7: Constraints on Reionization and Galaxy Formation Models”. *ApJ* 723 (1): 869–894. doi:10.1088/0004-637X/723/1/869.

Pacholczyk, A. G. 1970. “Infrared Variability of the Seyfert Galaxy NGC 1068”. *ApJ* 161:L207. doi:10.1086/180604.

Paciga, G., et al. 2013. “A simulation-calibrated limit on the H I power spectrum from the GMRT Epoch of Reionization experiment”. *MNRAS* 433 (1): 639–647. doi:10.1093/mnras/stt753.

Paciga, G., et al. 2011. “The GMRT Epoch of Reionization experiment: a new upper limit on the neutral hydrogen power spectrum at z$\approx$ 8.6”. *MNRAS* 413 (2): 1174–1183. doi:10.1111/j.1365-2966.2011.18208.x.

Parsons, A. R., and D. C. Backer. 2009. “Calibration of Low-Frequency, Wide-Field Radio Interferometers Using Delay/Delay-Rate Filtering”. *AJ* 138 (1): 219–226. doi:10.1088/0004-6256/138/1/219.

Parsons, A. R., et al. 2012a. “A Per-baseline, Delay-spectrum Technique for Accessing the 21 cm Cosmic Reionization Signature”. *ApJ* 756 (2): 165. doi:10.1088/0004-637X/756/2/165.

Parsons, A. R., et al. 2012b. “A Sensitivity and Array-configuration Study for Measuring the Power Spectrum of 21 cm Emission from Reionization”. *ApJ* 753 (1): 81. doi:10.1088/0004-637X/753/1/81.

Parsons, A. R., et al. 2014. “New Limits on 21 cm Epoch of Reionization from PAPER-32 Consistent with an X-Ray Heated Intergalactic Medium at z = 7.7”. *ApJ* 788 (2): 106. doi:10.1088/0004-637X/788/2/106.

Parsons, A. R., et al. 2010. “The Precision Array for Probing the Epoch of Re-ionization: Eight Station Results”. *AJ* 139 (4): 1468–1480. doi:10.1088/0004-6256/139/4/1468.

Patil, A. H., et al. 2017. “Upper Limits on the 21 cm Epoch of Reionization Power Spectrum from One Night with LOFAR”. *ApJ* 838 (1): 65. doi:10.3847/1538-4357/aa63e7.

Patra, N, et al. 2013. “SARAS: a precision system for measurement of the cosmic radio background and signatures from the epoch of reionization”. *Experimental Astronomy* 36 (1-2): 319–370. doi:10.1007/s10686-013-9336-3.

Peebles, P. J. E. 1968. “Recombination of the Primeval Plasma”. *ApJ* 153:1. doi:10.1086/149628.

Penzias, A. A., and R. W. Wilson. 1965. “A Measurement of Excess Antenna Temperature at 4080 Mc/s”. *ApJ* 142:419–421. doi:10.1086/148307.

Perlmutter, S., et al. 1999. “Measurements of Ω and Λ from 42 High-Redshift Supernovae”. *ApJ* 517 (2): 565–586. doi:10.1086/307221.

Philip, L., et al. 2019. “Probing Radio Intensity at High-Z from Marion: 2017 Instrument”. *Journal of Astronomical Instrumentation* 8 (2): 1950004. doi:10.1142/S2251171719500041.

Planck Collaboration et al. 2016a. “Planck 2015 results. XXV. Diffuse low-frequency Galactic foregrounds”. *A&A* 594:A25. doi:10.1051/0004-6361/201526803.

— . 2018a. “Planck 2018 results. I. Overview and the cosmological legacy of Planck”. *arXiv e-prints.* arXiv: 1807.06205.

— . 2018b. “Planck 2018 results. VI. Cosmological parameters”. *arXiv e-prints.* arXiv: 1807.06209.

— . 2019. “Planck 2018 results. VII. Isotropy and Statistics of the CMB”. *arXiv e-prints.* arXiv: 1906.02552.

— . 2018c. “Planck 2018 results. X. Constraints on inflation”. *arXiv e-prints.* arXiv: 1807.06211.

— . 2016b. “Planck intermediate results. XLVI. Reduction of large-scale systematic effects in HFI polarization maps and estimation of the reionization optical depth”. *A&A* 596:A107. doi:10.1051/0004-6361/201628890.

— . 2016c. “Planck intermediate results. XLVII. Planck constraints on reionization history”. *A&A* 596:A108. doi:10.1051/0004-6361/201628897.

Platania, P., et al. 1998. “A Determination of the Spectral Index of Galactic Synchrotron Emission in the 1-10 GHz Range”. *ApJ* 505 (2): 473–483. doi:10.1086/306175.

Pober, J. C., et al. 2013. “Opening the 21 cm Epoch of Reionization Window: Measurements of Foreground Isolation with PAPER”. *ApJ* 768 (2): L36. doi:10.1088/2041-8205/768/2/L36.

Prandoni, I. 2018. “EoR Foregrounds: the Faint Extragalactic Radio Sky”. In *Peering towards Cosmic Dawn*, ed. by Vibor Jelić and Thijs van der Hulst, 333:175–182. IAU Symposium. doi:10.1017/S174392131800073X.

Price, D. C., et al. 2018. “Design and characterization of the Large-aperture Experiment to Detect the Dark Age (LEDA) radiometer systems”. *MNRAS* 478 (3): 4193–4213. doi:10.1093/mnras/sty1244.

Pritchard, J. R., and S. R. Furlanetto. 2007. “21-cm fluctuations from inhomogeneous X-ray heating before reionization”. *MNRAS* 376 (4): 1680–1694. doi:10.1111/j.1365-2966.2007.11519.x.

— . 2006. “Descending from on high: Lyman-series cascades and spin-kinetic temperature coupling in the 21-cm line”. *MNRAS* 367 (3): 1057–1066. doi:10.1111/j.1365-2966.2006.10028.x.

Procopio, P., et al. 2017. “A High-Resolution Foreground Model for the MWA EoR1 Field: Model and Implications for EoR Power Spectrum Analysis”. *PASA* 34:e033. doi:10.1017/pasa.2017.26.

Rees, M. J. 1968. “Polarization and Spectrum of the Primeval Radiation in an Anisotropic Universe”. *ApJ* 153:L1. doi:10.1086/180208.

Reich, P., and W. Reich. 1988. “A map of spectral indices of the galactic radio continuum emission between 408 MHz and 1420 MHz for the entire northern sky.” *A&AS* 74:7–23.

Reichardt, C. L. 2016. “Observing the Epoch of Reionization with the Cosmic Microwave Background”. In *Understanding the Epoch of Cosmic Reionization: Challenges and Progress*, ed. by A. Mesinger, 423:227. doi:10.1007/978-3-319-21957-8_8.

Riess, A. G., et al. 2019. “Large Magellanic Cloud Cepheid Standards Provide a 1% Foundation for the Determination of the Hubble Constant and Stronger Evidence for Physics beyond ΛCDM”. *ApJ* 876 (1): 85. doi:10.3847/1538-4357/ab1422.

Robertson, B. E., et al. 2010. “Early star-forming galaxies and the reionization of the Universe”. *Nature* 468 (7320): 49–55. doi:10.1038/nature09527.

Rogers, A. E. E., and J. D. Bowman. 2008. “Spectral Index of the Diffuse Radio Background Measured from 100 to 200 MHz”. *AJ*, no. 2: 641–648. doi:10.1088/0004-6256/136/2/641.

Rybicki, G. B., and A. P. Lightman. 1979. *Radiative Processes in Astrophysics.* Wiley & Sons, Ltd.

Ryle, M., and A. Hewish. 1960. “The synthesis of large radio telescopes”. *MNRAS* 120:220. doi:10.1093/mnras/120.3.220.

Sakharov, A. D. 1967. “Violation of CP Invariance, C Asymmetry, and Baryon Asymmetry of the Universe”. *Soviet Journal of Experimental and Theoretical Physics Letters* 5:24.

Santos, M. G., A. Cooray, and L. Knox. 2005. “Multifrequency Analysis of 21 Centimeter Fluctuations from the Era of Reionization”. *ApJ* 625 (2): 575–587. doi:10.1086/429857.

Schmidt, M. 1965. “Large Redshifts of Five Quasi-Stellar Sources.” *ApJ* 141:1295. doi:10.1086/148217.

Shaposhnikov, M. E. 1987. “Baryon asymmetry of the universe in standard electroweak theory”. *Nucl. Phys. B* 287:757–775. doi:10.1016/0550-3213(87)90127-1.

Shaver, P. A., et al. 1999. “Can the reionization epoch be detected as a global signature in the cosmic background?” *A&A* 345:380–390.

Shaya, E. J., et al. 1996. “Hubble Space Telescope Planetary Camera Images of NGC 1316 (Fornax A)”. *AJ* 111:2212. doi:10.1086/117955.

Singh, S., and R. Subrahmanyan. 2019. “The Redshifted 21 cm Signal in the EDGES Low-band Spectrum”. *ApJ* 880 (1): 26. doi:10.3847/1538-4357/ab2879.

Singh, S., et al. 2017. “First Results on the Epoch of Reionization from First Light with SARAS 2”. *ApJ* 845 (2): L12. doi:10.3847/2041-8213/aa831b.

— . 2018. “SARAS 2 Constraints on Global 21 cm Signals from the Epoch of Reionization”. *ApJ* 858 (1): 54. doi:10.3847/1538-4357/aabae1.

Smirnov, O. M. 2011. “Revisiting the radio interferometer measurement equation. III. Addressing direction-dependent effects in 21 cm WSRT observations of 3C 147”. *A&A* 527:A108. doi:10.1051/0004-6361/201116435.

Songaila, A., and L. L. Cowie. 2002. “Approaching Reionization: The Evolution of the Ly α Forest from z=4 to z=6”. *AJ* 123 (5): 2183–2196. doi:10.1086/340079.

Springel, V., and L. Hernquist. 2003. “The history of star formation in a Λ cold dark matter universe”. *MNRAS* 339 (2): 312–334. doi:10.1046/j.1365-8711.2003.06207.x.

Strong, A. W., I. V. Moskalenko, and V. S. Ptuskin. 2007. "Cosmic-Ray Propagation and Interactions in the Galaxy". *Annual Review of Nuclear and Particle Science* 57 (1): 285–327. doi:10.1146/annurev.nucl.57.090506.123011.

Sunyaev, R. A., and Ia. B. Zeldovich. 1980. "The velocity of clusters of galaxies relative to the microwave background - The possibility of its measurement." *MNRAS* 190:413–420. doi:10.1093/mnras/190.3.413.

Sur, S., A. Brandenburg, and K. Subramanian. 2008. "Kinematic α-effect in isotropic turbulence simulations". *MNRAS* 385 (1): L15–L19. doi:10.1111/j.1745-3933.2008.00423.x.

Tegmark, M., et al. 2006. "Cosmological constraints from the SDSS luminous red galaxies". *Phys. Rev. D* 74 (12): 123507. doi:10.1103/PhysRevD.74.123507.

Thompson, A. R., J. M. Moran, and G. W. Jr. Swenson. 2017. *Interferometry and Synthesis in Radio Astronomy.* 3rd Edition. Springer.

Thyagarajan, N., et al. 2013. "A Study of Fundamental Limitations to Statistical Detection of Redshifted H I from the Epoch of Reionization". *ApJ* 776 (1): 6. doi:10.1088/0004-637X/776/1/6.

Thyagarajan, N., et al. 2015. "Foregrounds in Wide-field Redshifted 21 cm Power Spectra". *ApJ* 804 (1): 14. doi:10.1088/0004-637X/804/1/14.

Tilvi, V., et al. 2014. "Rapid Decline of Lyα Emission toward the Reionization Era". *ApJ* 794 (1): 5. doi:10.1088/0004-637X/794/1/5.

Tingay, S. J., et al. 2013. "The Murchison Widefield Array: The Square Kilometre Array Precursor at Low Radio Frequencies". *PASA* 30:e007. doi:10.1017/pasa.2012.007.

Trott, C. M., et al. 2016. "CHIPS: The Cosmological H I Power Spectrum Estimator". *ApJ* 818 (2): 139. doi:10.3847/0004-637X/818/2/139.

Trott, Ca. M., et al. 2020. "Deep multi-redshift limits on Epoch of Reionisation 21 cm Power Spectra from Four Seasons of Murchison Widefield Array Observations". *MNRAS*. doi:10.1093/mnras/staa414.

Urry, C. M., and P. Padovani. 1995. "Unified Schemes for Radio-Loud Active Galactic Nuclei". *PASP* 107:803. doi:10.1086/133630.

van Cittert, P. H. 1934. "Die Wahrscheinliche Schwingungsverteilung in Einer von Einer Lichtquelle Direkt Oder Mittels Einer Linse Beleuchteten Ebene". *Physica* 1 (1): 201–210. doi:10.1016/S0031-8914(34)90026-4.

van Haarlem, M. P., et al. 2013. "LOFAR: The LOw-Frequency ARray". *A&A* 556:A2. doi:10.1051/0004-6361/201220873.

Vedantham, H., N. Udaya Shankar, and R. Subrahmanyan. 2012. "Imaging the Epoch of Reionization: Limitations from Foreground Confusion and Imaging Algorithms". *ApJ* 745 (2): 176. doi:10.1088/0004-637X/745/2/176.

Venemans, B. P., et al. 2013. "Discovery of Three z > 6.5 Quasars in the VISTA Kilo-Degree Infrared Galaxy (VIKING) Survey". *ApJ* 779 (1): 24. doi:10.1088/0004-637X/779/1/24.

Wang, J., et al. 2013. "Exploring the Cosmic Reionization Epoch in Frequency Space: An Improved Approach to Remove the Foreground in 21 cm Tomography". *ApJ* 763 (2): 90. doi:10.1088/0004-637X/763/2/90.

Wang, T., et al. 2016. "Discovery of a Galaxy Cluster with a Violently Starbursting Core at z = 2.506". *ApJ* 828 (1): 56. doi:10.3847/0004-637X/828/1/56.

Wang, X., et al. 2006. "21 cm Tomography with Foregrounds". *ApJ* 650 (2): 529–537. doi:10.1086/506597.

Willott, C. J., et al. 2010. “The Canada-France High-z Quasar Survey: Nine New Quasars and the Luminosity Function at Redshift 6”. *AJ* 139 (3): 906–918. doi:10.1088/0004-6256/139/3/906.

Wilman, R. J., et al. 2008. “A semi-empirical simulation of the extragalactic radio continuum sky for next generation radio telescopes”. *MNRAS* 388 (3): 1335–1348. doi:10.1111/j.1365-2966.2008.13486.x.

Wilman, R. J., et al. 2010. “An infrared-radio simulation of the extragalactic sky: from the Square Kilometre Array to Herschel”. *MNRAS* 405 (1): 447–461. doi:10.1111/j.1365-2966.2010.16453.x.

Wouthuysen, S. A. 1952. “On the excitation mechanism of the 21-cm (radio-frequency) interstellar hydrogen emission line.” *AJ* 57:31–32. doi:10.1086/106661.

Wrobel, J. M., and R. C. Walker. 1999. “Sensitivity”. In *Synthesis Imaging in Radio Astronomy II*, ed. by G. B. Taylor, C. L. Carilli, and R. A. Perley, 180:171. Astronomical Society of the Pacific Conference Series.

Wyithe, J. S. B., and A. Loeb. 2004. “A characteristic size of ~10Mpc for the ionized bubbles at the end of cosmic reionization”. *Nature* 432 (7014): 194–196. doi:10.1038/nature03033.

Yatawatta, S., et al. 2013. “Initial deep LOFAR observations of epoch of reionization windows. I. The north celestial pole”. *A&A* 550:A136. doi:10.1051/0004-6361/201220874.

Zahn, O., et al. 2007. “Simulations and Analytic Calculations of Bubble Growth during Hydrogen Reionization”. *ApJ* 654 (1): 12–26. doi:10.1086/509597.

Zaldarriaga, M., S. R. Furlanetto, and L. Hernquist. 2004. “21 Centimeter Fluctuations from Cosmic Gas at High Redshifts”. *ApJ* 608 (2): 622–635. doi:10.1086/386327.

Zaroubi, S. 2013. “The Epoch of Reionization”. In *The First Galaxies*, ed. by B. Wiklind T.and Mobasher and V. Bromm, 396:45. doi:10.1007/978-3-642-32362-1_2.

Zeldovich, Y. B. 1972. “A hypothesis, unifying the structure and the entropy of the Universe”. *MNRAS* 160:1P. doi:10.1093/mnras/160.1.1P.

Zeldovich, Y. B., V. G. Kurt, and R. A. Syunyaev. 1968. “Recombination of Hydrogen in the Hot Model of the Universe”. *Zhurnal Eksperimentalnoi i Teoreticheskoi Fiziki* 55:278–286.

Zernike, F. 1938. “The concept of degree of coherence and its application to optical problems”. *Physica* 5 (8): 785–795. doi:10.1016/S0031-8914(38)80203-2.

Zhang, Y. G., A. Liu, and A. R. Parsons. 2018. “Unlocking Sensitivity for Visibility-based Estimators of the 21 cm Reionization Power Spectrum”. *ApJ* 852 (2): 110. doi:10.3847/1538-4357/aaa029.

Zwicky, F. 1933. “Die Rotverschiebung von extragalaktischen Nebeln”. *Helvetica Physica Acta* 6:110–127.